The Nature, Environments, and Origin of Post-Starburst Galaxies at $z \leq 0.6$

by

Kamalpreet Kaur

A Thesis Submitted to Saint Mary's University, Halifax, Nova Scotia in Partial Fulfillment
of the Requirements for the Degree of Master of Science in Astronomy
(Department of Astronomy and Physics)

August 2021, Halifax, Nova Scotia

Approved: _____
Dr. Ivana Damjanov
Supervisor

Approved: _____
Dr. Marcin Sawicki
Examiner

Approved: _____
Dr. Luigi Gallo
Examiner

Date: August 12, 2021.

Acknowledgements

I am very grateful to my supervisor Dr. Ivana Damjanov for her guidance in my research. Her constant guidance helped me to improve everyday and become a better researcher. I extend my thanks to Dr. Jubee Sohn for providing information about SHELS dataset and addressing all my doubts regarding this dataset. I appreciate the constant feedback on my research from extra-galactic group at the department in ArXiv meetings. I also want to thank committee members for reading my thesis and guiding me through this process. I would like to express deep gratitude to all fellow graduate students in Astronomy and Physics department at Saint Mary's University especially Angelo George and Margaret Buhariwalla for their encouragement. A special thanks to a fellow graduate student and a close friend Paresh Mungara who helped me get through some hard times during my Masters program. Lastly but most importantly, I want to thank my family especially my mom for their love, constant support and encouragement even from 1000 miles away throughout my Masters program. Without their support, this thesis would not have been possible.

Contents

List of Figures

List of Tables

Abstract

The Nature, Environments, and Origin of Post-Starburst Galaxies at $z \leq 0.6$

by Kamalpreet Kaur

Post-starburst galaxies represent a transitional stage between star-forming and quiescent galaxies and thus studying their nature, environments and origin mechanisms is fundamental to understanding galaxy evolution. In this thesis, we select a sample of 48 post-starburst galaxies from SHELS F2 spectroscopic sample using the width of Hδ absorption line combined with visual inspection. We construct galaxy stellar mass density field for the mass-limited SHELS F2 sample within $0.2 < z < 0.55$ to investigate the environments of post-starburst galaxies with respect to general galaxy population. We find that similar fractions of post-starburst galaxies reside in underdense, average dense and overdense regions, i.e., that these galaxies do not prefer special environments. Based on HSC $i-$ band images, we find that ram-pressure stripping, if present, is not strong enough to disturb the morphology of stellar light in cluster post-starburst galaxies and that merger/galaxy interactions drive the formation of post-starburst galaxies in average dense and underdense regions.

August 12, 2021

Chapter 1

Introduction

There are two major categories of galaxies in the universe: star forming spirals and quiescent elliptical galaxies. A star-forming galaxy can transform into a quiescent one following different evolutionary paths such as mass quenching and environmental quenching (Boselli & Gavazzi 2006; Peng et al. 2010; Smethurst et al. 2017). Mass quenching is a slow quenching mechanism and refers to internal processes within the galaxy such as Active Galactic Nuclei (AGN) feedback (Bower et al. 2006; Croton et al. 2006) and the potential well of large stellar bulge (Martig et al. 2009; Genzel et al. 2014). Environmental quenching is a rapid quenching mechanism related to galaxy surroundings. This class of quenching mechanisms involve galaxy-galaxy interactions such as gas-rich mergers (Canalizo et al. 2000; Yang et al. 2004; Cales et al. 2011; Zolotov et al. 2015) and ram-pressure stripping (Gunn & Gott 1972; Larson et al. 1980; Moore et al. 1996; Sohn et al. 2019).

Due to the presence of strong Balmer absorption lines and absence of emission lines, post-starburst galaxies represent a transition stage between star-forming and quiescent galaxies via rapid quenching mechanism (Caldwell et al. 1996; Zabludoff et al. 1996; Norton et al. 2001; Pracy et al.

2009; Wild et al. 2009; Zwaan et al. 2013; Wu et al. 2014; Yesuf et al. 2014; Pattarakijwanich et al. 2016; Wild et al. 2016; Zahid et al. 2016a; Paccagnella et al. 2017; Belli et al. 2019; Wild et al. 2020; Matharu et al. 2020). The studies of the environments and origin of post-starburst galaxies are fundamental to understanding this transition from star-forming to quiescent galaxies and hence galaxy evolution (Couch & Sharples 1987; Dressler & Gunn 1992; Tran et al. 2003; Bekki et al. 2001; Blake et al. 2004; Quintero et al. 2004; Hogg et al. 2006; Poggianti et al. 2009; Mahajan 2013; Yesuf et al. 2014; Paccagnella et al. 2017; Lotz et al. 2020).

1.1 Discovery and Spectroscopic nature

Post-starburst galaxies are galaxies which have undergone a starburst event within past 1 Gyr of their lifetime and abruptly stopped forming stars after that event. A starburst event refers to the formation of large number of stars within a short period of time. This abrupt cessation of star-formation after a starburst event within past 1 Gyr of their lifetime results in strong Balmer absorption lines and no emission lines in the spectra of post-starburst galaxies.

Post-starburst galaxies were first discovered by Dressler & Gunn (1983). The authors found three blue objects in cluster 3C295 at $z = 0.46$ with strong Balmer absorption lines and moderately blue colours ($B - V \sim 0.7$). The colour of an object depends on its temperature. B-V colour index is measured by using the magnitude obtained by two different filters: B refers to blue and V refers to visible (green-yellow) filter. More negative the value of B-V colour index is, hotter and bluer the object is. These three objects discovered in cluster 3C295 are known as post-starburst galaxies.

The spectrum of a post-starburst galaxy has very strong Balmer absorption lines and no or weak

emission lines. Post-starburst spectrum can be reproduced by the combination of spectra of an A dwarf and K0 giant (Dressler & Gunn 1983) and hence they are also known as K+A or E+A galaxies.

A dwarf is a hydrogen burning star with a lifetime of around 1 Gyr on the main sequence and surface temperature of around 7000 - 10,000 K. Emitted radiation from the star's core is absorbed by neutral H atoms present in the stellar atmosphere, producing strong Balmer absorption lines in its spectrum.

K0 is also a main sequence star with a lifetime of around 11 Gyr and surface temperature of around 3500-5000 K. The spectrum of a K0 star has metal absorption lines. K0 stars that evolve into the giant phase of stellar evolution will contribute the most towards the luminosity profile of an elliptical galaxy. Hence, the spectrum of an elliptical galaxy looks similar to a K0 giant.

Elliptical galaxies do not have any emission lines such as [OII] and Balmer emission lines as they lack O and B type stars. Emission lines are produced because of the ionization of hydrogen gas by UV radiation emitted by O,B type stars, hence absence of O,B type stars from elliptical galaxies results in no emission lines in their spectra. The presence of strong Hδ absorption lines with weak or no [OII]/Balmer emission lines in their spectra provides an effective way to detect post-starburst galaxies (Goto et al. 2003a).

After their discovery, the question was raised about the true origin of post-starburst galaxies: are they truly galaxies in a post-starburst phase or just dusty star-forming galaxies (Smail et al. 1999; Poggianti & Wu 2000)? The emission lines present in the spectrum of a dusty star-forming galaxy fade due to extinction of emitted star light by dust while dust has no effect on absorption lines (Asano et al. 2013). As a result, the spectrum of a dusty star-forming galaxy becomes more prominent in absorption features and looks similar to the spectrum of a post-starburst galaxy.

One way to distinguish a post-starburst galaxy from a dusty star-forming galaxy is to look for radio emission. The radio emission is produced by scattering of free electrons from ions present in star-forming regions (Field & Henry 1964). Radio emission is not affected by dust because the corresponding wavelengths are larger than the size of dust particles. Thus, if a galaxy with strong Balmer absorption lines shows radio emission, it is a star-forming galaxy. If, on the other hand, the galaxy shows no radio emission, it is a post-starburst galaxy.

In a sample of 10 radio galaxies, Smail et al. (1999) found five galaxies with strong Balmer absorption lines indicating that they are dusty star-forming galaxies. However, a series of other observations found no radio emission from post-starburst galaxies (Zabludoff et al. 1996; Chang et al. 2001; Miller & Owen 2001). The results of these observations indicate that majority of the galaxies with strong Balmer absorption lines are not dusty star-forming galaxies but genuine post-starburst galaxies that have been abruptly quenched within $\sim$ 1 Gyr of their star formation history. In this study we use either post-starburst or E+A to indicate these systems.

1.2 Internal properties and number density of E+A galaxies

E+A galaxies represent a transitional phase between star-forming and quiescent galaxies as we describe above. Thus studies of the internal properties and number densities of E+A galaxies gives insight into the transition from star-forming to quiescent galaxies (Rowlands et al. 2018; Wild et al. 2016; Zahid et al. 2016b, 2019; Belli et al. 2019).

1.2.1 Internal properties

The internal properties of galaxies that are estimated based on their photometry and spectra are stellar mass, dynamical state, light weighted average age of their stellar population and the structure of their light profiles. By comparing internal properties of E+A with the properties of star-forming and quiescent galaxies we can probe their connection to these galaxy populations.

D_n4000 index is the measure of strength of 4000 Å break and is calculated as the ratio of flux in 4000–4100 Å and 3850–3950 Å bands (Balogh et al. 1999). The 4000 Å break is the discontinuity in the spectra of galaxies that is caused by blanket absorption of radiation by neutral metal atoms present in the atmospheres of cool stars. Galaxies which have younger stellar population (i.e., hot O, B type stars) have low value of D_n4000 index and galaxies which have older stellar population (i.e., cool A, F type stars) have higher value of D_n4000 index (Section 2.2.2). Studies at $z \sim 0.1$ (Yamauchi & Goto 2005) and $0.5 < z < 1.2$ (Vergani et al. 2010) indicate that D_n4000 values of E+A galaxies lie within $1.2 < D_n4000 < 1.6$, intermediate to star-forming ($D_n4000 < 1.5$) and quiescent ($D_n4000 > 1.5$) galaxies.

Sérsic profile of a galaxy gives information about how the light is distributed within the galaxy (Sersic 1968). Spiral galaxies follow an exponential Sérsic profile in which the intensity of light declines towards the outer regions of the galaxy and quiescent galaxies follow de Vaucouleurs profile in which light is more concentrated in the center but also extends towards the outer regions of the galaxy (Section 2.1.1.1). Studies at $z \gtrsim 1$ (Almaini et al. 2017; Matharu et al. 2020) indicate that Sérsic index values of E+A galaxies lie intermediate to star-forming ($n = 1$) and quiescent galaxies ($n = 4$) but are on average more consistent with quiescent galaxies.

The relation between galaxy size (measured from its Sérsic profile) and its stellar mass differs for star-forming and quiescent galaxies and this relation evolves with redshift (Shen et al. 2003; Williams et al. 2010; van der Wel et al. 2014). Theoretical studies connect these observational results to the physical processes that drive mass assembly such as bulge growth, major and minor mergers and galaxy-cluster environment interactions (Toomre 1964; Couch & Sharples 1987; Naab et al. 2009; Oser et al. 2010; Rodriguez-Gomez et al. 2015). Size-mass relation is shallow for star-forming galaxies, much steeper for quiescent galaxies, and E+A galaxies follow a size-mass relation which is intermediate to both galaxy populations (Almaini et al. 2017; Matharu et al. 2020).

Furthermore, quiescent galaxies include a sub population of very compact galaxies i.e., galaxies that are extremely small in size for their stellar mass (Carollo et al. 2013; Damjanov et al. 2014, 2015; Zahid et al. 2016b). These galaxies were thought to disappear with decreasing redshift, but recent studies show that they are still present at $z < 1$ (Carollo et al. 2013; Damjanov et al. 2014, 2015). A sample of compact E+A galaxies at $0.2 < z < 0.8$ discovered in the Sloan Digital Sky Survey (Zahid et al. 2016b) are contributing to the population of young quiescent galaxies at these redshifts. On the other hand, non-compact E+A galaxies contribute to the number density of non-compact quiescent galaxies at low stellar mass, a process known as progenitor bias (van der Wel et al. 2009; Carollo et al. 2013; Zahid et al. 2019).

1.2.2 Number density

One way to study galaxy evolution is to compare the number densities of star-forming, post-starburst and quiescent galaxies at different redshifts. Various studies have found that with decreasing redshift, the number density of quiescent galaxies increases and post-starburst galaxies decreases (Bell et al.

2004; Arnouts et al. 2007; Brown et al. 2007; Wild et al. 2009, 2016; Rowlands et al. 2018; Belli et al. 2019; Wild et al. 2020). This trend in number densities indicates that post-starburst galaxies contribute towards the number density growth of quiescent population.

The growth of number density of quiescent population due to post-starburst galaxies between two redshifts is calculated as the ratio of change in number density of quiescent galaxies between two redshifts to visibility time[1] (Belli et al. 2019). Minimum visibility time is calculated assuming that 100% of post-starburst galaxies contribute to the number density growth of quiescent galaxies. Various studies report different values of visibility time ranging from 250 Myr to 1 Gyr but the most commonly used value is 250 Myr (Wild et al. 2009, 2016; Rowlands et al. 2018; Belli et al. 2019). Using this visibility time scale (250 Myr), Wild et al. (2016) finds that E+A galaxies contribute 100% to the growth of quiescent galaxies at $0.5 < z < 1.5$. Belli et al. (2019) finds that E+A galaxies contribute 50% to the number density growth of quiescent galaxies at $z \sim 2$ using visibility time of 500 Myr.

1.3 Environments of E+A galaxies

There is no universal definition of "galaxy environment". A number of studies over the years have used different techniques to probe environments around galaxies ranging from local to global scale (Cooper et al. 2005; Gallazzi et al. 2009; Wolf et al. 2009; Kovač et al. 2010; Wilman et al. 2010). Local environments around galaxies probe scales internal to halo and global environments probe scales external to the halo (Muldrew et al. 2012). While studying the global environment around galaxies can give insight into the formation of large scale structure of the universe, probing local

[1]Visibility time is the time spent by a galaxy in post-starburst phase.

environments can give more detailed information about the formation of individual galaxies.

1.3.1 Measuring Environments

A direct measure of galaxy environment is the number of neighbouring galaxies that surround it. There are two main techniques used to probe environments around galaxies based on whether number of nearest neighbours are fixed or the probed volume/area is fixed. These techniques are described below.

1.3.1.1 Nearest neighbour method

Nearest neighbour method is based on the principle that galaxies which have closest nearest neighbours reside in highest density environments. The number of nearest neighbours are fixed and projected surface density around a galaxy is defined as (Muldrew et al. 2012)

$$\sigma_n = \frac{n}{\pi r_n^2}, \tag{1.3.1}$$

where σ_n is projected surface density, n is number of nearest neighbours and r_n is the distance to n^{th} nearest neighbour. Projected surface density is not an accurate measurement of environment as it also includes foreground and background galaxies misidentified as neighbours. To eliminate misidentified neighbours, third dimension (redshift) is included with a velocity cut of $\pm$1000km s^{-1} and volume density is defined as (Muldrew et al. 2012)

$$\Sigma_n = \frac{n}{(4\pi/3) r_n^3}, \tag{1.3.2}$$

where Σ_n is volume number density and $(4\pi/3)\ r_n^3$ is the volume enclosed by nearest neighbours. Nearest neighbour method can be used to probe local environment around a galaxy using small n values ranging from $n = 3$ to $n = 7$ while large n values (> 10) can be used to probe large scale structures (Muldrew et al. 2012). In other words, smaller the value of n, more accurate the measurement of local environment and larger the value of n ($10 < n \lesssim 65$), more accurate is the measurement of global environment. Nearest neighbours with $n > 65$ may be too far away from central galaxy to have contribution in density estimation around central galaxy.

1.3.1.2 Aperture method

Aperture method is based on the principle that galaxies having more neighbours within a given volume reside in denser environments. The scale used to probe environment around galaxies is fixed and all galaxies within the volume that corresponds to that scale are used for density estimation (Croton et al. 2005). Density contrast is used to express environments around galaxies in aperture method and is defined as (Muldrew et al. 2012)

$$\delta = \frac{N_g - \bar{N_g}}{\bar{N_g}}, \tag{1.3.3}$$

where N_g is the number of galaxies within given volume and $\bar{N_g}$ is mean number of galaxies within the same volume if galaxies are distributed randomly. It is important to impose a velocity cut of $\pm$1000km s^{-1} in aperture method as well for the same reason as explained in Section 1.3.1.1.

Aperture method can be used to probe local environment around galaxies with small scales such as 1 and 2 Mpc while larger scales can be used to probe large scale structure (Muldrew et al. 2012).

As in the nearest neighbour method applications, smaller the scale, better is the measurement of local environment and large the scale, better is the measurement of global environment.

1.3.2 Evolution in Environments of E+A galaxies

E+A galaxies are found in both clusters and field at all redshifts but their abundance changes with environment and redshift (Poggianti & Barbaro 1997; Yang et al. 2008; Poggianti et al. 2009; Paccagnella et al. 2017) . Most of the studies related to the environments of E+A galaxies at $0.3 < z < 0.8$ indicate that E+A galaxies are found in clusters at this redshift range (Dressler et al. 1999; Poggianti et al. 1999; Tran et al. 2003, 2004; Tran 2007; Poggianti et al. 2009; Dressler et al. 2013). However, Balogh et al. (1999) found similar fraction of E+A galaxies in both clusters and field at $z \sim 0.2-0.3$ and Poggianti et al. (2009) found significant fraction of E+A galaxies in groups with low [OII] emission in addition to clusters at $z \sim 0.4-0.8$.

At low redshift $z \sim 0.1$, E+A galaxies are found in low density environments like field and poor galaxy groups (Zabludoff et al. 1996; Quintero et al. 2004; Balogh et al. 2005; Goto 2005a; Hogg et al. 2006; Nolan et al. 2007). However, there are few studies at $z \sim 0.1$ which find E+A galaxies in clusters (Mahajan 2013; Poggianti et al. 2016; Paccagnella et al. 2017).

Most of the studies at $z \geq 0.2$ and $z \sim 0.1$ have approximately similar range of absolute magnitude in $r-$band[2] for E+A galaxies i.e. $-18 < M_r < -23$. As the absolute magnitude at this rest-frame wavelength is related to stellar mass (i.e., brighter galaxies are more massive), we conclude that samples of E+A galaxies in these studies roughly cover similar range of stellar mass values. Thus mass quenching should have similar effect on E+A galaxy samples from different studies.

[2] $r-$band refers to wavelength range of $\sim$ 5500 Å to 7500 Å.

1.4 Origin of E+A galaxies in different environments

The fraction of E+A galaxies change with the density of the environment at all redshifts (Section 1.3.2). The change in the fraction of E+A galaxies gives information about different physical mechanisms that prevail at different redshifts because these mechanisms change with environment (Paccagnella et al. 2017).

1.4.1 Low density environment

In low density environments like poor galaxy groups and field, the origin of E+A galaxies is attributed to gas-rich merger/galaxy interaction (Bekki et al. 2001; Blake et al. 2004; Quintero et al. 2004; Goto 2005b; Hogg et al. 2006; Mahajan 2013; Yesuf et al. 2014; Lotz et al. 2020). A merger event requires both galaxies to have low relative velocities so that they do not just pass each other without enough time to experience a merger. Galaxies have low relative velocities in the field and poor galaxy groups, making these environments suitable for merger events. A gas rich merger between two galaxies leads to influx of large amount of gas in the center. This gas is contributed by both galaxies and triggers a starburst event if it is cool and dense enough to form stars. After initial burst of star-formation, gas either gets completely exhausted or remaining gas heats up resulting in abrupt quenching of star-formation (Johansson et al. 2009).

A merger event also fuels AGN and thus can also cause quenching through AGN feedback. The heating up of gas or removal of gas from the galaxy by AGN results in quenching of star-formation, a process known as AGN feedback (Di Matteo et al. 2005; Hopkins et al. 2006). The accretion of gas by AGN results in the emission of X-rays, a way to detect AGN host galaxies. Early works related to

post-starburst galaxies did not include AGN hosts because of selection criteria allowing no emission (Yan et al. 2006). Studies related to AGNs found some galaxies with strong Hδ absorption lines (Kauffmann et al. 2003a; Cid Fernandes et al. 2004). Using less restrictive selection criteria, later studies of post-starburst galaxies found AGN emission lines in the spectra of post-starburst galaxies[3] (Yan et al. 2006; Sell et al. 2014; Wild et al. 2007; Yesuf et al. 2014). Based on the study of time delay between occurrence of starburst event and AGN feedback, various studies of post-starburst galaxies have found that starburst feedback is the primary quenching mechanism in post-starburst galaxies while AGN feedback plays secondary role (Croton et al. 2006; Schawinski et al. 2007; Wild et al. 2009; Snyder et al. 2011; Cen 2012; Hayward et al. 2014; Yesuf et al. 2014).

Studies of the morphologies of post-starburst galaxies in low density environments indicate that these galaxies have disturbed morphologies and tidal features providing an evidence for merger origin (Zabludoff et al. 1996; Blake et al. 2004; Goto 2005b; Yamauchi & Goto 2005; Goto et al. 2008; Pracy et al. 2009). In addition to disturbed morphologies, a merger event also results in bluer colors and clump patterns in color maps of post-starburst galaxies indicating a centrally localized starburst event (Goto 2005a; Yang et al. 2008; Pracy et al. 2009).

Environmental processes such as major mergers may not be the primary mechanism for the quenching of star formation in massive galaxies ($log(M_\star/M_\odot) \simeq 10.65$), where mass quenching plays significant role. The presence of heavily obscured X-ray AGNs in galaxies with $log(M_\star/M_\odot) \simeq 10.65$ at $z < 1$ indicates that these galaxies experience major merger after they are quenched (Moutard et al. 2020). The evidence for major mergers after quenching comes from the flipping of angular momentum of the host dark matter haloes of these galaxies as a result of mergers (Pichon et al. 2011;

[3]Note that these post-starburst galaxies do not comply with the definition of E+A galaxies used in our study

Codis et al. 2015; Moutard et al. 2020). These galaxies undergo quenching due to slow (1 - 3.5 Gyr) quenching mechanisms leading to the formation of green valley galaxies which may or may not include post-starburst galaxies.

1.4.2 High density environment

In high density environment like clusters, galaxies have very high relative velocities and they pass each other without enough time to experience merger and hence mergers are not frequent (Ostriker 1980). The most dominant mechanism for origin of post-starburst galaxies in clusters is ram-pressure stripping. A star-forming galaxy falls into cluster environment and its molecular hydrogen gas (out of which starts are formed) is removed by interaction with dense intracluster medium (Couch & Sharples 1987; Dressler & Gunn 1992; Tran et al. 2003; Tran 2007; Poggianti et al. 2009; Paccagnella et al. 2017). Ram pressure increases with the density of the ICM and the relative velocity of galaxy with respect to the ICM (Gunn & Gott 1972; Larson et al. 1980; Moore et al. 1996; Sohn et al. 2019). When ram pressure acting on the galaxy exceeds the restoring force produced per unit area of the disc of galaxy, gas is removed from the galaxy. This removal of gas from the galaxy results in quenching of star formation and transition into post-starburst phase over a period of time ($\sim$ 1Gyr). There are observations of jellyfish shaped galaxies with disturbed morphologies and 5-10 % of these jellyfish shaped galaxies are either post-starburst or spectroscopically passive galaxies (Poggianti et al. 2016). These observations provide indirect evidence for the formation of E+A galaxies by ram-pressure stripping. The positive correlation between the fraction of post-starburst galaxies and halo mass/cluster velocity dispersion also provides the evidence for ram-pressure stripping being the dominant mechanism for origin of post-starburst galaxies in clusters (Paccagnella et al. 2019).

Ram-pressure stripping is stronger in massive clusters (Gunn & Gott 1972; Jaffé et al. 2015), this may be either due to the larger fraction of E+A galaxies in more massive dark matter haloes or longer E+A phase in these haloes.

1.5 Motivation and structure of this thesis

The formation mechanism and properties of galaxies are closely related to their environment (Zehavi et al. 2005; Li et al. 2006; Blanton et al. 2005; Cassata et al. 2007). As E+A galaxies represent a transitional phase between star-forming and quiescent galaxies (Caldwell et al. 1996; Zabludoff et al. 1996; Norton et al. 2001; Pracy et al. 2009; Wild et al. 2009; Zwaan et al. 2013; Wu et al. 2014; Yesuf et al. 2014; Pattarakijwanich et al. 2016; Wild et al. 2016; Zahid et al. 2016a; Paccagnella et al. 2017; Belli et al. 2019; Wild et al. 2020; Matharu et al. 2020), studying their environments can help understand galaxy evolution. We aim to study the environments of E+A galaxies within $0.2 < z < 0.55$ using spectroscopic data from Smithsonian Hectospec Lensing Survey (SHELS) F2 4 deg^2 field (Geller et al. 2014, 2016). We want to make a connection between low redshift ($z \sim 0.1$) studies (Bekki et al. 2001; Blake et al. 2004; Quintero et al. 2004; Goto 2005b; Hogg et al. 2006) and studies at $0.2 < z < 0.8$ (Dressler et al. 1999; Balogh et al. 1999; Poggianti et al. 1999; Tran et al. 2004; Dressler et al. 2013) and probe the redshift range ($0.2 < z < 0.5$) in which the main mechanisms for the formation of E+A galaxies are debatable. We thus investigate different quenching mechanisms responsible for the transformation of star-forming galaxies to quiescent galaxies via post-starburst phase in different environments (Yang et al. 2008; Mahajan 2013; Yesuf et al. 2014; Paccagnella et al. 2017; Lotz et al. 2020).

The structure of the thesis is as follows. We provide the description of SHELS dataset in Chapter 2 and discuss the criteria used to select our sample of E+A galaxies in Chapter 3. Chapter 4 includes the discussion of internal properties and number density of E+A galaxies. We measure the environments of E+A galaxies in Chapter 5 . Chapter 6 includes the discussion of our results and the comparison with literature. We discuss conclusions and future goals of our study in Chapter 7. Throughout this thesis, we assume a ΛCDM cosmology with present-day $\Omega_M = 0.3$, $\Omega_\Lambda = 0.7$ and $H_0 = 68\text{km s}^{-1}\text{ Mpc}^{-1}$.

Chapter 2

Dataset

We use spectroscopic data from the Smithsonian Hectospec Lensing Survey (SHELS) for our study. SHELS (Geller et al. 2014, 2016) is a dense redshift survey which covers two fields (F1 and F2) of Deep Lensing Survey (Wittman et al. 2006). SHELS has a redshift range of $0.1 < z < 0.6$ with median redshift of $z = 0.3$. F2 field is 4 deg^2, centered at $R.A._{.2000} = 09^h19^m32.4^s$ and $Decl._{.2000} = 30^0 00' 00''$. We use 17, 343 galaxy spectra from SHELS F2 field for our analysis.

2.1 Photometry

DLS images in R-band are used to select spectroscopic targets (Geller et al. 2014). The objects in F2 catalog have a limiting surface brightness of 27 mag arcsec^{-2} within the half light radius[1]. Bright stars have wide extended wings which can affect the photometry of nearby objects. To reduce the effect from bright objects, SHELS catalog excludes the regions surrounding brighter objects. The radius of excluded region around each bright star can be calculated using USNO-A2 m_v magnitudes

[1]Half light radius is the radius containing 50% flux of the galaxy.

(Monet et al. 2003) using the relation

$$r_{excluded} = 1.2(m_v - 15.5)^2 \text{arcsec}. \quad (2.1.1)$$

Excluded regions include 0.21 deg^2 of area in F2 field (4.19 deg^2) leaving an unmasked area of 3.98 deg^2. SHELS catalog also excludes the artifacts inspected visually on the extreme faint end of the survey.

SHELS galaxies have Sloan Digital Sky Survey (SDSS) DR16 photometric data (Ahumada et al. 2020) in five bands (u, g, r, i, z) which is used for the determination of stellar masses for these galaxies (Section 2.2.3). We use $r-$band SDSS petrosian magnitudes[2] to estimate 85% spectroscopic completeness absolute magnitude limit for SHELS F2 galaxies which we later transform into stellar mass limit (Section 4.1).

2.1.1 Structural parameters

Galaxy structural parameters used in this analysis (Damjanov et al. 2019) are based on the Sérsic profile fit to the galaxy (Sersic 1968). We briefly explain these parameters and how they were derived in subsections below.

2.1.1.1 Sérsic profile

Sérsic profile (Sersic 1968) is a mathematical expression which describes the radial dependence of the surface brightness of the galaxy as

[2]Petrosian magnitude is the magnitude corresponding to the flux within petrosian radius. Petrosian radius (R) is the radius at which the average intensity at a distance R from center of the galaxy is equal to the intensity within R (Petrosian 1976).

$$I(r) = I_0 \exp\left\{-b_n \left(\frac{r}{r_e}\right)^{1/n}\right\}. \tag{2.1.2}$$

Here I_0, r_e, b_n and n are all free parameters of Sérsic model profile. I_0 is the central surface brightness, n is Sérsic index, r_e is the half light radius along semi major axis and b_n is a function of n such that r_e contains half of the total galaxy light. The best fit of Sérsic model profile with the brightness profile of the galaxy gives values for all these free parameters. Sérsic index is a measure of how concentrated the light is towards the center of the galaxy.

Galaxy discs follow exponential profile (i.e. $n = 1$) in which the intensity of light declines towards the outer regions of the galaxy as

$$I(r) = I_0 \exp\{-r/r_e\}. \tag{2.1.3}$$

Elliptical galaxies follow de Vaucouleurs profile (i.e. $n = 4$) in which light is more concentrated in the center but also extends towards the outer regions of the galaxy as

$$I(r) = I_0 \exp\left\{-b_n \left(\frac{r}{r_e}\right)^{1/4}\right\} \tag{2.1.4}$$

(de Vaucouleurs 1948). Here $b_n = 1.999n - 0.327$ for $n > 1$. Hence, $b_n = 5.67$ for $n = 4$.

2.1.1.2 Axis ratio and size

Axis ratio is the ratio of intrinsic semi-minor axis to intrinsic semi-major axis of the galaxy i.e B/A. Galaxies are 3-D objects but appear as 2-D objects on the sky. We can not directly measure intrinsic

axis ratio (B/A) of a galaxy but we can measure its projected axis ratio (b/a) on the sky. Distribution of b/a can be connected to the distribution of intrinsic shapes of galaxies.

Size of a galaxy is defined in terms of half light radius (R_e). Half light radius is the distance from the center of the galaxy which contains 50% of the flux of the galaxy. The definition of half light radius assumes a circularly symmetric morphology for galaxies i.e. $b/a = 1$. We change the effective radii into circularized radii as $R_c = R_e\sqrt{b/a}$ to be able to compare our size measurements with literature (Section 4.4).

2.1.2 Galaxy Sérsic profile properties

The sizes for SHELS F2 galaxies are estimated by Damjanov et al. (2019) using Hyper Suprime-Cam (HSC) photometric data (Aihara et al. 2018). The authors fit the Sérsic profile (Section 2.1.1.1) with the surface brightness profile of each galaxy using SExtractor software[3] (Bertin & Arnouts 1996). This software returns best fit parameters such as n, b/a and R_e (in arcseconds). They convert angular size (R_e) of each galaxy to kiloparsecs using angular diameter distance at redshift of each galaxy. The errors in size measurements are calculated by comparing 4999 repeat measurements from 4999 objects which were observed twice because of overlap of HSC pointings. For detailed procedure, the reader should refer to Damjanov et al. (2019).

2.2 Spectroscopy

We use 17,343 SHELS spectra for our analysis. SHELS spectra are acquired using Hectospec (Fabricant et al. 2005) on Multiple Mirror Telescope (MMT). Hectospec is an optical spectrograph

[3] https://sextractor.readthedocs.io/en/latest/Model.html

fed by 300 optical fibers which operates over the wavelength range of 350-1000 nm with a full width half maximum (FWHM) resolution of 5Å.

? reduce the data[4] with the standard Hectospec pipeline[5]. Hectospec pipeline makes use of Image Reduction and Analysis Facility (IRAF) script which extracts 1d spectra. The pipeline corrects the spectra beyond 7000Å for OH emission by masking this skyline. Bright mercury and oxygen skylines are also masked. The spectra are available in terms of fits files. Each fits file has four arrays corresponding to flux calibrated spectrum, sky-subtracted spectrum, flux errors and mask.

Additionally, we have spectroscopic data for 2643 SDSS/Baryon Oscillation Spectroscopic Survey (BOSS) galaxies (Ahumada et al. 2020) which we use to extend our sample of E+A galaxies selected from SHELS spectra. SDSS covers the wavelength range of 3800 - 9200 Å with resolution of 1500 at 3800 Å and 2500 at 9000 Å.

2.2.1 Determination of redshift

SHELS F2 catalog has redshift values for all galaxies determined using RVSAO (Kurtz & Mink 1998). RVSAO is an IRAF radial velocity package developed at Smithsonian Astrophysical Observatory (SAO) to measure redshift values from emission and absorption lines present in the spectrum of each galaxy. We provide a brief description in the next paragraph about how RVSAO work.

The program loads the spectrum file, renormalizes the spectrum and subtracts the continuum from the spectrum. After continuum subtraction, the program fits the spectral lines in the galaxy spectrum with a model spectrum. It is important to select suitable template model spectra depending on whether the program fits emission lines or absorption lines. The program suppresses emission

[4]Hectospec makes use of two CCD detectors for imaging and stores data as multiextension files
[5]http://www.mmto.org/hsred-reduction-pipeline/

(absorption) lines present in the spectrum of the galaxy while fitting with absorption (emission) model template spectra for best fitting. After fitting with a model spectrum, the program defines a table containing the wavelength ranges for different spectral lines present in the galaxy.

The comparison of observed wavelength range and rest wavelength range (obtained from model spectrum) of the brightest spectral line gives an initial guess on the redshift value. The same process is repeated for next brightest spectral line to obtain second guess on the redshift value. This process continues for all spectral lines present in the galaxy until the final redshift is determined.

2.2.2 D_n4000 index measurements

SHELS survey provides D_n4000 values for all galaxies in F2 field which are computed by Dr. Jubee Sohn[6]. D_n4000 index is the measure of strength of 4000 Å break. D_n4000 index is the ratio of flux in 4000–4100 Å and 3850–3950 Å bands (Balogh et al. 1999). We use D_n4000 values in our analysis to categorise star-forming ($D_n4000 < 1.5$) and quiescent ($D_n4000 > 1.5$) galaxies.

There is a large abundance of O and B type stars in star-forming galaxies as compared to quiescent galaxies. The atmospheres of O and B type stars are transparent and contribute efficiently towards the continuum flux to the blue end (3850–3950 Å) of 4000 Å break resulting in low strength of D_n4000 index for star-forming galaxies. As the galaxy's star formation rate decreases, O, B type stars die out leaving numerous cool A,F type stars. Neutral metal atoms present in the cool atmospheres of A and F type stars absorb the photons from the blue end of 4000 Å break resulting in a decrease in the continuum flux. Hence quiescent galaxies have higher value of D_n4000 index than star-forming galaxies (Balogh et al. 1999).

[6]Post-doctoral researcher at the Harvard-Smithsonian Center for Astrophysics,US.

The value of D_n4000 index is calculated as the ratio of flux (in erg s^{-1} cm^{-2} Hz^{-1}) in the 4000–4100 Å and 3850–3950 Å bands. The errors on these measurements are based on 1468 pairs of SHELS spectra by (Fabricant et al. 2008). These errors include in quadrature the sum of statistical and systematic errors. Statistical errors in flux measurements are the resultant of error propagation of flux errors for each pixel of the spectra. Systematic errors are computed based on differences between 1468 repeated measurements from 1468 pairs of SHELS spectra and can arise from different factors like short-term variations in the wavelength dependence, amount of extinction, variable alignment of the fiber with respect to the observed galaxy, errors in calibration of fiber to fiber and imperfect sky subtraction. Total internal error in each measurement (σ) of D_n4000 index is computed such that 68% of measured differences lie within $\sqrt{2}\sigma$ and is equal to 0.045 times each measurement.

2.2.3 Stellar mass

We also use stellar mass values from the SHELS catalog provided by Dr. Jubee Sohn[7]. These values are estimated using Le Phare code[8](Arnouts et al. 1999; Ilbert et al. 2006), SDSS five-band photometry ($ugriz$) and known galaxy redshift (Zahid et al. 2013). This code involves fitting stellar population synthesis (SPS) models to spectral energy distributions (SEDs) of galaxies to obtain mass to light ratio. The models used to estimate stellar mass values of SHELS F2 galaxies are based on Bruzual & Charlot (2003) and Chabrier (2003) initial mass function (IMF). The set of models include two stellar metallicity values (0.4 and 1 solar), seven exponentially decreasing star formation rates (SFRs)[9] with decay times (τ) of 0.1, 0.3, 1.2, 3, 5, 10, 15, 30 Gyr and reddening of $0 < E(B-V) < 0.6$

[7]Post-doctoral researcher at the Harvard-Smithsonian Center for Astrophysics,US.

[8]http://www.cfht.hawaii.edu/~arnouts/LEPHARE/lephare.html

[9]SFR of a galaxy at time t is given is given by: $\psi(t) = \tau^{-1} \exp[-(t-t_f)/\tau]\, H(t-t_f)$, where $H(t-t_f)$ is a Heaviside function such that $H(t-t_f) = 1$ for $t > t_f$ and $H(t-t_f) = 0$ for $t < t_f$, t_f is the onset of star formation and τ is decay

using the extinction law of Calzetti et al. (2000). The program fits each model SED to the observed SED of the galaxy to give an estimate of mass-to-light ratio (M/L) of the galaxy in different bands. The product of M/L in a given band with the luminosity in the same band gives the value of stellar mass of the galaxy.

time. Decay time is the time in which SFR of a galaxy becomes $1/e$ times of its peak value.

Chapter 3

Selecting E+A sample based on spectroscopic properties

Post-starburst galaxies are selected on the basis of specific features in their spectra such as very strong Hδ absorption line at 4100 Å and very weak or no [OII] emission line at 3727 Å (Figure 3.1). There are many different definitions of post-starburst galaxies and majority of them are based on the strength of Hδ and [OII] spectral lines.

The strength of a spectral line is defined in terms of equivalent width (EW) which is a quantitative measure of the area under the spectral line. The positive value of EW corresponds to absorption line and negative value corresponds to emission line. The positive value of EW([OII]) represents very weak emission line. The common selection criteria for E+A galaxies is EW(Hδ) > 4 Å and EW([OII]) > 0 Å (Goto et al. 2003a).

Hδ spectral line is usually selected over other hydrogen Balmer lines for selection criteria because

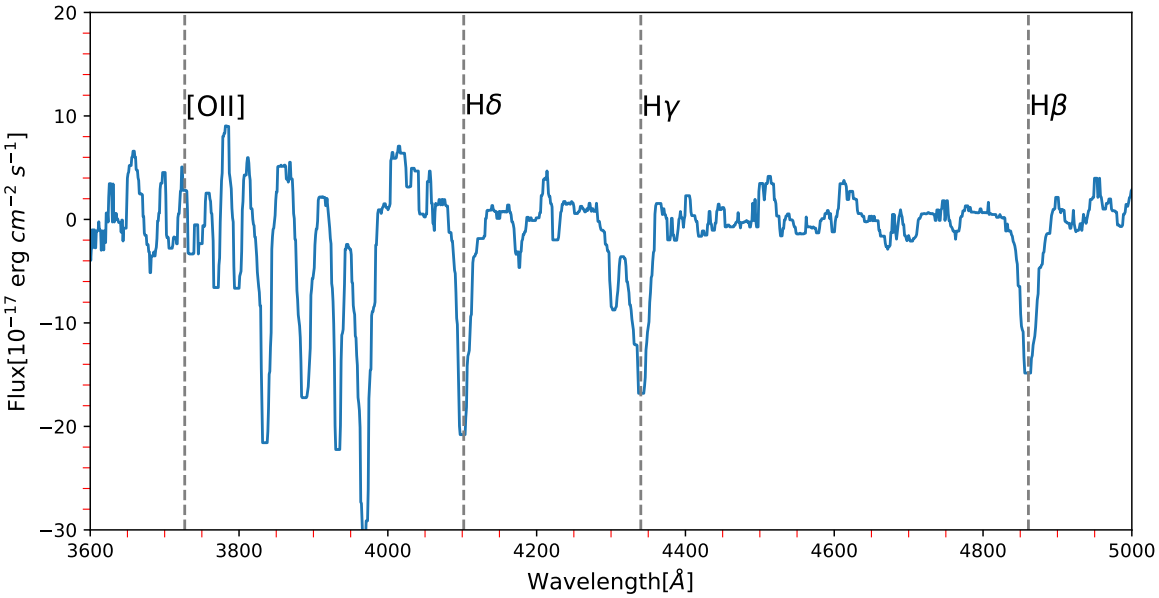

Figure 3.1: Spectrum of a SDSS post-starburst galaxy showing Hδ, Hβ, Hγ and [OII] spectral lines. Hδ spectral line is a prominent feature in the spectrum of a post-starburst galaxy but [OII] spectral line is barely visible because of its very low strength.

Table 3.1: Wavelength ranges corresponding to continuum and line regions in Å

Spectral line	Blue continuum	Line region	Red continuum
[OII]	3653-3713	3713-3741	3741-3801
$H\delta_{wide}$	4030-4082	4082-4122	4122-4170
$H\delta_{nar}$	4030-4082	4088-4116	4122-4170
$H\alpha$	6537-6490	6490-6594	6594-6640

it is least affected by emission filling. Emission filling is the presence of emission at the bottom of the absorption line and decreases the corresponding equivalent width (Section 3.1.2.1). Higher order Balmer lines ($H\beta$, $H\gamma$) are affected more by emission filling and lower order Balmer lines ($H\epsilon$, $H\zeta$) have low signal to noise ratio (Goto et al. 2003a).

3.1 Equivalent width of emission and absorption lines

We develop a code to measure equivalent widths of $H\delta$ and [OII] spectral lines and use a test sample from Goto et al. (2003a) to test the reliability of our code. This test sample consists of 200 post-starburst galaxies selected from SDSS[1] DR7 catalog available at webpage[2]. This catalog consists of 564 post-starburst galaxies selected as: EW($H\delta$) > 5 Å, EW[OII] > -2.5 Å and EW($H\alpha$) > -3 Å (Goto et al. 2003a,b; Goto 2005a, 2007).

3.1.1 Procedure

3.1.1.1 Flux Summing Method

Flux summing method involves summing the flux in a wavelength range centered on the spectral line (Abraham et al. 1996; Balogh et al. 1999; Goto et al. 2003a). We choose to use flux summing method described in Goto et al. (2003a) as it is consistent with previous studies done by Zabludoff et al. (1996) and Balogh et al. (1999). Table 3.1 lists different wavelength regions that we use to calculate the equivalent width of Hδ, [OII] and Hα spectral lines (Abraham et al. 1996).

There are two line regions defined in Table 3.1 for Hδ spectral line: narrow wavelength region (4088 Å - 4116 Å) for Hδ_{nar} (EW(Hδ) < 2Å) and wide wavelength region (4082 Å - 4122 Å) for Hδ_{wide} (EW($H\delta$) > 2 Å). We know from Goto et al. (2003a) that for large equivalent widths, wider wavelength window gives larger values of equivalent widths as compared to narrower window. This is because narrower window is not able to capture the wings of the absorption line. On the other hand, narrower window works better for small equivalent widths because wider window is more affected by noise (see Abraham et al. (1996) for similar discussion). We use wide window to find EW(Hδ) because all 200 galaxies in our test sample have large equivalent widths (i.e. $>$ 2 Å) and lie within 6.8 Å $< EW(H\delta) <$ 9.28 Å .

3.1.1.2 Continuum fitting

It is important to find a suitable continuum flux value at each wavelength which reliably represents the continuum level in the line region. Choosing one continuum flux value over the whole wavelength

[1]Sloan Digital Sky Survey(SDSS) is a redshift survey which uses a 2.5 m, wide-angle optical telescope at Apache Point Observatory, New Mexico, United States to obtain photometric as well as spectroscopic data (Stoughton et al. 2002).

[2]http://www.phys.nthu.edu.tw/~tomo/research/ea_dr7/

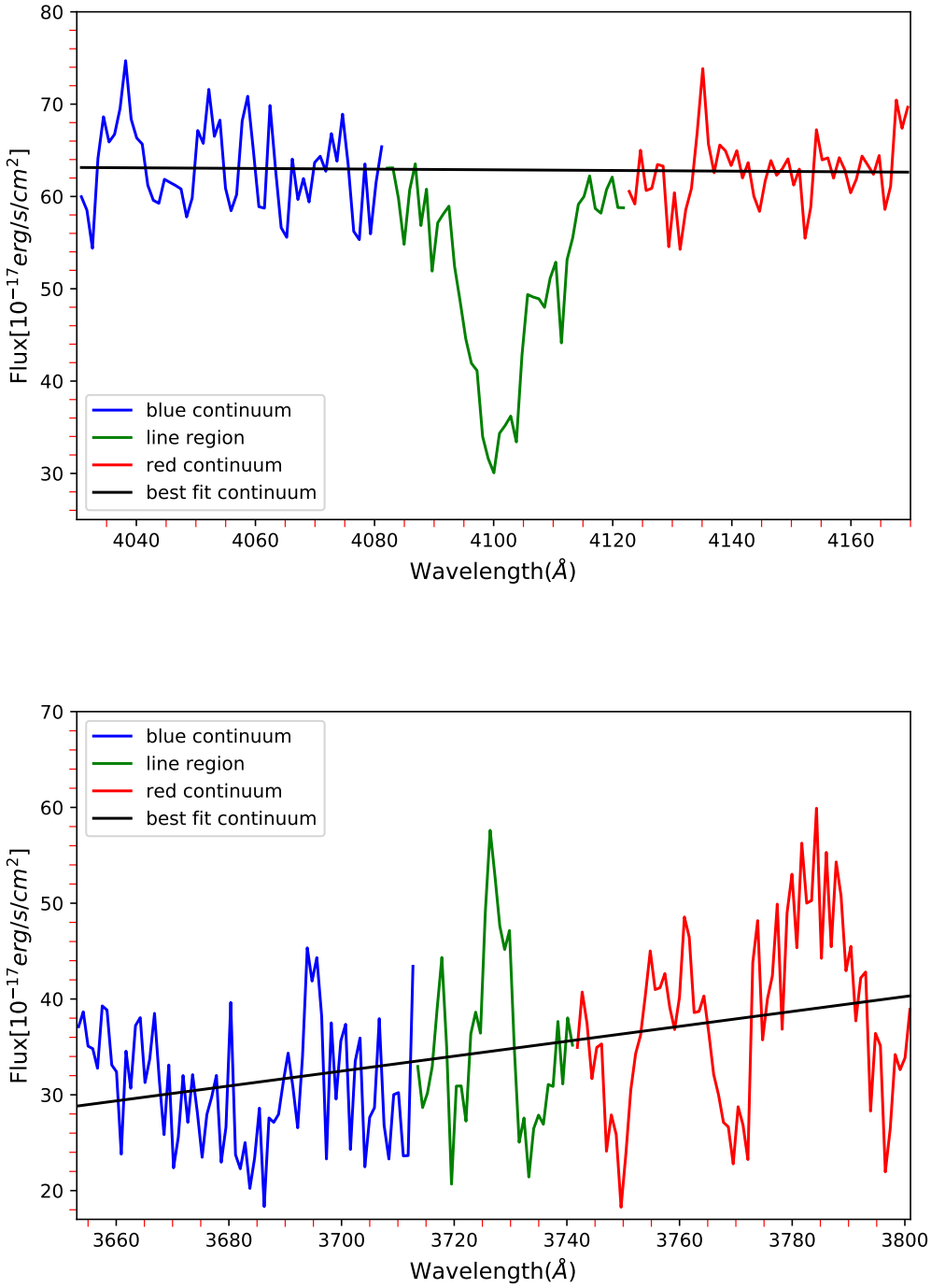

Figure 3.2: Top: Continuum and line wavelength regions for Hδ spectral line. Red colour represents red continuum region, blue colour represents blue continuum region and green colour represents line region. Black line represents the continuum level obtained by linear fitting. Bottom: Continuum and line wavelength regions for [OII] spectral line with overplotted continuum level. Color scheme is the same as top panel.

range can lead to erroneous results because the continuum level changes across the line region.

The continuum level is obtained by linear fitting of flux values in red and blue continuum regions. After initial fit, we calculate differences between given flux values and flux values obtained from best fit at each wavelength in continuum regions. We ignore flux values in continuum regions which lie more than 2σ away from the best fit line for next fitting. We repeat the fitting process several times after eliminating 2σ outliers each time until none is left. After a number of iterations, we find best fit parameters and use the best fit line to find continuum flux values for the line region (Figure 3.2).

3.1.1.3 Algorithm for EW values

The algorithm that we use to estimate the equivalent widths of different emission and absorption lines written in `Python`[3] includes the following steps:

1. Spectra are available in the first row of the fits file while wavelength values are extracted using $C0$ (center wavelength) and $C1$ (dispersion per pixel) coefficients from the header.

2. The wavelength regions given in Table 3.1 are rest frame ($z = 0$) wavelength regions for different spectral lines. These spectral lines shift to higher wavelength range in the spectrum of the galaxy with increasing redshift as a result of the expansion of the universe (Hubble 1929). To calculate rest frame EW values, we shift the spectra to rest frame wavelength as

$$\lambda_{rest} = \frac{\lambda_{obs}}{1+z}, \tag{3.1.1}$$

where λ_{rest} is rest frame wavelength and λ_{obs} is observed frame wavelength.

[3] https://en.wikipedia.org/wiki/Python_(programming_language)

3. We define a function `Flux` which reads in spectrum of a galaxy and gives flux values and corresponding wavelength values within given wavelength range. Using this function, we store the flux values corresponding to line as well as continuum regions in different lists. Another function `Error` reads sigma errors from third row of spectrum fits file and give a list of errors for a given wavelength range.

4. We define a function `Cont` which estimates the value of continuum flux by fitting a line with two continuum regions so as to interpolate the continuum flux values in line region. We use `curve fit`[4] to perform linear fitting. From comparison with Goto et al. (2003a), we find that excluding errors on flux data points in linear fitting process gives more consistent values of equivalent widths. Thus we do not take into account flux errors when fitting the continuum. This procedure gives fitted continuum flux value at every point in line region as well as continuum regions.

5. We define a function `EWidth` to calculate rest frame equivalent width as

$$EW = \sum_i \frac{F_{c,i} - F_{\lambda,i}}{F_{c,i}} (\Delta\lambda_i), \tag{3.1.2}$$

where $F_{c,i}$ and $F_{\lambda,i}$ refer to continuum flux and line flux respectively, i is the index which runs over all rest frame wavelengths in line region.

6. We calculate the errors in rest frame EW using error propagation method as

[4] `Curve fit` function fits a function model defined by the user to data points. It finds the residuals which are the differences between fitted values and data points. We perform fitting in iteration until the sum of squared residuals is minimized and the best fit parameters are returned as output (https://docs.scipy.org/doc/scipy/reference/generated/scipy.optimize.curve_fit.html)

$$\Delta EW = \sqrt{\sum_i (1 - \frac{F_{\lambda,i}}{F_{c,i}})^2 \times \Delta\lambda_i^2 \times (\frac{\sigma^2_{F_{c,i}}}{F^2_{c,i}} + \frac{\sigma^2_{F_{\lambda,i}}}{F^2_{\lambda,i}})}, \tag{3.1.3}$$

where $F_{c,i}$ and $F_{\lambda,i}$ refer to continuum and line flux respectively and $\sigma_{F_{c,i}}$ is the average of all flux errors corresponding to two continuum regions.

3.1.2 Procedure Testing and Validation

We compare our equivalent width measurements with the measurements from Goto et al. (2003a) to check the validity of our code. Here we discuss the results of that comparison.

3.1.2.1 Comparison of EW(Hδ) values

We calculate the relative differences between our measured EWs and EWs from Goto et al. (2003a) as

$$Rel_{\rm diff} = \frac{EW_{\rm Goto} - EW_{\rm measured}}{EW_{\rm Goto}}. \tag{3.1.4}$$

The errors in relative differences between the measured EWs and EWs from Goto et al. (2003a) are calculated as

$$\Delta Rel_{\rm diff} = Rel_{\rm diff} \times \sqrt{\frac{\sigma^2_{EW_{\rm measured}}}{EW^2_{\rm measured}} + \frac{\sigma^2_{EW_{\rm Goto}}}{EW^2_{\rm Goto}}}. \tag{3.1.5}$$

Figure 3.3 shows the distribution of relative differences between our EW measurements and the ones from Goto et al. (2003a) as a histogram. The relative differences for EW(Hδ) lie within -0.1 to

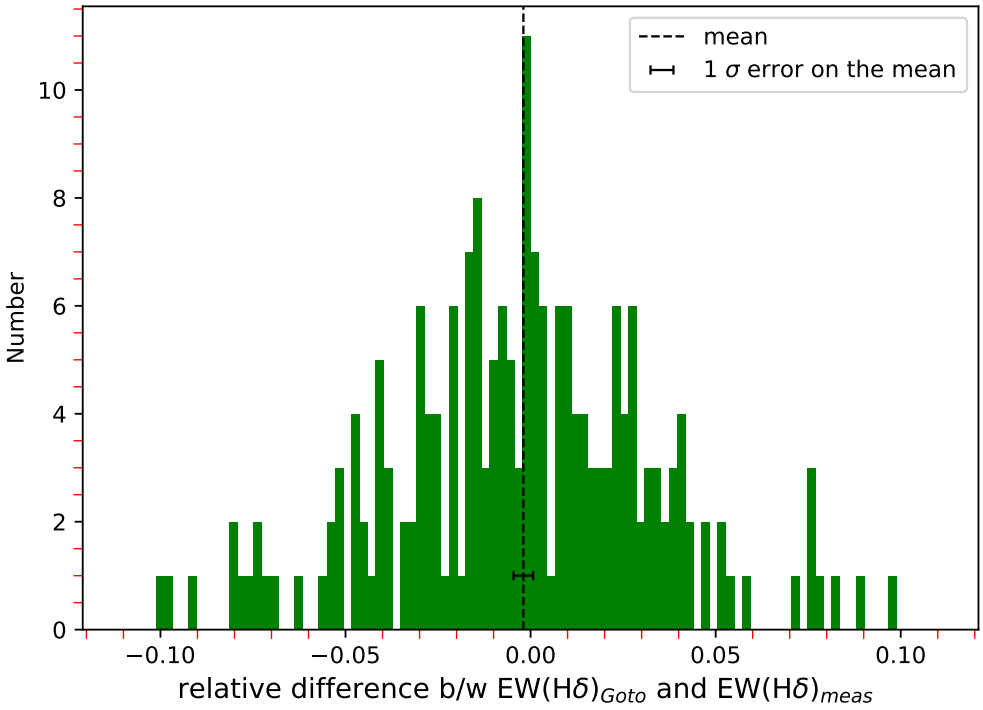

Figure 3.3: Histogram showing distribution of relative differences for EW(Hδ). Black dashed line represents the mean and black error bar represents 1 σ error on the mean.

0.1 range. The positive and negative values for relative differences indicate that our EW values are smaller and larger as compared to Goto et al. (2003a) respectively. The mean of the distribution is -0.0019 ± 0.0027, 0.7 σ away from zero.

The variation of relative differences with published EW values, redshift and signal to noise ratio shows no trend (Figures 3.4 and 3.5). The relative differences between two EW measurements may arise due to different fitting techniques used for continuum fitting process and also the fact that we do not correct our EW measurements for emission line filling while Goto et al. (2003a) does this correction.

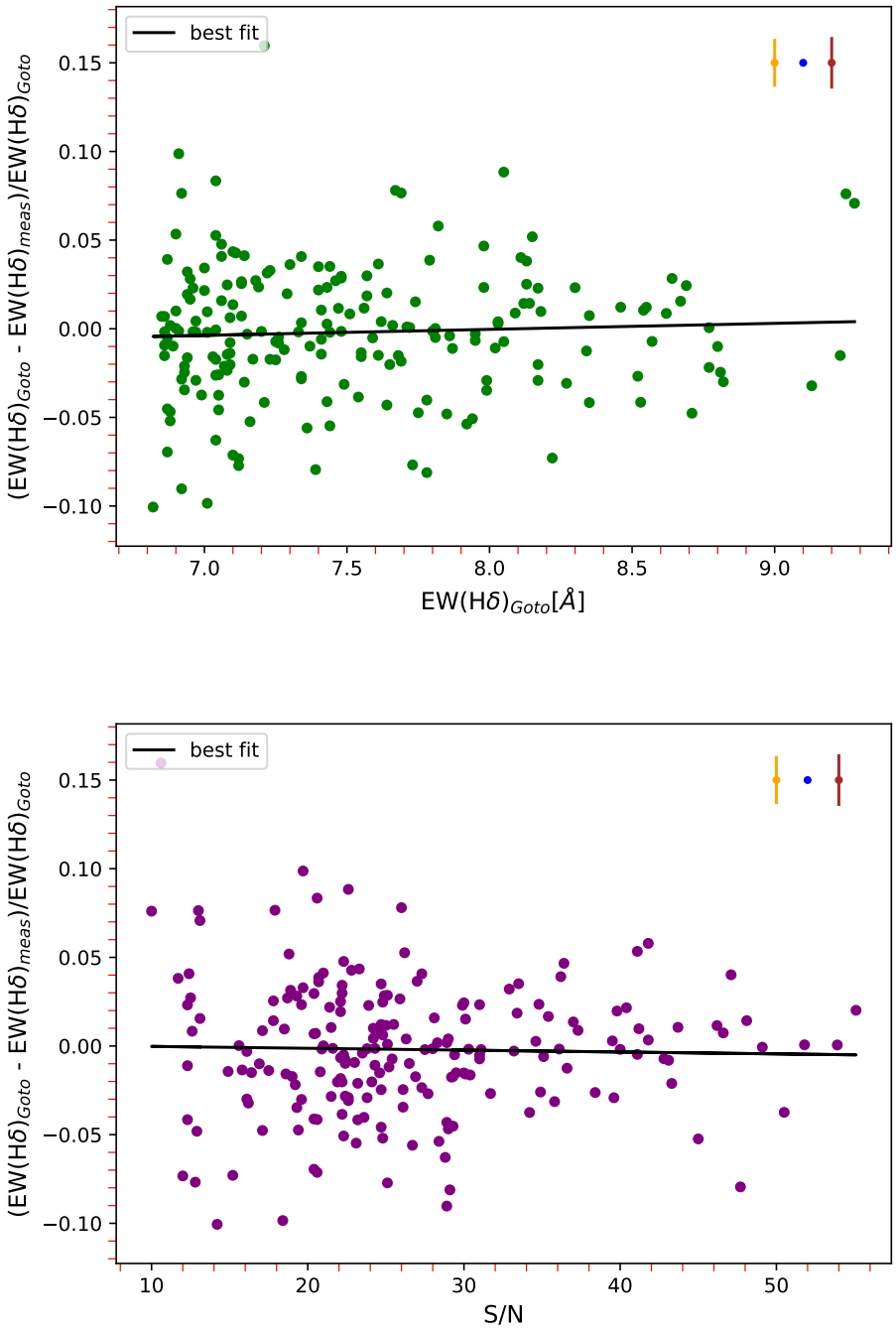

Figure 3.4: Variation of relative differences between our EW(Hδ) measurements and the ones (EW(Hδ)$_{Goto}$) from Goto et al. (2003a) as a function of different parameters. Top: Relative differences as a function of EW(Hδ)$_{Goto}$. Green points represent the relative differences with the black line as the best fit to these data points. Orange, blue and brown error bars in top right corner represent average absolute errors corresponding to relative differences within three relative difference bins: -0.1 to -0.05, -0.05 to 0.05 and 0.05 to 0.15 respectively. Bottom: Purple points represent the relative differences as a function of signal to noise ratio (S/N) with black line as the best fit to these points. Color scheme for error bars is the same as top panel.

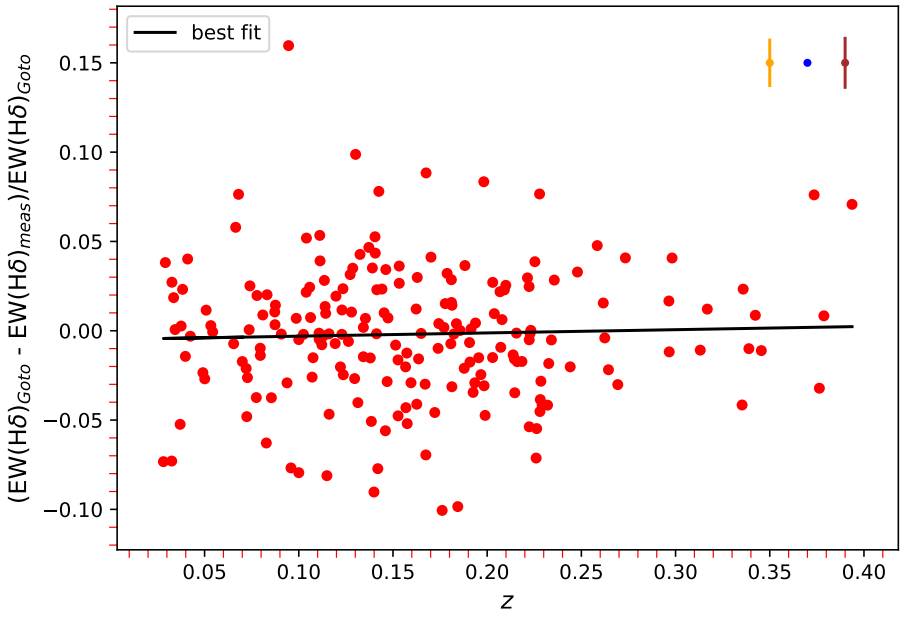

Figure 3.5: Continuation of Fig 3.4 showing relative differences vs. redshift. Red points represent relative differences with black line as the best fit. Color scheme for error bars is the same as in Figure 3.4.

Emission filling is Hδ emission present at the bottom of Hδ absorption line, thus reduces the equivalent width of Hδ spectral line. To investigate if emission filling is responsible for the relative differences between our measurements and measurements from Goto et al. (2003a), we correct our EW(Hδ) measurements from test sample by adding average value of emission filling factor (0.485 Å) from Goto et al. (2003a) to these measurements. Emission filling does not decrease the absolute differences between our EW measurements and the ones from Goto et al. (2003a). This shows that the relative differences do not arise because of emission filling and that we do not need to correct our measurements for emission filling.

3.1.2.2 Comparison of EW([OII]) values

We calculate the relative differences between measured EW([OII]) and EW([OII]) from (Goto et al. 2003a). Top panel of Figure 3.6 shows the distribution of relative differences as a histogram. The relative differences lie within the range of (-2,3) except for the region where -0.5 < EW([OII])$_{Goto}$ < 0.5. In this region, the relative differences increase upto a value of 10. The value of mean is 0.511 ± 0.266 and is 1.9 σ away from zero. The large positive value of mean may be due to large relative differences in -0.5 < EW([OII])$_{Goto}$ < 0.5 region. These large relative differences are due to low values of EW([OII]) in this region. The strength of [OII] emission line is at the same level as the noise which can affect the corresponding measurements. However, measured EW([OII]) values are consistent with EW([OII])$_{Goto}$ values within corresponding errors (Figure 3.7). Our EW([OII]) errors are smaller than errors from Goto et al. (2003a) as this study includes external errors and errors for emission filling correction. Goto et al. (2003a) computes external errors using the distribution of differences between EW([OII]) values measured from repeated observations of 11538 galaxies in

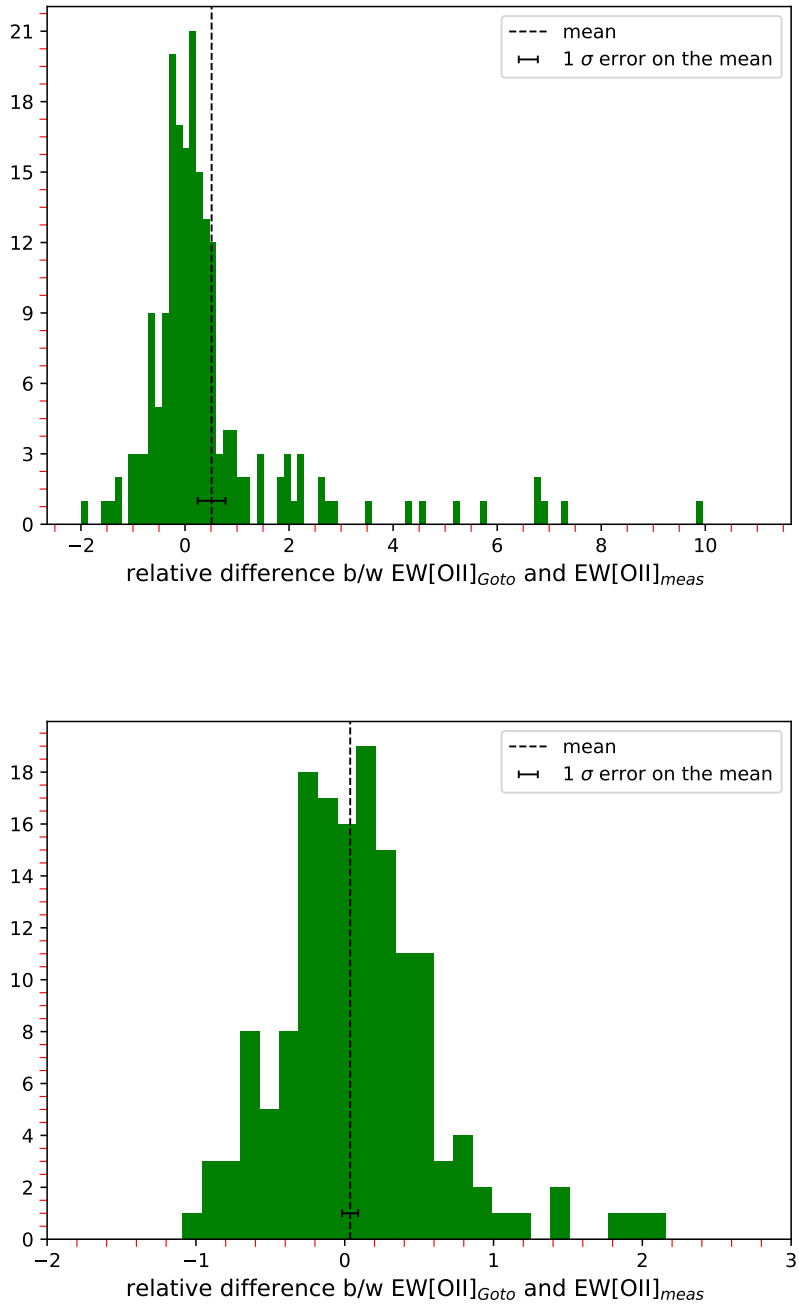

Figure 3.6: Top: Green histogram shows the distribution of relative differences between our measured EW([OII]) and measurements from Goto et al. (2003a). Black dashed line represents the mean value and black error bar represents 1 σ error on the mean. Bottom: Histogram shows the distribution of relative differences after ignoring values within -0.5 < EW([OII])$_{Goto}$ < 0.5 region. Color scheme is same as top panel.

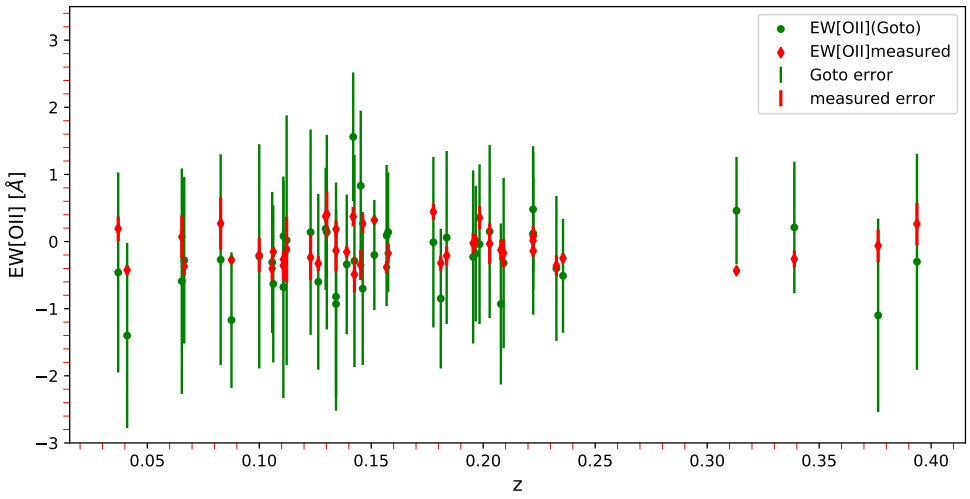

Figure 3.7: Comparison of our EW([OII]) measured errors and EW([OII]) errors from Goto et al. (2003a) as a function of redshift. Red color represents our EW([OII]) measurements and corresponding errors and green color represents EW([OII]) measurements and corresponding errors from Goto et al. (2003a).

their catalog. We do not have repeated observations and we also do not correct for emission filling, hence we do not include these additional error terms in our analysis.

based on differences

We ignore the relative differences between -0.5< EW([OII])$_{Goto}$ < 0.5 and again calculate the mean. The mean value changes to 0.036 ± 0.053 after ignoring the values between -0.5< EW([OII])$_{Goto}$ < 0.5 (bottom panel of Figure 3.6). The mean is 0.6 σ away from zero. This confirms that the positive mean in top panel of Fig 3.6 is due to relative differences within -0.5 < EW([OII])$_{Goto}$ < 0.5 region. There is no noticeable trend for variation of absolute differences between our EW([OII]) measurements and published EW([OII]) values from Goto et al. (2003a) with published EW([OII]), z and S/N within large average error (Figures 3.8 and 3.9).

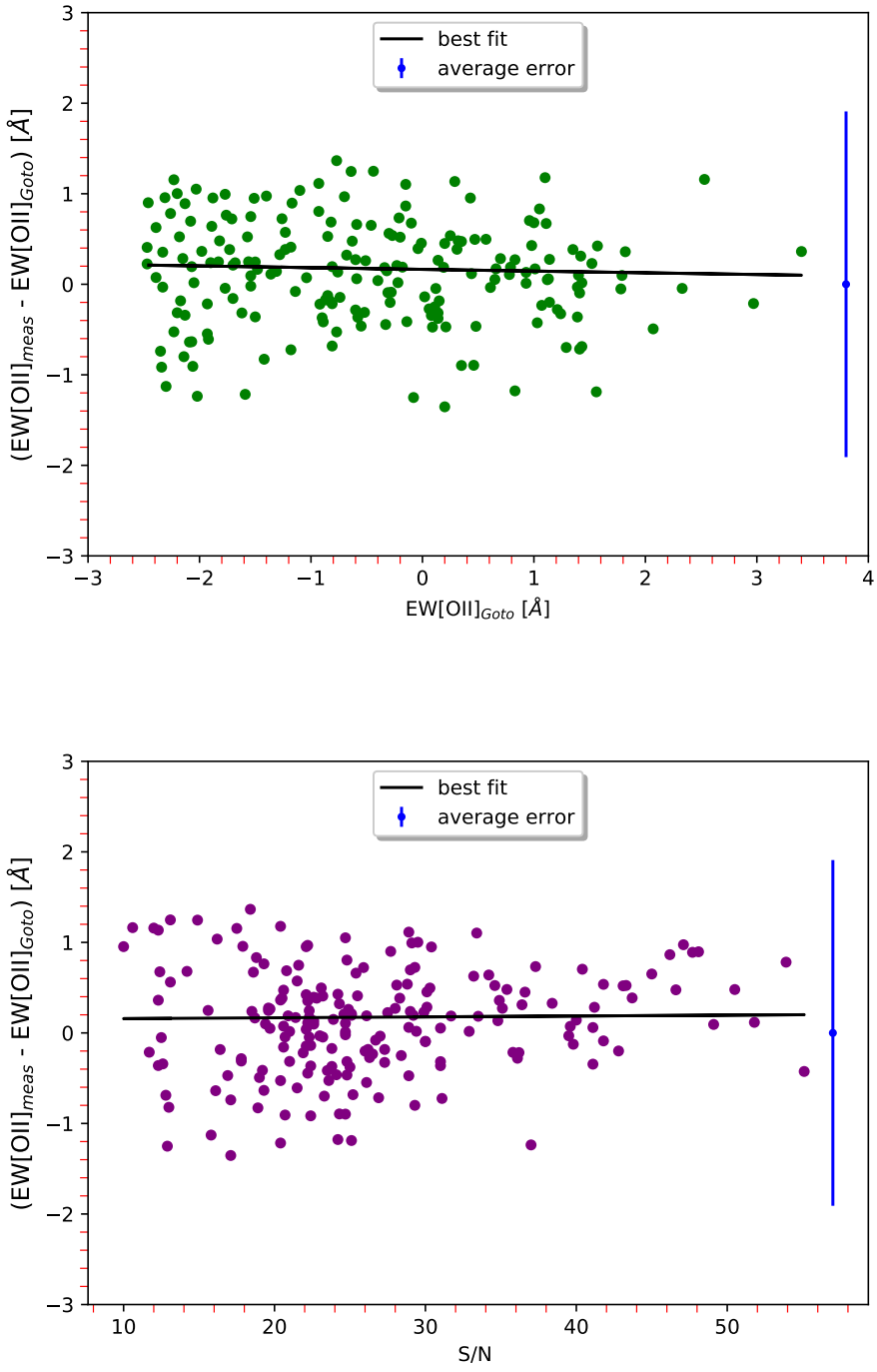

Figure 3.8: Variation of absolute differences between measured EW([OII]) and EW([OII]) calculated by Goto et al. (2003a) as a function of different parameters. Top: Absolute differences vs. EW([OII])$_{Goto}$. Green points represent the absolute differences with black line as the best fit to these data points. Blue error bar represents the average error corresponding to these absolute differences. Bottom: Purple points represent the absolute differences as a function of S/N with black line as the best fit. Error bar has the same meaning as top panel.

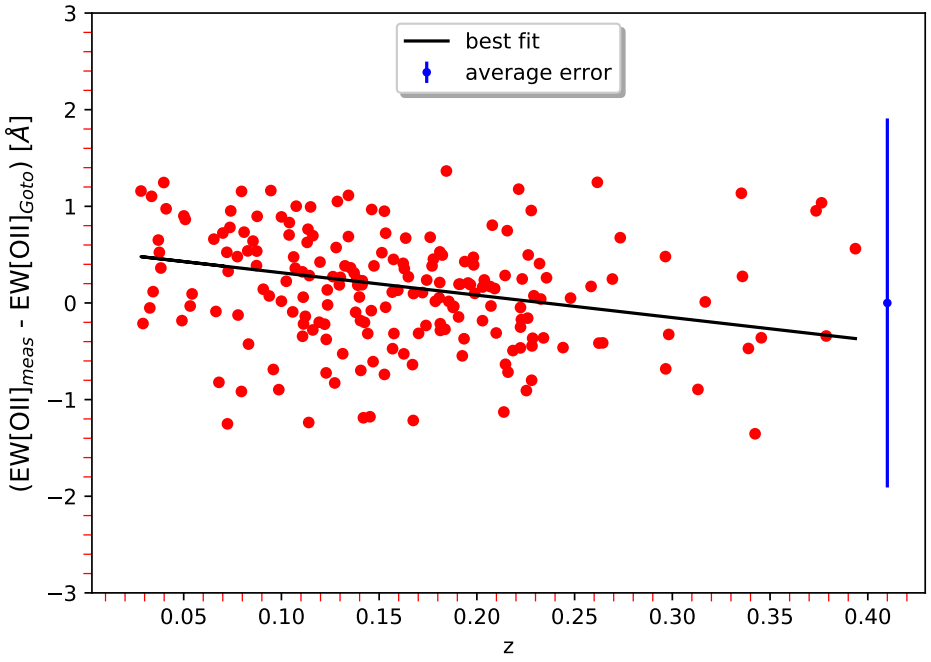

Figure 3.9: Continuation of Figure 3.8 for relative differences vs. z. Red points represent relative differences with black line as the best fit. Error bar has same meaning as in Figure 3.8.

3.2 Final SHELS F2 E+A sample

We use the same procedure as described above (based on SDSS galaxies) to compute EW values for SHELS F2 galaxies because SDSS and SHELS have similar spectral resolution. We select a sample of ~ 3064 PSB galaxy candidates from 17,343 SHELS spectra and 2643 SDSS spectra based on miminum EW condition on their EW(Hδ) measurements. However, after visual inspection we reject ~ 98% of those candidates. Here we provide details about the selection of our final SHELS F2 sample.

3.2.1 Conditions on EW values

We use flux summing method (Section 3.1.1.1) to find EW(Hδ_{nar}), EW(Hδ_{wide}), EW([OII]), EW(Hα) and corresponding EW errors for galaxies in SHELS F2 field at $z > 0.01$ with line and continuum regions from Table 3.1. The equivalent width measurements for [OII] spectral line are noisy and not robust (Section 3.1.2.2). We decide to perform visual inspection to confirm [OII] measurements. We choose ~ 3000 galaxies from 17,343 SHELS F2 spectra for visual inspection based on following condition: EW(Hδ_{wide}) - EWerr(Hδ_{wide}) > 4 Å. To extend our sample, we additionally select ~ 64 galaxies from ~ 2643 SDSS spectra for visual inspection based on the same condition.

We do not correct our EW values for emission filling as explained in Section 3.1.2.1. As a result, we might miss some galaxies using the above condition where the emission filling is more dominant than Hδ absorption. Galaxies with strong emission filling are more likely to have ongoing star formation even if the rate of star formation is low and hence are not the prime candidates for

our E+A sample. Also, the correction for emission filling is only going to increase our EW(Hδ) measurements and hence E+A sample selected by above two conditions would still be valid. Hence, not doing corrections for emission filling in our EW(Hδ) measurements does not affect our E+A sample.

3.2.2 Visual inspection

We visually inspect the spectra of all galaxies selected from Section 3.2.1 to confirm the absence of [OII] and Hα spectral lines. We can visually inspect Hα spectral lines only for galaxies with z < 0.37 because Hα lies beyond observed wavelength range for more distant galaxies. Visual inspection sometimes fails when the spectral lines are very weak and it becomes hard to accept or reject the presence of the spectral line. We rely on EW([OII]) measurements in the spectra where visual inspection fails to confirm the absence or presence of [OII] line (Figure 3.10). We find some spectra with emission filling confirming that our EW condition (from Section 3.2.1) is conservative and also includes galaxies with emission filling (Figure 3.11).

We also find spectra which do not show the presence of Hδ spectral line on visual inspection but have EW(Hδ) > 4 Å (Figure 3.12). These spectra indicate that a sample selected merely on the basis of $(EW)_{wide}$ measurements is likely to have galaxies misidentified as post-starburst. Hence, visual inspection is a necessity to select a pure sample of post-starburst galaxies. Our final sample has 48 post-starburst galaxies selected by the condition on EW(Hδ_{wide}) followed by visual inspection. Out of 48, 41 have MMT/Hectospec spectra only , 5 are SDSS galaxies and 2 galaxies have both MMT/Hectospec and SDSS spectra.

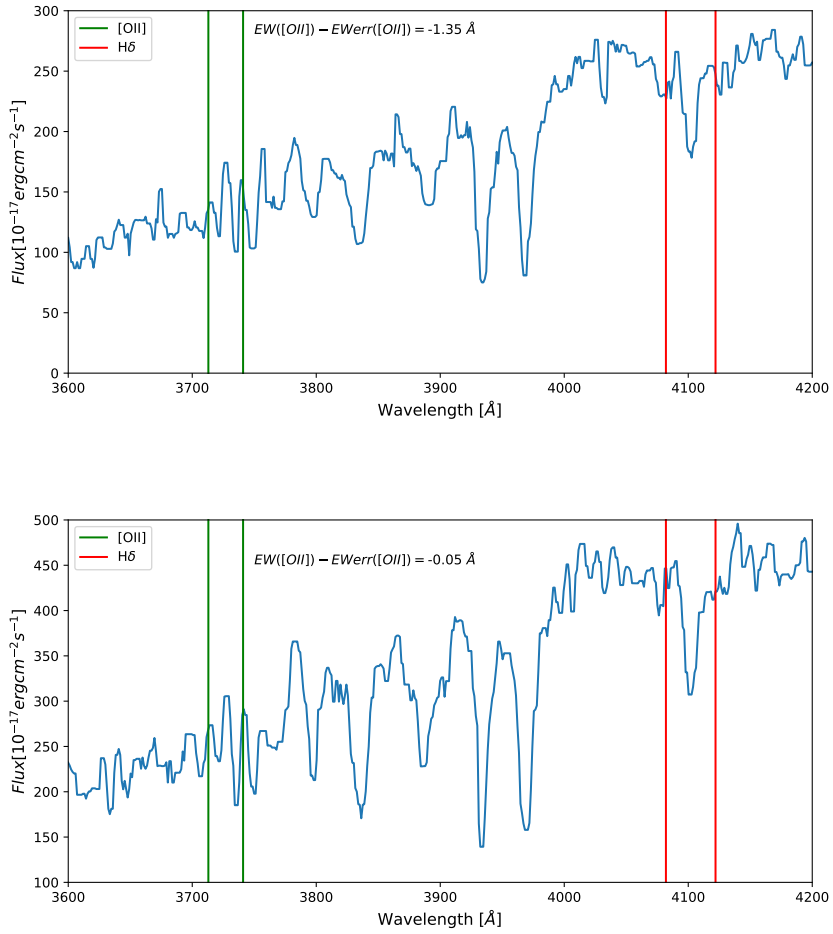

Figure 3.10: Spectra of two galaxies from SHELS F2 field having weak [OII] spectral lines (shown within green lines) and strong Hδ lines (shown within red lines). The presence of [OII] line is hard to detect visually as it lies within noise level. The negative EW measurements (written within) indicate the presence of [OII] line.

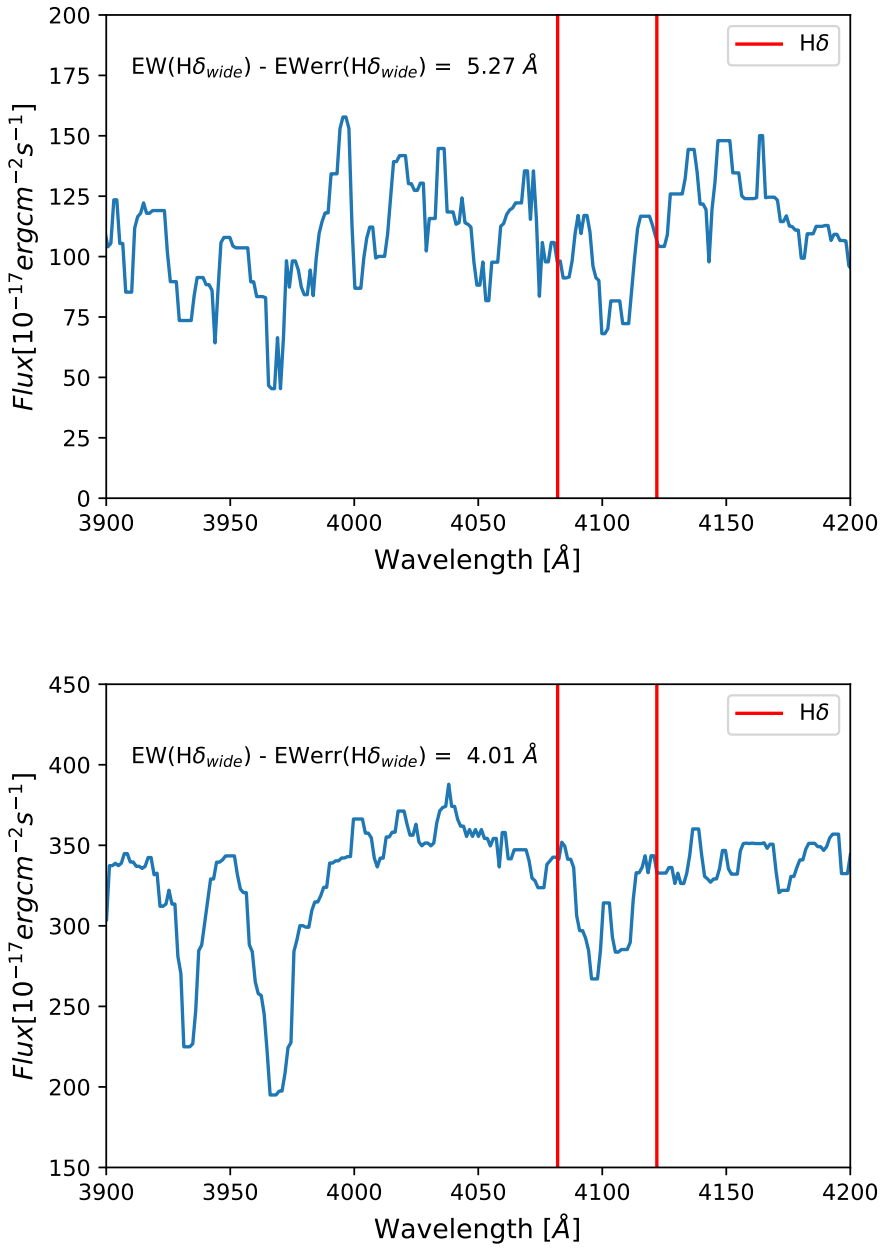

Figure 3.11: Spectra of two galaxies from SHELS F2 field having emission filling in Hδ spectral line (shown within red lines). Hδ spectral line is strong in both spectra visually but EW(Hδ) measurements indicate a weak Hδ line because of emission filling.

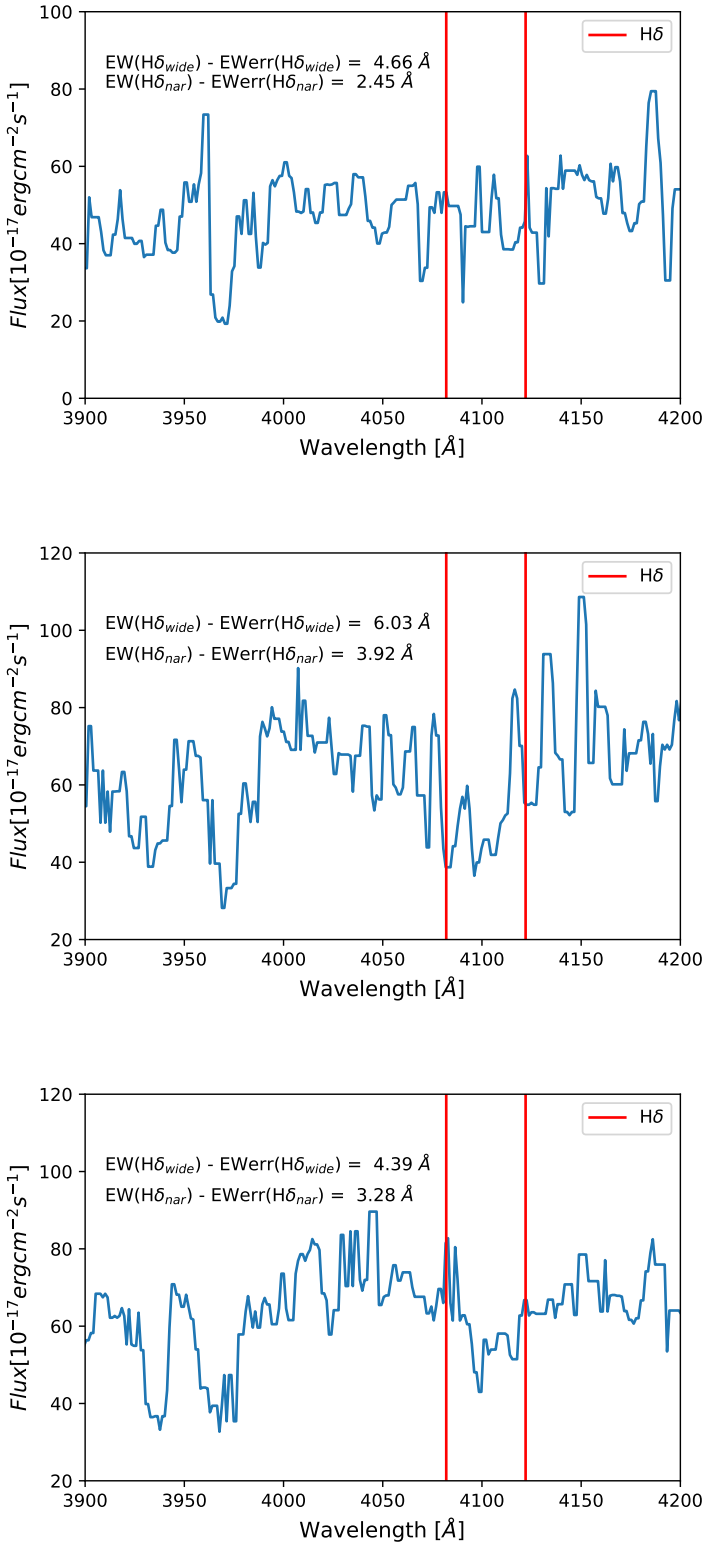

Figure 3.12: Spectra of three galaxies from SHELS F2 field having no Hδ spectral line (shown within red lines). On contrary, EW(Hδ) measurements indicate the presence of Hδ spectral line. There is a tiny peak of Hδ emission on top of Hδ absorption in each spectra.

Chapter 4

The abundance and internal properties of E+A galaxies at $z \leq 0.6$

In this chapter, we explore the internal properties and number density of E+A galaxies selected from the combination of minimum EW condition on Hδ spectral line and visual inspection (Section 3.2). We construct a mass-limited sample within $0.2 < z < 0.55$ in Section 4.1 and present the internal properties of both parent E+A sample (from Section 3.2) and mass-limited E+A sample in Section 4.4. We construct a sample in which each galaxy is observable over the complete redshift range ($0 < z < 0.6$) of the sample (volume-limited sample, Section 4.2). We compute number density of quiescent and E+A galaxies in our volume-limited sample (Section 4.3).

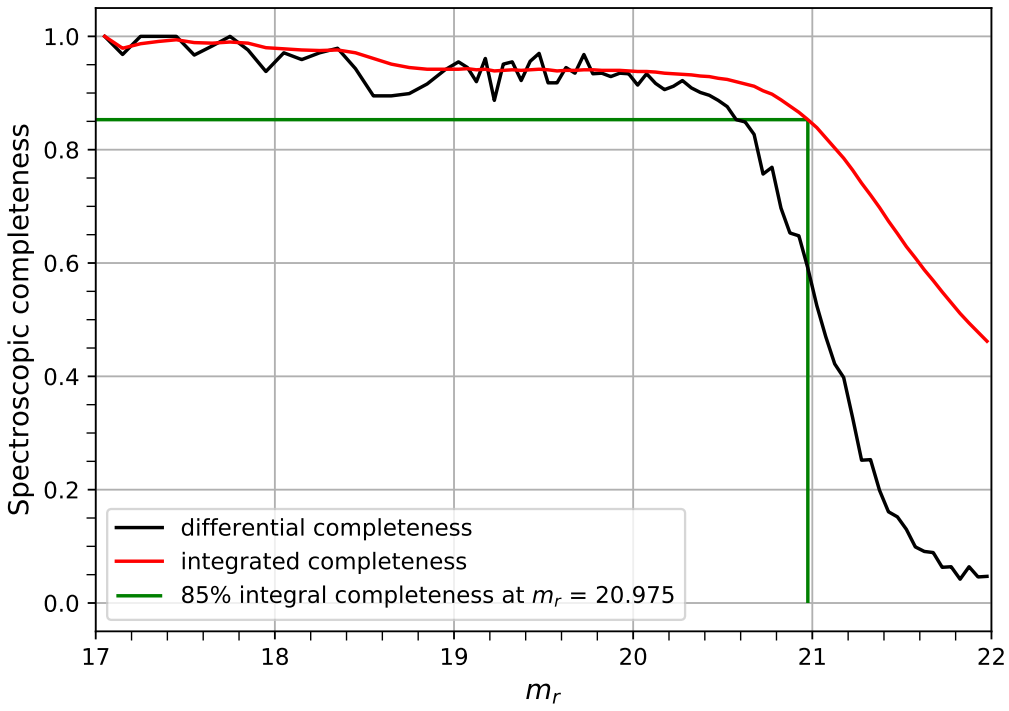

Figure 4.1: Spectroscopic completeness (in fraction) as a function of magnitude in SDSS $r-$band for SHELS F2 field. Red and black solid lines represent integrated and differential completeness as a function of magnitude respectively. Green line represents the apparent magnitude limit of 20.975 for 85% integrated completeness that we use in our analysis.

4.1 Constructing Mass-limited sample

4.1.1 Absolute Magnitude limit

The spectroscopic completeness varies as a function of apparent magnitude because of the limitations of the telescope and instrument used to observe galaxies. We can define spectroscopic completeness for each redshift survey as differential completeness and integrated completeness. Differential completeness is the ratio between the number of galaxies with recorded spectra (i.e, detected by the survey) and number of all possible photometric targets including the ones for which spectra was not recorded. Integrated completeness is the ratio between the number of galaxies with recorded spectra and number of all possible photometric targets integrated to a given apparent magnitude value.

SHELS has a magnitude limit of 20.725 in SDSS r band with 90% integrated completeness i.e. survey detects 90% of galaxies which have SDSS $r-$band magnitude values lower and equal to 20.725 (see Figure 4.1). We use apparent magnitude limit of 20.975 in SDSS $r-$band corresponding to 85% integrated completeness in SHELS (see Figure 4.1) to select a magnitude limited sample that includes the largest fraction of our E+A galaxy sample.

The decrease in the number of fainter galaxies in a magnitude limited survey as a function of redshift is known as Malmquist bias (Teerikorpi 1997; Butkevich et al. 2005). This selection effect is caused by the fact that the intrinsic brightness of the objects that can be observed increases with their distance (redshift in case of galaxy surveys). The intrinsic brightness of an object is measured as absolute magnitude. We change the magnitude limit to absolute magnitude limit as a function of redshift (z) using the following equation:

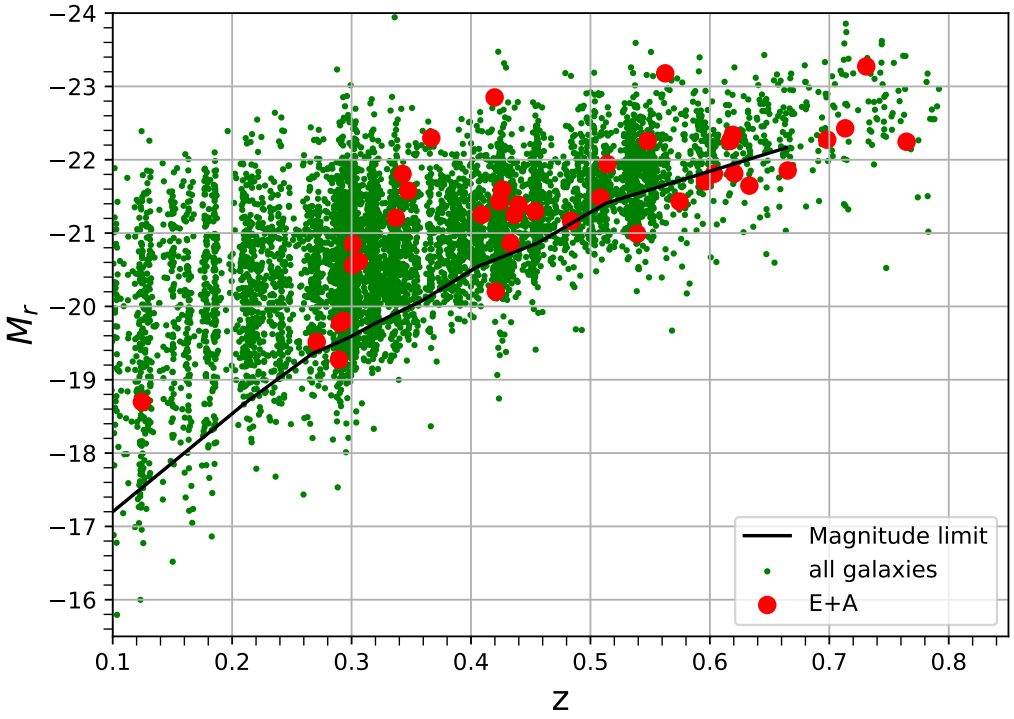

Figure 4.2: Absolute magnitude values in $r-$band as a function of redshift for all galaxies in SHELS F2 field (green points). The black solid line represents the absolute magnitude limit as a function of redshift. Red points represent E+A galaxies in our parent sample within $0.1 < z < 0.8$.

$$M_{R,\,\mathrm{lim}} = m_{R,\,\mathrm{lim}} - 5\log\left(\frac{D_L(z)}{10\mathrm{pc}}\right) - \bar{K}(z) - extinction. \tag{4.1.1}$$

Here $M_{R,\,\mathrm{lim}}$ is the absolute magnitude limit, $m_{R,\,\mathrm{lim}} = 20.975$ is the magnitude limit for 85% completeness in SDSS $r-$band. $D_L(z)$ is the luminosity distance at z calculated as

$$D_L = \frac{c}{H_0}(1+z)\int_0^z \frac{dz'}{\sqrt{\Omega_{\mathrm{M}}(1+z')^3 + \Omega_k(1+z')^2 + \Omega_\Lambda}} \tag{4.1.2}$$

(Hogg 1999). Cosmological parameters used in this equation are the same as mentioned in Section 1.5 and $\bar{K}(z)$ is the $k-$correction at z used to convert observed frame magnitudes to rest frame and is calculated as

$$\bar{K} = -2.5\log\left[(1+z)\frac{L_{(1+z)\nu}}{L_\nu}\right] \tag{4.1.3}$$

(Oke & Sandage 1968). Here L_ν is the luminosity at frequency ν assuming SED from five band SDSS photometry. We divide the redshift range of our survey $0.01 < z < 0.8$ into ten equally populated redshift bins. We find the absolute magnitude limit at the central redshift of each redshift bin using equations 4.1.2 and 4.1.3 for that bin. This procedure provides ten absolute magnitude limit values at the central redshifts of ten bins. We interpolate between ten absolute magnitude limit values to define a continuous function that describes absolute magnitude limit as a function of redshift (black solid line in Figure 4.2).

4.1.2 Transforming Absolute Magnitude limit to stellar mass limit

As stellar mass correlates with absolute magnitude, Malmquist bias implies that the stellar mass limit also increases with redshift. We translate absolute magnitude limit to stellar mass limit (i.e, the lowest stellar mass that we can observe within the survey) while taking into consideration the bimodality in galaxy population i.e., star-forming and quiescent galaxies. The light of star-forming galaxies is dominated by young massive stars (which are luminous but contribute less to stellar mass) and hence these galaxies have low mass-to-light ratio. Quiescent galaxies have both mass and light dominated by lower mass stars (which are fainter and contribute more to stellar mass because they are numerous) and that is why these galaxies have mass-to-light ratio which is stable and higher than in star-forming galaxies.

The first step to find stellar mass limit is to convert absolute magnitude limit into luminosity limit. We convert the absolute magnitude limit in each redshift bin to luminosity limit in SDSS $r-$band using the equation:

$$L_{r_{lim}} = 10^{\frac{(M_{r_{lim}} - M_{\odot,r})}{-2.5}}. \tag{4.1.4}$$

Here $L_{r_{lim}}$is the luminosity limit in $r-$band, $M_{r_{lim}}$ is the absolute magnitude limit in $r-$band, $M_{\odot,r}$ = 4.76 is SDSS $r-$band absolute magnitude for the Sun (Blanton et al. 2003).

The next step is to estimate the average mass-to-light ratio in each redshift bin separately for star-forming ($D_n4000 < 1.5$) and quiescent galaxies ($D_n4000 > 1.5$). Multiplying the average mass-to-light ratio with the luminosity limit in each bin gives the stellar mass limit for that bin. We interpolate between estimated stellar mass limit values to find stellar mass limit for the complete

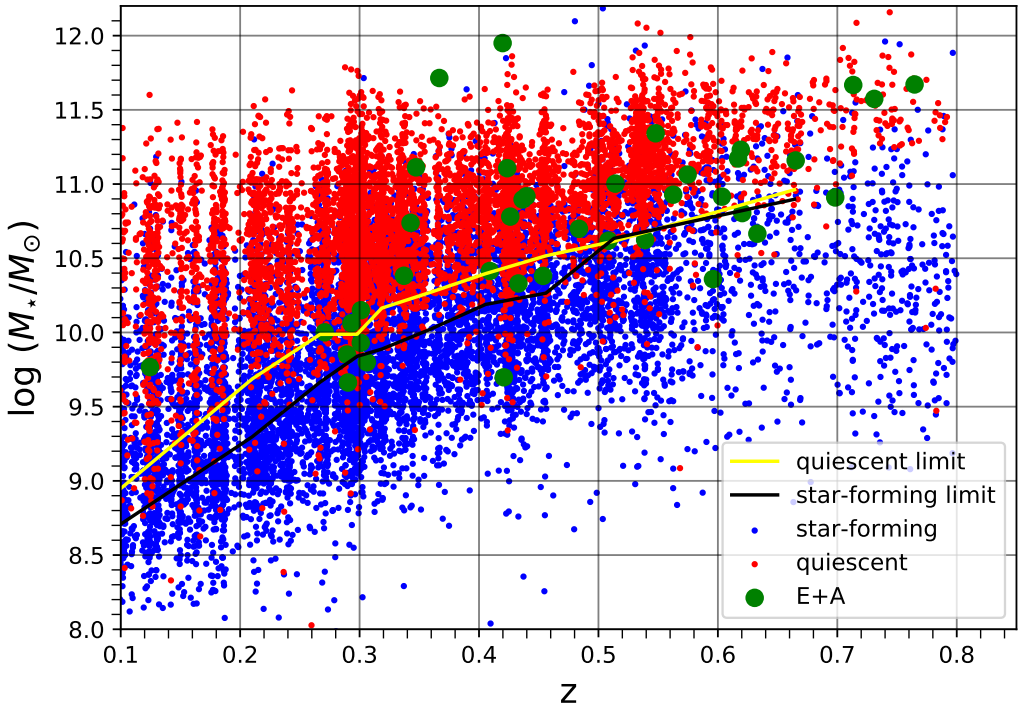

Figure 4.3: Stellar mass as a function of redshift for star-forming (blue points) and quiescent (red points) galaxies in SHELS F2 field. The black solid and yellow solid lines represent the stellar mass limit as a function of redshift for star-forming and quiescent galaxies respectively above apparent magnitude of 20.975 i.e., 85% completeness limit of the survey. Green points represent E+A galaxies in our parent sample within $0.1 < z < 0.8$.

redshift range ($0.1 < z < 0.8$) for star-forming and quiescent galaxies separately (see Figure 4.3).

Star-forming galaxies have a wider range of mass-to-light ratios and hence the stellar mass limit for star-forming galaxies is not well constrained. On the other hand, quiescent galaxies have narrower range of mass-to-light ratios which results in well defined stellar mass limit for quiescent population. In subsequent analysis, we choose to select galaxies which lie above the quiescent stellar mass limit as it is more conservative than star-forming stellar mass limit.

We trace $0.2 < z < 0.55$ because the clusters in F2 field are present within this redshift range. Our mass limited sample consists of 17 post-starburst galaxies, i.e. 65 % of all E+A galaxies within $0.2 < z < 0.55$ lie above apparent magnitude limit of 20.975 in SDSS $r-$band (Figure 4.1).

4.2 Volume-limited sample of E+A galaxies in SHELS F2 field

We construct a sample in which each galaxy is observable over the complete redshift range of the sample, known as volume-limited sample. Volume-limited sample allows us to test whether or not the measurements for mass-limited sample change in case no correction for missing mass is required. Previous studies of E+A galaxies adopt this approach at $z \sim 0.1$ (Goto et al. 2003a; Goto 2005a, 2007). We can extend this approach to higher redshift with our highly complete spectroscopic SHELS F2 E+A sample.

Our volume-limited sample consists of of 10 E+A galaxies with $\log(M_\star/M_\odot) \geq 10.8$ within $0.01 < z < 0.6$ (purple rectangle in Figure 4.4). We use this volume-limited sample to compute the number density of E+A galaxies (see Section 4.3), local densities around E+A galaxies (Section 5.4.2) and calculate E+A fractions in different environments (Section 6.1.1).

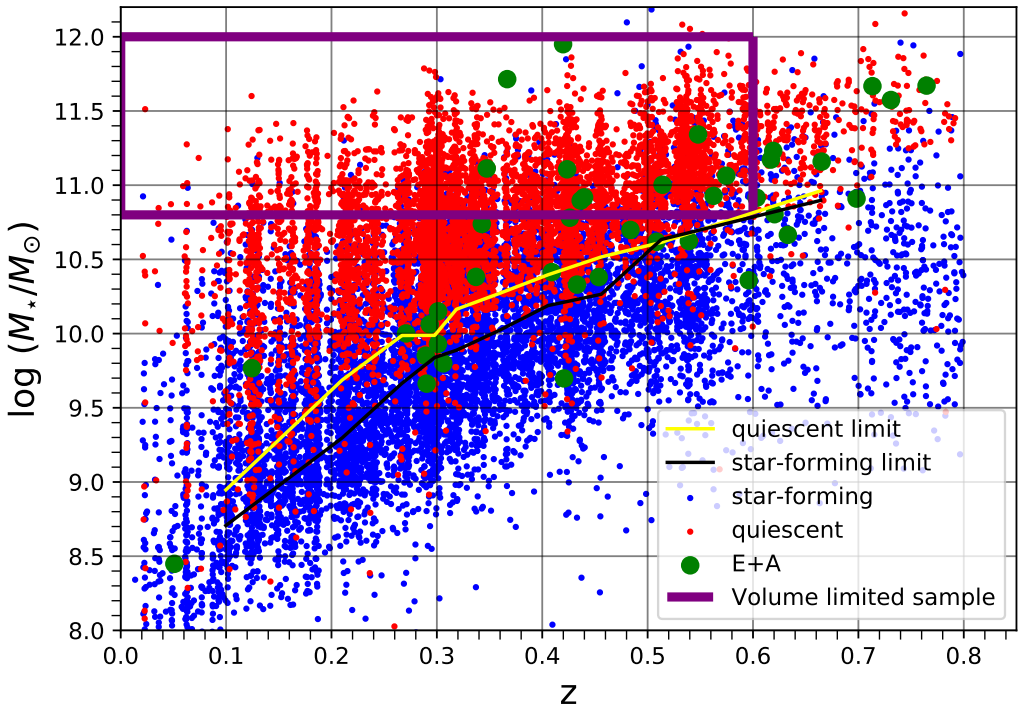

Figure 4.4: All symbols and colors have same meaning as in Figure 4.3. The purple rectangle shows SHELS F2 volume-limited sample consisting of 10 E+A galaxies within $0.01 < z < 0.6$. We exclude objects at $z < 0.01$ because of aperture effects.

4.3 Number density

One way to understand galaxy evolution is to study the change in number densities of quiescent and E+A galaxies as a function of redshift (Wild et al. 2016; Rowlands et al. 2018; Belli et al. 2019). To trace the change in number density over the redshift interval of our volume limited sample, we calculate number densities of E+A and quiescent galaxies in two redshift bins: $0 < z < 0.5$ and $0.5 < z < 0.6$. We choose these redshift bins to have maximum possible number of E+A galaxies in each bin. We also try other redshift bins and find that our results for E+A galaxies do not significantly change within error bars. However, we note that the results for quiescent galaxies do change (as we describe below). We use `Planck13` (Planck Collaboration et al. 2014) cosmology model from `astropy`[1] to calculate the volume corresponding to each redshift bin. To compute the number density (n) in each redshift bin, we divide the number of galaxies in that bin by the volume covered by that redshift bin in units of Mpc^{-3}, both for E+A and quiescent galaxies separately.

The errors in number density follow Poisson statistics. We assume Gaussian statistics for number density errors for quiescent galaxies because of large sample size (Poission statistics approach Gaussian statistics for large number of counts).The errors on $\log(n)$ for quiescent galaxies for N counts are $\log(e)/\sqrt{N}$. As number of counts are very low for E+A galaxies, we calculate 1σ upper and lower limits for number density of E+A galaxies using following equations (Gehrels 1986)

$$\sum_{x=0}^{N} \frac{\lambda_u^x e^{-\lambda_u}}{x!} = 1 - \mathrm{CL}, \tag{4.3.1}$$

[1] https://docs.astropy.org/en/stable/cosmology/index.html

$$\sum_{x=0}^{N-1} \frac{\lambda_l^x e^{-\lambda_l}}{x!} = \mathrm{CL} \quad (N \neq 0), \tag{4.3.2}$$

where N is number of counts (galaxies) in given bin, λ_u and λ_l are the upper and lower limits for Poisson statistics and CL = 0.8413 is the confidence interval for 1 σ upper and lower limits.

The number density of E+A galaxies in our volume-limited sample decreases by a factor of 1.13 and number density of quiescent galaxies increase by a factor of 1.58 from z = 0.6 to z = 0.01 (Figure 4.5). Rowlands et al. (2018) found the decrease in number density of E+A galaxies by a factor of 9 and increase in number density of quiescent galaxies by a factor of 1.58 from z = 0.6 to z = 0.1. Although there is slight difference between redshift ranges covered in the two studies, the change in quiescent number density in our measurements (58%) with decreasing redshift is equal to change in quiescent number density (58%) from Rowlands et al. (2018). However this percentage changes to 48% when we choose bins $0 < z < 0.3$ and $0.3 < z < 0.6$. Furthermore this percentage changes to 81% when we choose equal volume bins, $0 < z < 0.46$ and $0.46 < z < 0.6$.

Our E+A number density ($\log(n) = -5.71$) agrees with E+A number density ($\log(n) = -5.63$) from Rowlands et al. (2018) within error bars at $z \sim 0.25$ but our E+A number density ($\log(n) = -5.65$) at $z \sim 0.55$ is lower than E+A number density ($\log(n) = -4.70$) from Rowlands et al. (2018). The differences in E+A number densities at $z = 0.55$ may arise due to different selection criteria for E+A galaxies. Rowlands et al. (2018) use Principal Component Analysis (PCA) to select E+A galaxies with no cut on EW([OII]) which can result in contamination from star-forming/AGN galaxies in their sample unlike our E+A sample. This contamination is more at high redshift because of presence of more star-forming galaxies at higher z. Also, $z = 0.55$ is the central redshift corresponding to

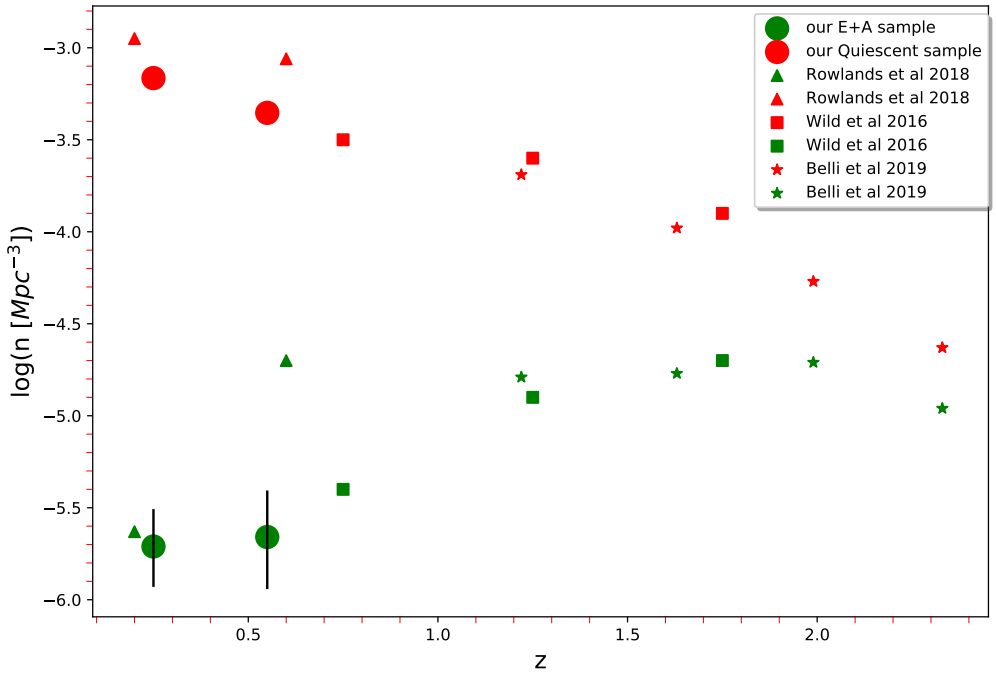

Figure 4.5: Number density of E+A and quiescent galaxies as a function of redshift. All green symbols represent number densities of E+A galaxies and all red symbols represent number densities of quiescent galaxies. Circles represent our number density measurements with black error bars representing 1 σ errors. Errors bars for our quiescent number density measurements are smaller than symbol size. We show errors for number density measurements from Rowlands et al. (2018) for comparison with our measurements; these errors are smaller than symbol size. The errors from high redshift studies such as Wild et al. (2016) and Belli et al. (2019) are also smaller than symbol size. Our errors bars for E+A number density values are bigger than other studies because of low number of counts for E+A galaxies in each redshift bin for our sample.

redshift bin ($0.5 < z < 0.6$) which lies at the edge of the redshift range that we probe in our analysis. We might be missing some galaxies at $z = 0.55$ because the completeness drops very steeply at the edge.

Another reason for the difference in our E+A number density measurements and E+A number density values from Rowlands et al. (2018) is the difference in stellar mass limits. Stellar mass limit for galaxies in Rowlands et al. (2018) is $\log(M_\star/M_\odot) > 10.6$, which is lower than stellar mass limit for our volume-limited sample ($\log(M_\star/M_\odot) > 10.8$). Rowlands et al. (2018) may have low mass E+A galaxies which are missing from our E+A sample. Different stellar mass limits would result in differences between our E+A number density measurements and E+A number density from Rowlands et al. (2018) both at $z = 0.25$ and $z = 0.55$.

Our measurements are also lower than number density measurements in high redshift studies (Wild et al. 2016; Belli et al. 2019), which have the same stellar mass limit ($\log(M_\star/M_\odot) > 10.8$) as our study. These differences might be real showing the evolution in number densities from high redshift to low redshift. However, some of the differences may arise due to different selection criteria for E+A galaxies. Wild et al. (2016) also uses PCA analysis and Belli et al. (2019) uses UVJ color diagram to select E+A galaxies. Overall, the positive and negative trends in number densities of quiescent and E+A galaxies as a function of redshift in our measurements are consistent with previous studies (Bell et al. 2004; Arnouts et al. 2007; Brown et al. 2007; Wild et al. 2009, 2016; Rowlands et al. 2018; Belli et al. 2019; Wild et al. 2020).

The growth rate of number density of quiescent galaxies is defined as

$$Gq = \frac{n_{2q} - n_{1q}}{t_2 - t_1}, \tag{4.3.3}$$

where n_{1q} is the number density of quiescent galaxies in the first bin ($0 < z < 0.5$), n_{2q} is the number density of quiescent galaxies in the second bin ($0.5 < z < 0.6$) and $(t_2 - t_1)$ is the time interval corresponding to the redshift difference between the central redshifts of two bins ($z = 0.55$ and $z = 0.25$) in units of Gyr. The total growth rate of number density of quiescent galaxies is $9.6 \times 10^{-5} \pm 2.2 \times 10^{-9}$ Mpc^{-3}Gyr^{-1} in our sample. This growth rate changes within $9.3 \times 10^{-5} \pm 10^{-8}$ Mpc^{-3}Gyr^{-1} and $1.3 \times 10^{-4} \pm 10^{-8}$ Mpc^{-3}Gyr^{-1} for different redshift bins we describe above.

In addition, we calculate the growth rate of number density of quiescent galaxies due to post-starburst galaxies with a visibility time of 250 Myr (Wild et al. 2009, 2016). Visibility time is the time scale during which post-starburst features are visible in galaxy spectra. We use the following equation

$$Gp = \frac{n_{2p}}{t_2 - t_1}, \tag{4.3.4}$$

where n_{2p} is the number density of E+A galaxies in second bin ($0.5 < z < 0.6$) and $t_2 - t_1 = 0.25$ Gyr is the visibility time. The number density growth rate of quiescent galaxies due to E+A galaxies is $(8.8 \times 10^{-6})^{+6.9\times10^{-6}}_{-4.2\times10^{-6}}$ Mpc^{-3}Gyr^{-1} in our sample. This growth rate does not change within error bars if we use maximum value of visibility time of 1 Gyr or different redshift bins.

Based on the difference in the number density growth rates, E+A galaxies contribute only $9\%^{+9\%}_{-7\%}$ to number density growth of quiescent galaxies. Studies related to higher redshifts (Wild et al. 2016; Belli et al. 2019) find significant contribution towards the growth in number density of quiescent galaxies from E+A galaxies. Belli et al. (2019) finds 50% growth of number density of quiescent galaxies from E+A galaxies at $z \sim 2$ with visibility time of 250 Myr. Wild et al. (2016) finds 100%

growth of number density of quiescent galaxies from E+A galaxies at $z \sim 0.5 - 1.5$ with visibility time of 500 Myr. We would need to decrease the visibility time by a large amount to significantly increase the contribution of E+A galaxies towards the number density growth of quiescent galaxies which cannot be justified. Our growth rate measurements are consistent with the idea that the contribution of E+A galaxies decrease towards the growth of quiescent galaxies with redshift from $z \sim 1$ to 0 and become almost negligible at $z \sim 0$ (Wild et al. 2009; Dressler et al. 2013; Rowlands et al. 2018).

4.4 Internal properties

We have measurements of stellar mass, D_n4000 index, Sérsic index (n) and circularized radius (R_c) for all galaxies in SHELS F2 catalog (Chapter 2). Physical values of all these parameters are available for 39/48 galaxies in our E+A sample and these 39 galaxies include all E+A galaxies (17) from our mass-limited sample. Figure 4.6 shows the distribution of different parameters as a function of redshift for these 39 E+A galaxies.

Left panels of Figure 4.6 show the range of stellar mass values and D_n4000 values of for E+A galaxies in our sample. The stellar mass values of E+A galaxies in our sample range within $9.5 < \log(M_\star)/M_\odot < 12$, consistent with other samples in literature (Vergani et al. 2010; Matharu et al. 2020). Around 67% of E+A galaxies in our sample have $1.2 < D_n4000 < 1.6$, within similar range as other studies such as Yamauchi & Goto (2005) at $z \sim 0.1$ and Vergani et al. (2010) at $0.5 < z < 1.2$. Some SHELS F2 E+A galaxies in our sample have extreme D_n4000 values ($D_n4000 > 1.8$). The reason for these unexpected values may be the presence of a skyline towards the blue side of 4000 Å break. Skyline subtraction may decrease the continuum level and hence increase the strength of

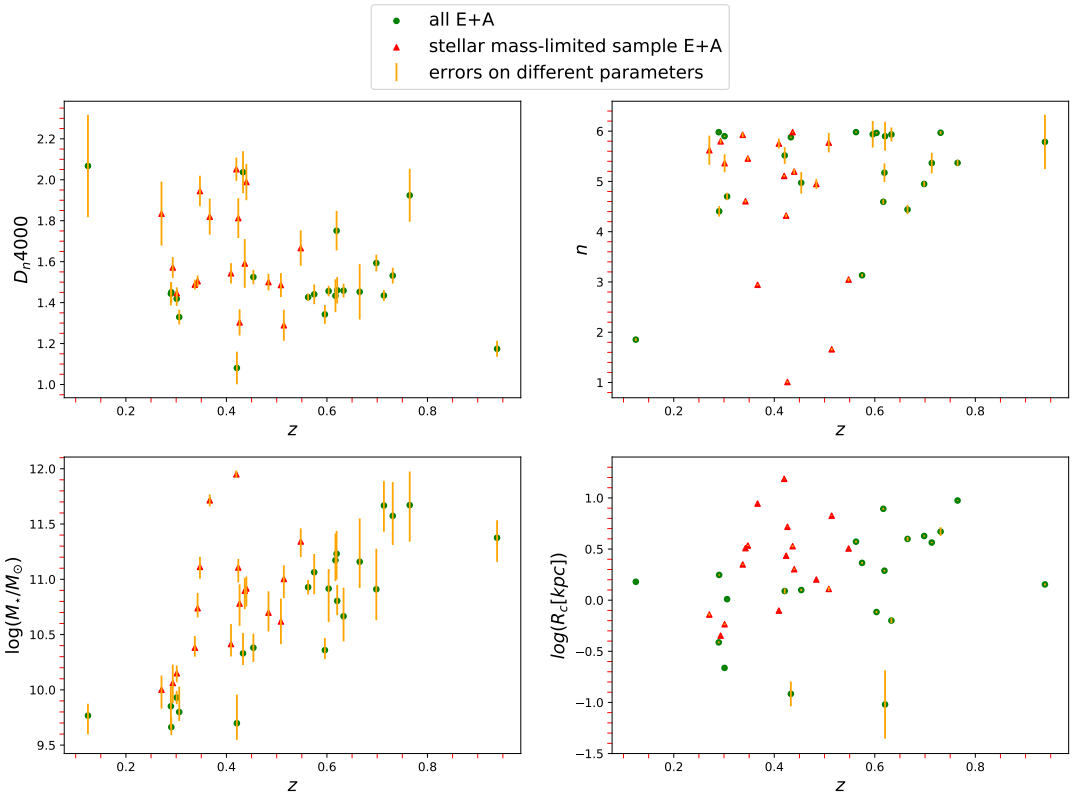

Figure 4.6: Distribution of internal properties of E+A galaxies as a function of redshift. First column: D_n4000 and stellar mass ($\log(M_\star/\mathrm{M}_\odot)$) measurements of E+A galaxies from top to bottom. Green points represent E+A galaxies and red triangles represent E+A galaxies in mass-limited sample. Yellow error bars represent the errors in different parameters. Second column: Sérsic index (n) and circularized radius ($\log(R_c)$) measurements of E+A galaxies from top to bottom. All symbols have same meaning as left panels. Error bars are smaller than symbol size for some parameters and are not visible.

D_n4000 index. The visual inspection of spectra for E+A galaxies with $D_n4000 > 1.8$ confirm the presence of a skyline in the blue side of 4000 Å break. We conclude that these unlikely high D_n4000 values for E+A galaxies are likely suffering from large uncertainties and thus are not as reliable as other D_n4000 measurements for the E+A sample.

Right panels of Figure 4.6 show structural parameters of E+A galaxies in our sample i.e. Sérsic index and circularized radii. Majority of E+A galaxies ($\sim 90\%$) in our sample have high Sérsic index values ($n > 3$) which indicate that these are bulge-dominated galaxies (Quintero et al. 2004; Blake et al. 2004; Balogh et al. 2005; Poggianti et al. 1999). Mean Sérsic index values of E+A galaxies, star-forming galaxies and quiescent galaxies with 1 σ errors on mean values are 4.62 ± 0.36, 2.6 ± 0.04 and 4.72 ± 0.02 respectively. Mean Sérsic index of E+A galaxies is consistent with mean Sérsic index value of quiescent galaxies within 1 σ errors, similar to the results of Almaini et al. (2017) and Matharu et al. (2020) at $z \gtrsim 1$.

Majority ($\sim 85\%$) of E+A galaxies in our mass-limited sample have a range of values for circularized radii: 0.45 to 15 kpc. Mean values of circularized radii with 1 σ errors on mean values for E+A, star-forming and quiescent in mass-limited sample are 3.63 ± 0.88 kpc, 3.90 ± 0.04 kpc and 3.48 ± 0.05 kpc respectively. Comparison of these mean values indicate that E+A galaxies in our sample have smaller sizes than star-forming galaxies and have similar size distribution as quiescent galaxies within error bars, similar to Almaini et al. (2017) and Matharu et al. (2020). This comparison does not take into account the fact that size depends on mass, which we explore further in Section 4.4.1.2.

4.4.1 Trends in spectroscopic and structural properties with galaxy stellar mass

We investigate the trends in different spectroscopic and structural properties with stellar mass for E+A galaxies and compare these with star-forming and quiescent galaxies in our mass-limited sample. This comparison provides an insight into the evolution from star-forming to quiescent galaxies via post-starburst phase.

4.4.1.1 Spectroscopic properties as functions of stellar mass

Figure 4.7 shows the distribution of all galaxies in mass-limited sample in the form of contours in D_n4000 vs. stellar mass plane with overplotted E+A galaxies. The trend in D_n4000 values of E+A galaxies with stellar mass is the same as for general galaxy population once the extreme values of $D_n4000 > 1.8$ are excluded - galaxies with older stellar populations are more massive (Gallazzi et al. 2005, 2014; Kauffmann et al. 2003c).

Figure 4.8 shows the distribution of all galaxies in mass-limited sample in the form of contours in EW(Hδ) vs. stellar mass plane with overplotted E+A galaxies, similar to other studies in literature at $z \sim 0.1$ (Kauffmann et al. 2003b,c). Since we do not expect galaxies with $D_n4000 > 1.5$ to have negative values of EW(Hδ) (negative EW values correspond to emission lines, Chapter 3), we visually inspect some of the spectra for these galaxies. Our code gives EW(Hδ) measurements with the errors that are at the same level as these EW(Hδ) measurements, and thus these measurements are not reliable. Our visual inspection shows that the reason for this are either very weak or non-existent Hδ absorption lines and/or the artifact of the skyline subtraction in the line or continuum region.

By definition, our E+A sample galaxies have EW(Hδ) values higher than most of star-forming and quiescent galaxy population. Quiescent galaxies have older stellar population with either very

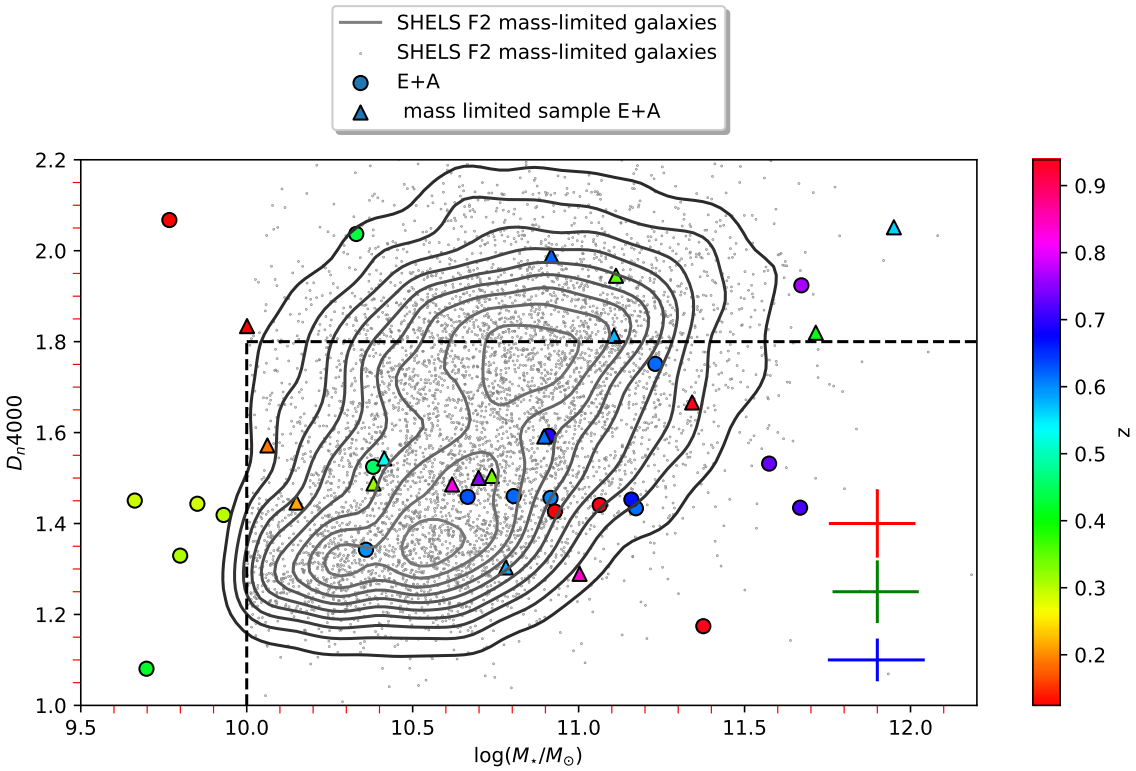

Figure 4.7: Distribution of star-forming and quiescent galaxies from mass-limited sample in D_n4000 vs. stellar mass plane with overplotted E+A galaxies. Gray contours and gray points represent galaxies in SHELS F2 mass-limited sample. Circles represent all E+A galaxies excluding mass-limited E+A galaxies and triangles represent mass-limited E+A galaxies. Circles and triangles are color coded by redshift (z). Red, green and blue error bars in bottom right corner represent average errors corresponding to quiescent, E+A and star-forming galaxies respectively. Black dashed lines mark the boundary for $D_n4000 > 1.8$ (which are uncertain) and $\log(M_\star/M_\odot) > 10$.

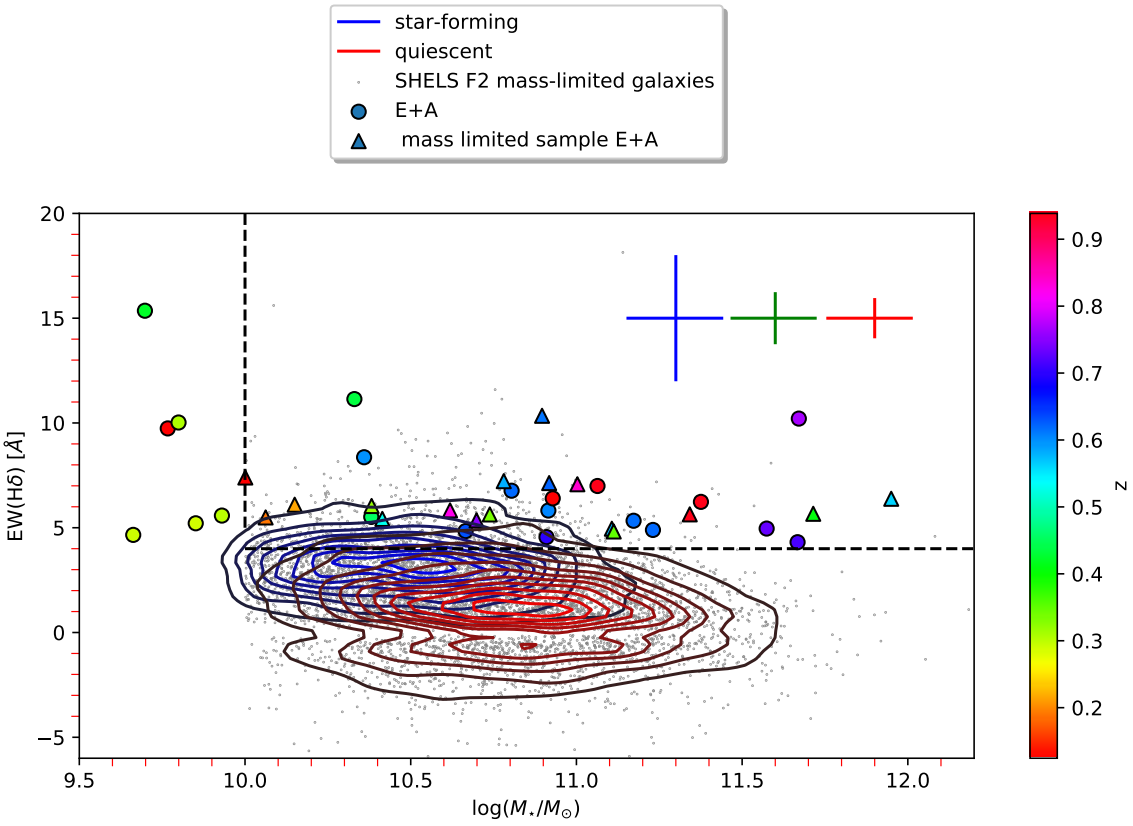

Figure 4.8: Distribution of star-forming and quiescent galaxies from mass-limited sample in EW(Hδ) vs. stellar mass plane with overplotted E+A galaxies. Blue and red contours represent star-forming and quiescent galaxies respectively. Gray points represent all galaxies in SHELS F2 mass-limited sample. Black dashed lines mark the boundary for region where we see a flat trend of EW(Hδ) with stellar mass. Colour-coding and symbol assignment for big symbols and average error bars is the same as in Figure 4.7.

low number or no A type stars resulting in lower EW(Hδ) than E+A galaxies. Stellar light of star-forming galaxies is dominated by O,B type hot stars and hence these galaxies have emission lines due to ionization of the ISM around these hot stars (unlike quiescent galaxies) along with weak Balmer absorption lines. Thus, the strength of Hδ absorption line decreases because of emission filling in star-forming galaxies. EW(Hδ) values of E+A galaxies in our sample show a flat trend with stellar mass within error bars except for the low mass ($M_\star < 10^{10} M_\odot$) end, where EW(H$\delta$) values show a decreasing trend with stellar mass. The flat trend of EW(Hδ) with stellar mass for E+A galaxies may be an artifact of minimum EW condition used on EW(Hδ) in selection criteria (i.e. EW(Hδ) > 4 Å).

Since there is a relation between D_n4000 and $\log(M_\star/M_\odot)$ as well as between D_n4000 and EW(Hδ), there should be a relation between D_n4000 and EW(Hδ). Figure 4.9 shows the distribution of all galaxies in mass-limited sample in the form of contours in EW(Hδ) vs. D_n4000 plane with overplotted E+A galaxies. Older stellar population (higher D_n4000) galaxies have lower EW(Hδ) values. The distribution of all galaxies from our mass-limited sample in EW(Hδ) vs. D_n4000 plane is similar to other studies in literature such as Kauffmann et al. (2003b,c) at $z \sim 0.1$ for SDSS galaxies and Gallazzi et al. (2014) at $z \sim 0.7$ based on Extended Chandra Deep Field South (E-CDFS) survey (Wolf et al. 2004). There is a slight decreasing trend of EW(Hδ) with increasing D_n4000 values for E+A sample[2], similar to Figure 11 of Balogh et al. (1999). To confirm this decreasing trend, we measure median EW(Hδ) values for E+A galaxies in two bins: $0 < D_n4000 < 1.5$ and $1.5 < D_n4000 < 1.8$. Median EW(Hδ) values in first ($0 < D_n4000 < 1.5$) and second bin ($1.5 < D_n4000 < 1.8$) are 6.2 Å and 5.5 Å respectively which suggests the decreasing trend of EW(Hδ) with D_n4000 for E+A galaxies.

[2]if we exclude E+A galaxies with $D_n4000 > 1.8$ as these measurements are uncertain

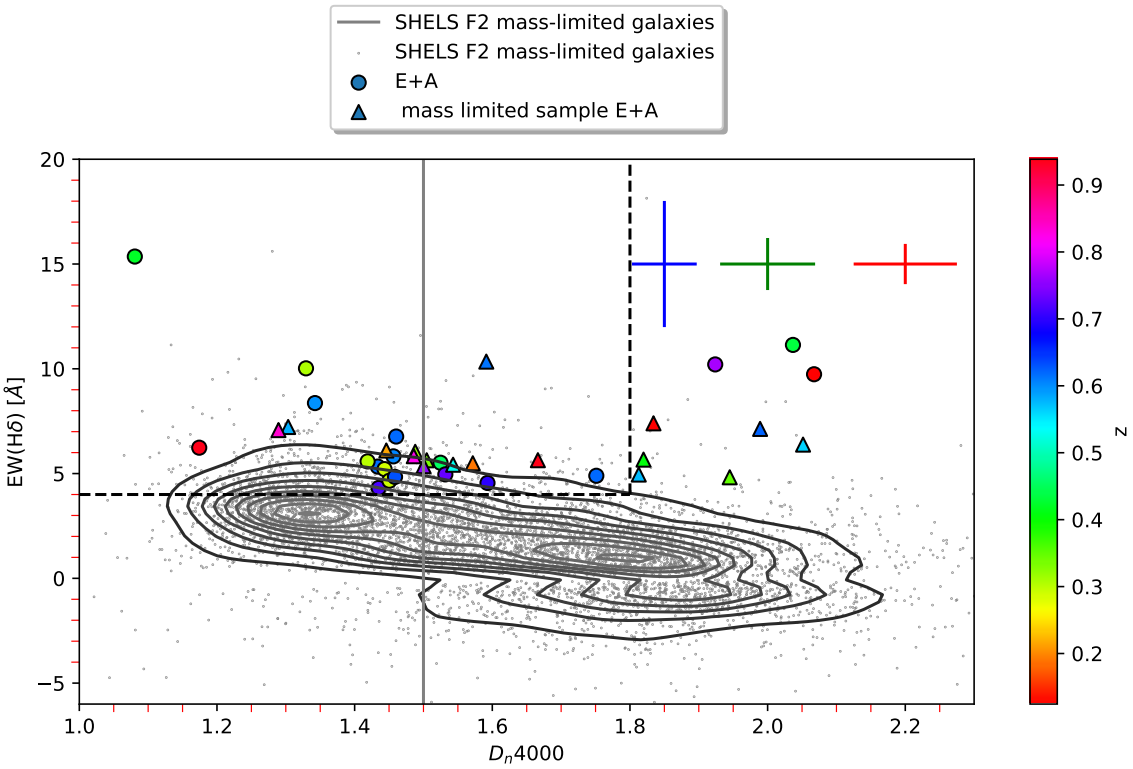

Figure 4.9: Distribution of star-forming and quiescent galaxies from SHELS F2 mass-limited sample in EW(Hδ) vs. D_n4000 plane with overplotted E+A galaxies. Gray vertical line marks the boundary ($D_n4000 = 1.5$) to divide star-forming ($D_n4000 < 1.5$) and quiescent galaxies ($D_n4000 > 1.5$). Black dashed lines mark the boundary for region in which D_n4000 values are certain and EW(Hδ) shows a decreasing trend with D_n4000. Symbols and color assignment is the same as in Figure 4.7.

Looking at the trends of spectroscopic properties with stellar mass, we conclude:

- Majority of E+A galaxies (67%) have D_n4000 values intermediate to both galaxy populations i.e. $1.2 < D_n4000 < 1.6$. This provides an evidence that E+A galaxies act as transitional state between star-forming and quiescent galaxies.

- By design, E+A galaxies have higher value of EW(Hδ) than both galaxy populations as these galaxies are abundant in A type stars. Star-forming galaxies have young stars (O,B type) while quiescent galaxies have old stars (K type) as explained previously. Star-forming and quiescent galaxies exhibit the trend of decrease in value of EW(Hδ) with increase in stellar mass. This trend becomes visible at $< 5 \times 10^{10} M_{\odot}$ for E+A galaxies.

4.4.1.2 Galaxy size - stellar mass relation

Previous studies have found that E+A galaxies have size-mass relation intermediate to star-forming and quiescent galaxies (Almaini et al. 2017; Matharu et al. 2020; Suess et al. 2021). Figure 4.10 shows the distribution of all galaxies in SHELS F2 mass-limited sample in the form of contours in EW(Hδ) vs. stellar mass plane with overplotted E+A galaxies. Star-forming galaxies are larger in size than quiescent galaxies within same stellar mass range, as shown in Damjanov et al. (2019).

E+A galaxies have smaller sizes than star-forming galaxies and cover the full range of sizes of quiescent population. The consistency of E+A galaxy sizes in our sample with quiescent population indicates that E+A galaxies contribute to the formation of quiescent galaxies (Zahid et al. 2016b, 2019).

Compact E+A galaxies act as progenitors of compact quiescent galaxies (Zahid et al. 2016b).

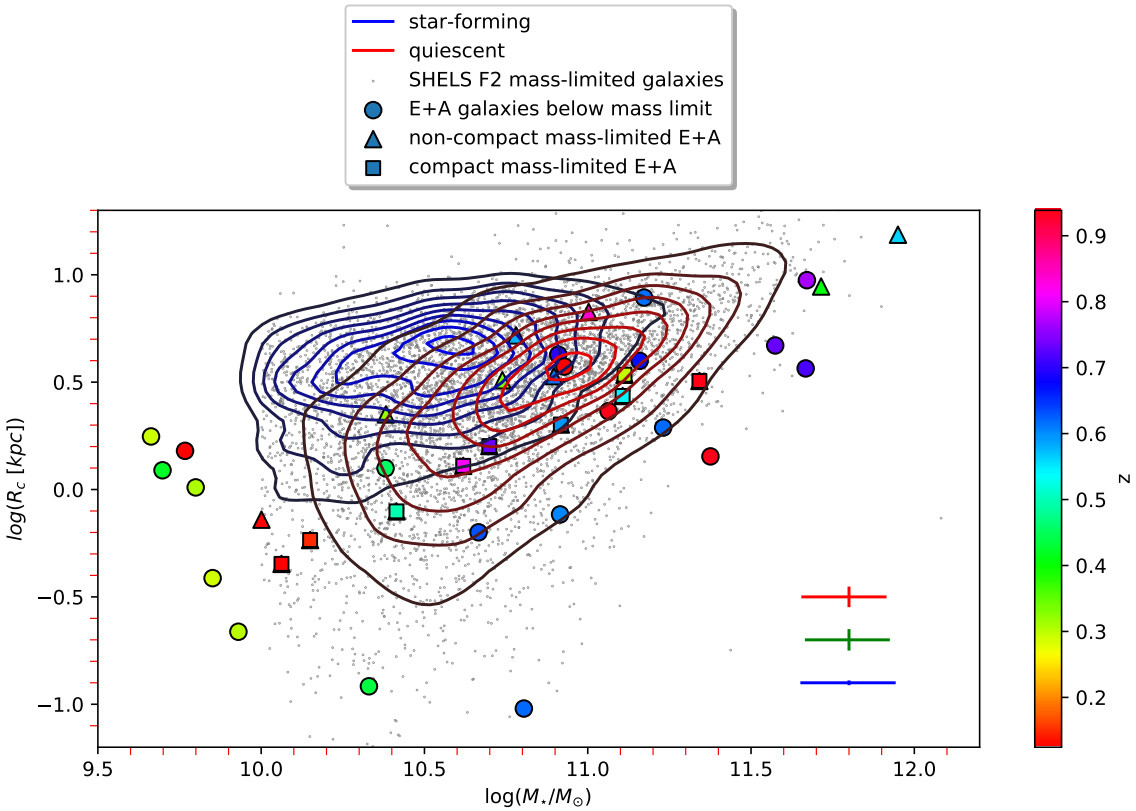

Figure 4.10: Distribution of star-forming and quiescent galaxies from SHELS F2 mass limited sample in circularized radius $log(R_c)$ vs. stellar mass plane with overplotted E+A galaxies. Blue and red contours represent star-forming and quiescent galaxies respectively. Circles represent E+A galaxies excluding mass-limited E+A galaxies, triangles represent non-compact mass-limited E+A galaxies and squares represent compact mass-limited E+A galaxies. All symbols are color coded by redshift (z). Error bars follow same color scheme as Figure 4.7.

Several studies have found that compact quiescent galaxies are formed at high redshifts ($z > 1$) and their number density rapidly declines at $z < 1$ (Trujillo et al. 2009; Taylor et al. 2010; van der Wel et al. 2014). Size growth of quiescent galaxies with decreasing redshift via minor mergers (Bezanson et al. 2009; Hopkins et al. 2009; Naab et al. 2009; Hilz et al. 2012; Oser et al. 2012) explains the decrease in number density of compact quiescent galaxies.

There are other studies which find that the number density of compact quiescent galaxies remains constant at $z < 1$ (Carollo et al. 2013; Damjanov et al. 2014, 2015). The constancy in number density of compact quiescent galaxies at $z < 1$ indicates that these galaxies must form at $z < 1$. We investigate the compactness of E+A galaxies from our mass-limited sample using the compactness criteria from Barro et al. (2013). We find that nine E+A galaxies in mass-limited sample have $\log(M_\star/Rc^{1.5}) > 10.3\ M_\odot kpc^{-1.5}$. Compact E+A galaxies in our sample provide a channel for the formation of new (young) compact quiescent galaxies at $z < 1$.

Non-compact E+A galaxies act as progenitors of large size quiescent galaxies. Quiescent galaxies grow more in size than stellar mass with decreasing redshift (Daddi et al. 2005; Trujillo et al. 2006; van der Wel et al. 2008; Damjanov et al. 2011; van der Wel et al. 2014). In addition to minor mergers, the size growth of red sequence includes the effects of the progenitor bias (van der Wel et al. 2009; Carollo et al. 2013). Progenitor bias refers to the growth of average galaxy size for quiescent population due to the addition of large newly quenched galaxies (including E+A) with decreasing redshift. Progenitor bias is the most significant at lower stellar masses [$< 5 \times 10^{10} M_\odot$] (Damjanov et al. 2019). At $0.2 < z < 0.6$, progenitor bias has low but significant contribution towards the growth of red sequence (Zahid et al. 2019).

We find approximately equal number of compact and non-compact E+A galaxies in our mass-

limited sample. Both compact and non-compact E+A galaxies in our sample have a wide range of stellar mass values which cover the entire range of stellar mass values of quiescent population. Since majority ($\sim 75\%$) of non-compact E+A galaxies have high stellar mass ($> 5 \times 10^{10} M_{\odot}$) in our mass-limited sample, they do not contribute significantly to the progenitor bias effect. On the other hand, compact E+A galaxies in our sample can contribute to the population of compact galaxies at $z < 1$. There are 33% compact quiescent and 50% compact E+A galaxies in our volume-limited sample. We compute the number densities of compact quiescent and E+A galaxies in same redshift bins as in Section 4.3. Based on the trends in number density measurements of compact E+A and quiescent galaxies, we find that compact E+A galaxies contribute $48\%^{+37\%}_{-19\%}$ to number density growth of compact quiescent galaxies in our volume-limited sample.

Chapter 5

Environments of E+A galaxies at

$0.2 < z < 0.55$

Galaxy properties and their formation mechanisms are closely related with the environments in which they reside (Zehavi et al. 2005; Li et al. 2006; Blanton et al. 2005; Cassata et al. 2007). As galaxies form in dark matter haloes, probing the environment around galaxies within host dark matter halo can provide insight into their formation mechanisms (White & Rees 1978). As measurement of local environment around a galaxy probes scales internal to halo (Muldrew et al. 2012), we study the local environments around E+A galaxies in our mass-limited sample within $0.2 < z < 0.55$.

Both nearest neighbour (Section 1.3.1.1) and aperture methods (Section1.3.1.2) can be used to probe local environments. We use aperture method in combination with the smoothing kernel (B_3 spline) to estimate local densities around SHELS F2 mass-limited sample galaxies. B_3 spline is used to weight the contribution of neighbouring galaxies in estimation of local density around central

galaxy as per their distances from central galaxy. In addition to this, we also impose a velocity cut of ± 1000 km/s to include third dimension (redshift) in density estimation and remove foreground and background objects. The combination of small scale lengths (1 and 2 Mpc) with narrow velocity cut (± 1000 km/s) gives an estimate of local densities around SHELS F2 galaxies. We estimate the local densities around E+A galaxies to investigate the environments in which these galaxies reside and different mechanisms which lead to their formation in different environments.

5.1 Local stellar mass density estimation

We estimate galaxy stellar mass density (GSMD) at the locations of all galaxies in SHELS F2 field which lie above the quiescent stellar mass limit within $0.2 < z < 0.55$. The stellar mass limit increases as a function of redshift resulting in missing of more and more low mass galaxies with increasing redshift (i.e.,Malmquist bias, Section 4.1). To account for missing mass due to Malmquist bias down to $\log(M_\star/M_\odot) = 10$, we multiply the stellar masses of galaxies in our mass-limited sample with weights calculated as

$$W_z = \frac{\int_{M_l}^{M_u} M_\star \Phi\left(M_\star\right) dM_\star}{\int_{M_{\rm lim}(z)}^{M_u} M_\star \Phi\left(M_\star\right) dM_\star} \tag{5.1.1}$$

(Grogin & Geller 1998; Tempel et al. 2012). Here W_z is the weighting factor at z, $\Phi(M_\star)$ is the value of stellar mass function for a given base 10 logarithm of stellar mass $M_\star$ (in units of solar mass); M_l and M_u are base 10 logarithms of upper and lower limits of stellar mass values (in units of solar mass) and $M_{\rm lim}(z)$ is the base 10 logarithm of stellar mass limit (in units of solar mass) at redshift z.

We take $M_l = 10$ and M_u as the 95^{th} percentile of stellar mass distribution of quiescent population

within $0.2 < z < 0.55$. The stellar mass function for $0.2 < z < 0.55$ is given in the form of Schechter function (Schechter 1976):

$$\Phi(M_\star) = (\ln 10)\Phi^\star \left[10^{(M_\star - M^\star)(1+\alpha)}\right] \times \exp\left[-10^{(M_\star - M^\star)}\right]. \quad (5.1.2)$$

Here $M_\star$ is base 10 logarithm of galaxy stellar mass (in units of solar mass), $M^\star$ is base 10 logarithm of characteristic mass[1] (in units of solar mass), Φ^* is the normalization constant for stellar mass function and α is the slope of low mass end of stellar mass function. We use values of $M^\star$ and α from Muzzin et al. (2013b) to find the weighting factors at the median redshift values of each redshift bin for both star-forming and quiescent galaxies separately (Figure 5.1). At $0.2 < z < 0.55$, we take $\alpha = -1.34$ and $M^\star = 10.81$ for star-forming galaxies and $\alpha = -0.92$ and $M^\star = 11.21$ for quiescent galaxies. At $0.5 < z < 0.55$, we use values of $\alpha = -1.26$ and $M^\star = 10.78$ for star-forming galaxies and $\alpha = -0.44$ and $M^\star = 10.87$ for quiescent galaxies.

Muzzin et al. (2013b) stellar mass functions are based on 1.6 deg^2 COSMOS/UltraVISTA field catalog (Muzzin et al. 2013a). Because of small area covered by COSMOS/UltraVISTA field, stellar mass functions may not be well constrained at $z < 1$. Ilbert et al. (2013) also computes stellar mass functions for star-forming and quiescent galaxies based on a different catalog from COSMOS/UltraVISTA field. The comparison of results from Muzzin et al. (2013b) and Ilbert et al. (2013) shows that stellar mass functions from Ilbert et al. (2013) have shallower α for quiescent galaxies and steeper α for star-forming galaxies as compared to α values from Muzzin et al. (2013b) (see Appendix C of Muzzin et al. (2013b) for more details). These differences might arise due to

[1]characteristic mass is the mass at the knee of stellar mass function at which the mass function changes rapidly.

different definition of quiescent galaxies and higher number densities for star-forming galaxies in Ilbert et al. (2013) as compared to Muzzin et al. (2013b). Overall, the stellar mass functions from both studies are more similar than different.

Furthermore, Ilbert et al. (2013) stellar mass functions are consistent with stellar mass functions from Moutard et al. (2016), which is based on a catalog from VIPERS spectroscopic survey covering a wide area of 22.4 $\deg^2$ (see Moutard et al. (2016) for details). We can indirectly compare the stellar mass functions from Muzzin et al. (2013b) with stellar mass functions from Moutard et al. (2016) based on the information of comparison of results from Ilbert et al. (2013) with both these studies. Hence, we can say that the stellar mass functions given in Muzzin et al. (2013b) may not be as well constrained as stellar mass functions from Moutard et al. (2016) but they are still more similar than different. Furthermore, we can reduce the dependence of our GSMD values on the stellar mass functions (used to estimate weights) by computing GSMD ratios which we explain at the end of this section. To obtain the weighting factors as a function of redshift (W_z), we use linear interpolation and correct the stellar mass value of each galaxy as

$$M_\star^{\rm tot} = M_\star \times W_z. \tag{5.1.3}$$

Star-forming galaxies have higher weights than quiescent galaxies because of the difference in shapes of stellar mass functions within $9.5 < \log(M_\star[M_\odot]) < 11$ for two galaxy populations. The number density of star-forming galaxies is higher than quiescent galaxies within $0.2 < z < 0.5$ for stellar mass range $9.5 < \log(M_\star[M_\odot]) < 11$ - as shown in Figure 8 of Muzzin et al. (2013b). As we are correcting down to $\log(M_\star[M_\odot]) = 10$, missing low mass galaxies in our analysis are more

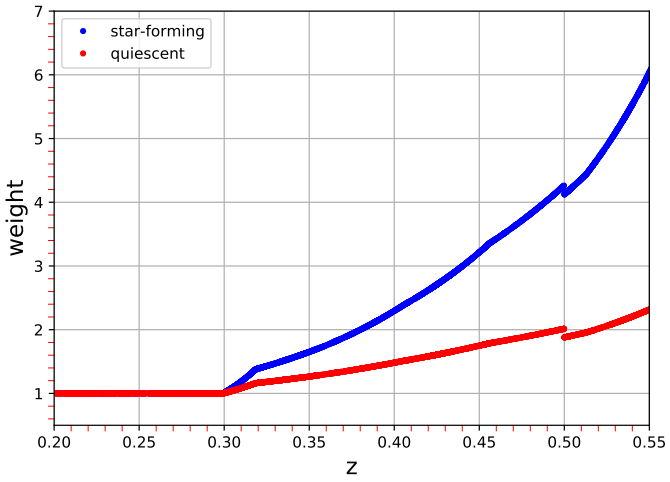

Figure 5.1: Weighting factors for star-forming and quiescent galaxies as a function of redshift shown in blue and red respectively.

likely to be star-forming galaxies and hence the weighting factors are higher for star-forming than quiescent galaxies.

To probe the local environment of galaxies in our sample, we weight all galaxies (Equation 5.1.3) within ± 1000 km/s from the central galaxy by their distances (in Mpc) from the central galaxy using B_3 spline kernel (Tempel et al. 2012):

$$B_3(x) = \frac{|x-2|^3-4|x-1|^3+6|x|^3-4|x+1|^3+|x+2|^3}{12}, \tag{5.1.4}$$

where x corresponds to the distance (in Mpc) between galaxies. Galaxies that are far away from the central galaxy get lower weights than galaxies near to the central location (left panel of Figure 5.2). This weighting procedure allows us to construct smooth density field.

We probe four smoothing scales, from 1 to 4 Mpc, to see how local environment changes at

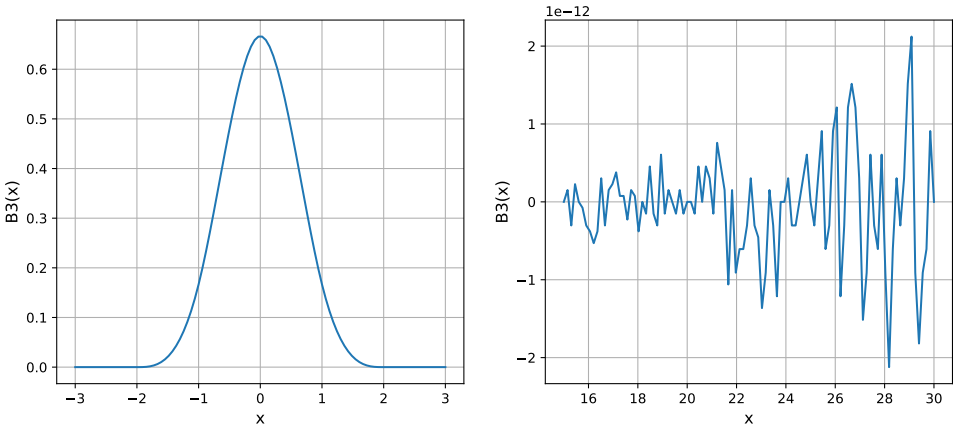

Figure 5.2: Left: The form of spline kernel $B_3(x)$ as a function of uniform distribution of x. Spline kernel gives non-zero weights only to the values which lie within |x| > 2. Right: Spline kernel gives extremely small negative values for large values of x which are just numerical errors.

different scales. We do not place the center of the cell at the position of the central galaxy because doing that would give the maximum weight to the central galaxy in density estimation (B_3 spline function peaks at $x = 0$, left panel of Figure 5.2). Giving the maximum weight to the central galaxy overestimates or underestimates the measurement of local environment around it depending on the mass of the galaxy. To avoid assigning the highest weights always to the central object, we displace the center of the cell by a random value. This random value is smaller than the smoothing scale so that it does not affect our definition of local environment. We calculate local GSMD at these new locations as

$$m = \frac{1}{a^3} \sum_{i=0}^{N} B_3 \left(\frac{|\boldsymbol{r} - \boldsymbol{r}_i|}{a} \right) M_{\star i}^{\rm tot} \,. \tag{5.1.5}$$

Here $|r - r_i|$ is the distance between the given location $r \equiv [\alpha, \delta, r(z)]$ and i^{th} galaxy in arcseconds. We change the distance from arcseconds to Mpc using `Planck13` cosmology model (Planck Collab-

oration et al. 2014) from `astropy`[2] and normalize it by smoothing scale a(Mpc). The spline kernel used to smooth the region around each galaxy is $B_3(\frac{|r-r_i|}{a})$ such that $B_3(\frac{|r-r_i|}{a}) = 0$ for $|r - r_i| > 2a$ (left panel of Figure 5.2).

Spline kernel sometimes gives negligibly small negative values ($\sim 10^{-12}$) for very large values of x (right panel of Figure 4.5). These negative values are extremely small numerical errors and make no difference to our GSMD values. We decide to take into account the positive values of spline function in GSMD estimation.

We compute GSMD field around all galaxies to make a comparison between the local densities around E+A galaxies and local densities around star-forming and quiescent galaxies. We can not directly compare density values of two galaxies at different redshifts because density distribution changes with redshift. It is better to use relative values normalized by a suitable parameter rather than absolute values. We compute local GSMD ratios around galaxies by dividing local GSMD values with average GSMD values. Average GSMD value for each central galaxy represents the average of GSMD distribution of all galaxies within the radial velocity interval of ± 1000 km/s from the redshift of the central galaxy. Stellar mass function dependent weights (Equation 5.1.1) have similar effect on the GSMD values in the numerator and denominator of the GSMD ratio. Thus, GSMD ratios reduce the dependence of our results on the type of stellar mass function used to estimate weights.

[2]Astropy is a collection of software packages written in programming language `Python` and is used to perform computations in astronomy. This package is available at https://docs.astropy.org/en/stable/cosmology/index.html

5.2 Accounting for the edge effects

Our procedure does not give accurate density values at the locations of galaxies (α, δ, z) which lie at the edges of the survey because we have no information about the number of galaxies present on the other side of the edge of survey. We take the edges of the field in equatorial coordinates (Geller et al. 2014) and exclude all galaxies that are within one smoothing length (a) from the field edge (following the approach from (Tempel et al. 2012)). In order to do this, we convert smoothing length (a) given in physical units (Mpc) into arcseconds on the sky using `Planck13` cosmology model (Planck Collaboration et al. 2014) from `astropy` (Section 5.1). Once the scale length is converted into arcseconds on the sky, we change the survey field as

$$\alpha_{min,z} = \alpha_{min,0} + \frac{a(z)}{\sqrt{2}}, \tag{5.2.1}$$

$$\alpha_{max,z} = \alpha_{max,0} - \frac{a(z)}{\sqrt{2}}, \tag{5.2.2}$$

$$\delta_{min,z} = \delta_{min,0} + \frac{a(z)}{\sqrt{2}}, \tag{5.2.3}$$

$$\delta_{max,z} = \delta_{max,0} - \frac{a(z)}{\sqrt{2}}, \tag{5.2.4}$$

where $(\alpha_{min,0}, \delta_{min,0})$, $(\alpha_{max,0}, \delta_{max,0})$, $(\alpha_{min,0}, \delta_{max,0})$ and $(\alpha_{max,0}, \delta_{min,0})$ are the original edge coordinates of the field and $(\alpha_{min,z}, \delta_{min,z})$, $(\alpha_{max,z}, \delta_{max,z})$, $(\alpha_{min,z}, \delta_{max,z})$ and $(\alpha_{max,z}, \delta_{min,z})$

are new edge coordinates of the field at z. The smoothing scale at redshift z is $a(z)$ in units of arcseconds.

Using above equations, we can define new edges of the survey field that change with redshift and check how many galaxies fall outside of these edges. The ones that are out are not considered as centres of the cells for local GSMD measurements. The number of edge galaxies decrease with increasing redshift at a fixed smoothing scale because a fixed length in Mpc corresponds to smaller values in arcseconds at higher redshift as discussed above. Figure 5.3 shows the distribution of SHELS F2 field galaxies in α cosδ_0[3] and δ plane for four different smoothing scales (1 to 4 Mpc). Edge galaxies are shown as blue points and the number of edge galaxies are written in title of each panel. As expected, number of edge galaxies increase with increasing smoothing length. There are 17 E+A galaxies in our mass-limited sample which reduce to 16 galaxies at 3 Mpc and 14 galaxies at 4 Mpc because of the edge effects.

5.3 Assigning cluster membership

Another way to measure the environments of galaxies is Friends of Friends (FoF) algorithm (Huchra & Geller 1982). We compare our GSMD measurements for SHELS F2 galaxies with the results from FoF algorithm to verify our GSMD measurements in Section 5.4.1. We start by briefly describing FoF algorithm here.

FoF algorithm starts a chain by finding neighbouring galaxies which lie within a given linking length from the central galaxy. The chain continues by finding neighbours of neighbouring galaxies

[3]As we are probing the part of celestial sphere which is far away from equator, to correct for projection effect, we multiply α with the center of δ values in the field which is 30 degrees.

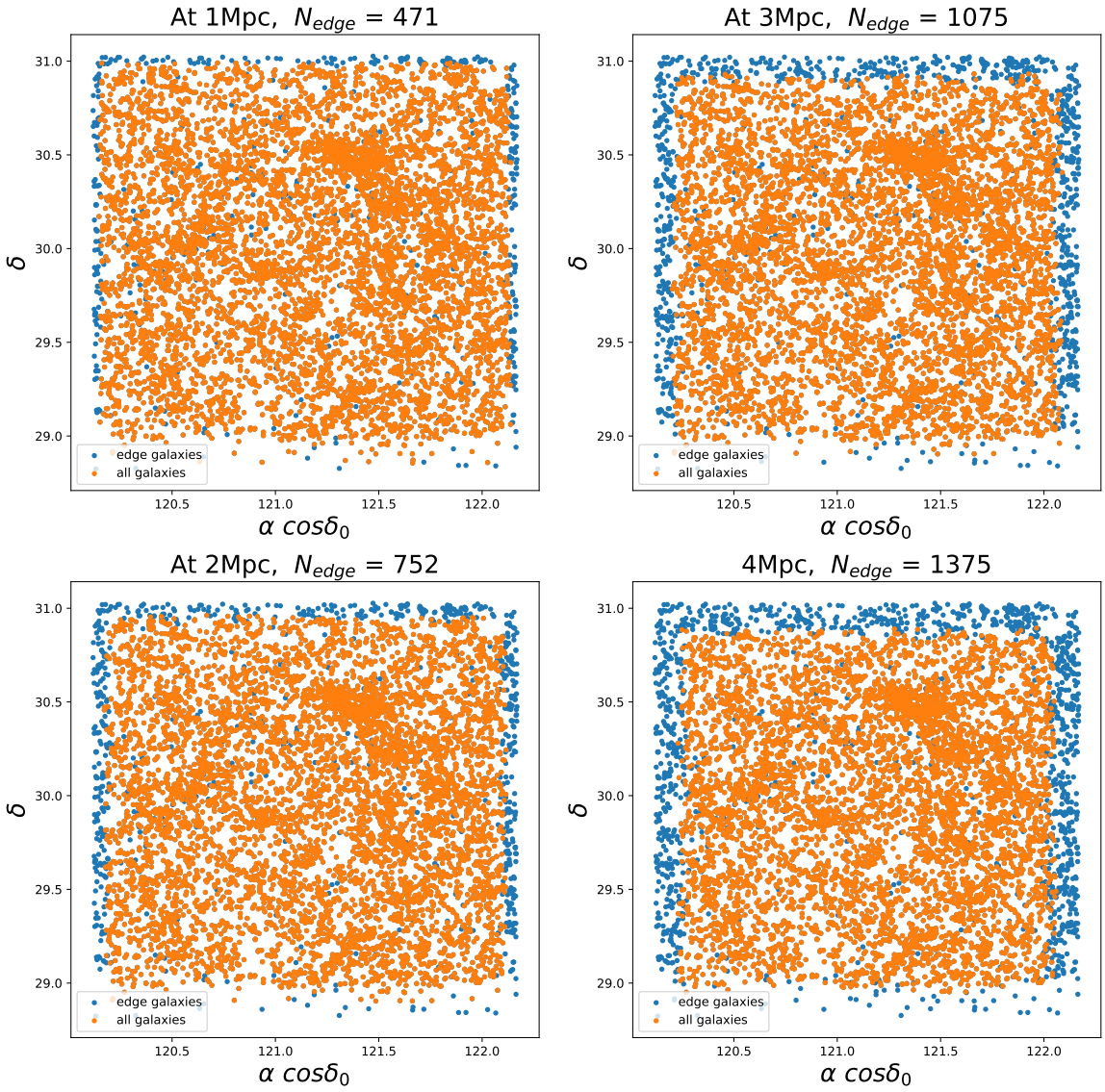

Figure 5.3: Distribution of SHELS F2 mass-limited sample galaxies (orange points) in $\alpha\cos\delta_0$ and δ plane for four different smoothing scales (1 to 4 Mpc). We show the number of edge galaxies as blue points and also write the number of edge galaxies as N_{edge} in the title for each panel. The number of edge galaxies increase as a function of increasing length of smoothing scale.

within the same linking length and so on (Huchra & Geller 1982; Berlind et al. 2006; Tempel et al. 2012; Hwang et al. 2016; Sohn et al. 2016, 2018). FoF algorithm uses two linking lengths known as projected linking length ($b_{projected}$) and radial linking length (b_{radial}). These linking lengths are related to projected spatial direction (ΔD), projected radial direction (ΔR) and mean galaxy volume number density ($n_{g,mean}$) in a survey at a given redshift z as

$$\Delta D = b_{projected} \times n_{g,mean}^{-1/3}(z) \tag{5.3.1}$$

$$\Delta R = b_{radial} \times n_{g,mean}^{-1/3}(z) \tag{5.3.2}$$

(Sohn et al. 2021). It is very important to find an optimal linking length. If linking length is very small then algorithm selects compact dense systems and is prone to missing large size galaxy systems. On the other hand, if linking length is very large then it finds comparatively smaller number of systems as it selects galaxies spread over large distances as one system.

Minimum galaxy overdensity is related to projected linking length (Huchra & Geller 1982) as

$$\frac{\delta n}{n} = \frac{3}{4\pi (b_{projected})^3} - 1, \tag{5.3.3}$$

where $\frac{\delta n}{n} > 1$ represents galaxy overdensity and $\frac{\delta n}{n} < 1$ represents underdense systems. As galaxy volume number density changes with redshift, a constant linking length probes systems of varying densities at different redshift. We need to change the linking length with redshift if we want to probe systems of same densities at different redshift. Hence, the choice of optimal linking length depends

strongly on the density and the redshift of the galaxy system that we aim to find with FoF algorithm.

Sohn et al. (2018) computes the environments of SHELS F2 galaxies with FoF algorithm using $b_{projected} = 0.1$ and $b_{radial} = 0.5$. The information about SHELS F2 cluster members is available in the form of a table based on FoF algorithm. We match all galaxies in our E+A sample with the objects in cluster table from Sohn et al. (2018) on the basis of three parameters: α, δ and z using `Skycoord`[4].

We decide to use the redshift range $0.2 < z < 0.55$ for our analysis as it traces the clusters in SHELS F2 field. These clusters have the highest overdensities at $z = 0.3$. There are 26 E+A galaxies within $0.2 < z < 0.55$ and 17/26 lie in our mass-limited sample. Based on matching results we find that there are 3713 cluster members in SHELS F2 field within $0.2 < z < 0.55$ and five of these are E+A galaxies. Our SHELS F2 mass-limited sample consists of 2344 cluster FoF members within $0.2 < z < 0.55$ and two of these are E+A galaxies.

5.4 Environments of SHELS F2 galaxies within $0.2 < z < 0.55$

5.4.1 GSMD measurements for the mass-limited sample

We estimate the GSMD values at the locations of all galaxies in SHELS F2 field above quiescent stellar mass limit (Section 4.1) within $0.2 < z < 0.55$ for four smoothing scales from 1 to 4 Mpc. It is well established that star-forming galaxies ($D_n4000 < 1.5$) lie in lower density regions than quiescent ($D_n4000 > 1.5$) galaxies (Kennicutt 1983; Hashimoto et al. 1998; Balogh et al. 2001;

[4]Skycoord is a subpackage in `astropy` used to represent, manipulate and tranform celestial coordinates in different coordinate systems. Detailed information for this subpackage is available at https://docs.astropy.org/en/stable/api/astropy.coordinates.SkyCoord.html.

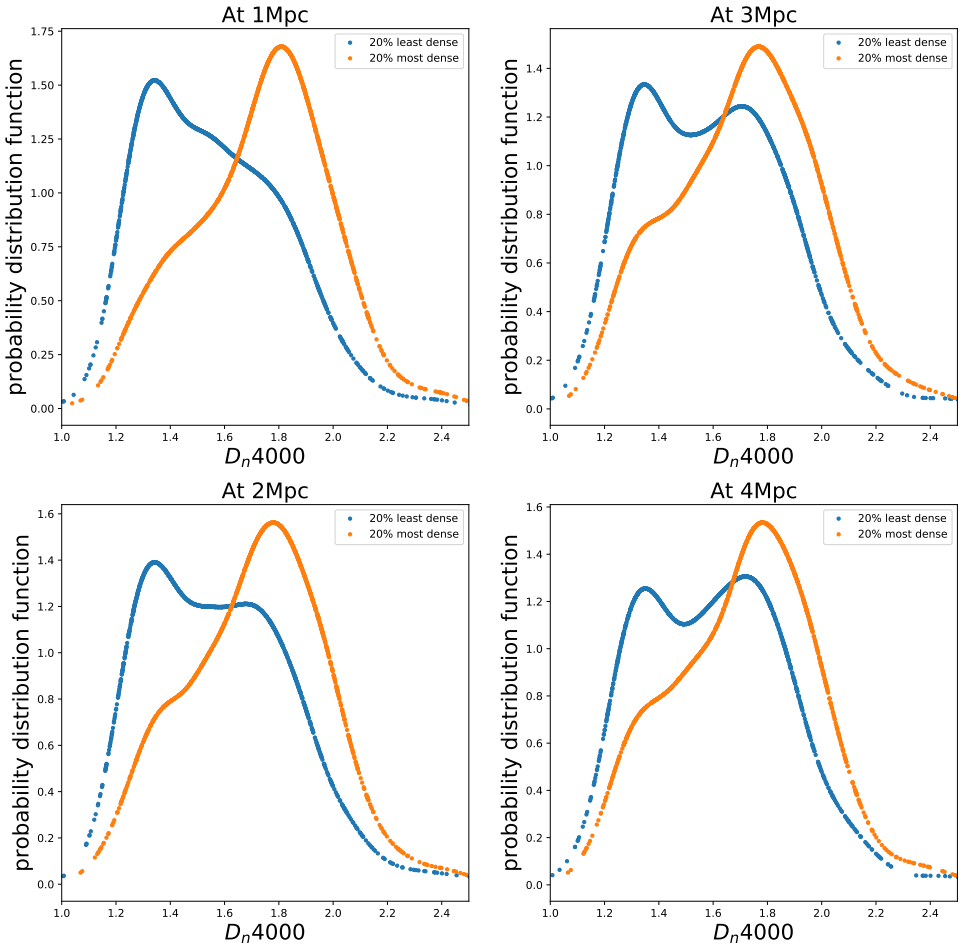

Figure 5.4: Distribution of D_n4000 values of SHELS F2 mass-limited sample galaxies which lie in 20% most dense (orange curve) and 20% least dense (blue curve) regions for four smoothing scales from 1 to 4 Mpc.

Hogg et al. 2003; Kauffmann et al. 2004; Quintero et al. 2005; Muldrew et al. 2012). To verify our GSMD measurements, we select galaxies which lie within 20% least dense and 20% most dense regions based on our GSMD ratio measurements and compare their D_n4000 distributions in Figure 5.4. We find that 20% least dense distribution has two peaks. Lower D_n4000 galaxies dominate the highest peak in 20% least dense distribution but second peak become more prominent with increasing scale length as higher D_n4000 galaxies start to join 20% least dense galaxy population. There are two peaks in 20% most dense distribution but the peak at lower D_n4000 values is not that prominent. Higher D_n4000 galaxies significantly dominate 20% most dense population. Our results are consistent with Figure 7 of Muldrew et al. (2012) which confirms that our density measurements are robust.

To further verify our density measurements, we make a comparison between GSMD and GSMD ratio distributions of star forming, quiescent, and FoF cluster members in Figures 5.5 and 5.6. We find that the star-forming and quiescent galaxies have lower density distribution than cluster population, as expected.

To compare the distributions for star-forming and quiescent galaxies, where the difference is not obvious from Figures 5.5 and 5.6, we perform Kolmogorov-Smirnov (K-S) test (Fasano & Franceschini 1987). The null hypothesis that is tested by K-S test is that two distributions belong to the same underlying distribution. K-S test statistics measure the probability for null hypothesis to be true. The probability to obtain K-S statistics above the value given by the two tested distributions is p. If $p-$ value is below a chosen level of significance α, the null hypothesis is rejected. Otherwise the hypothesis cannot be rejected.

We assume the null hypothesis that star-forming galaxies and quiescent galaxies belong to the

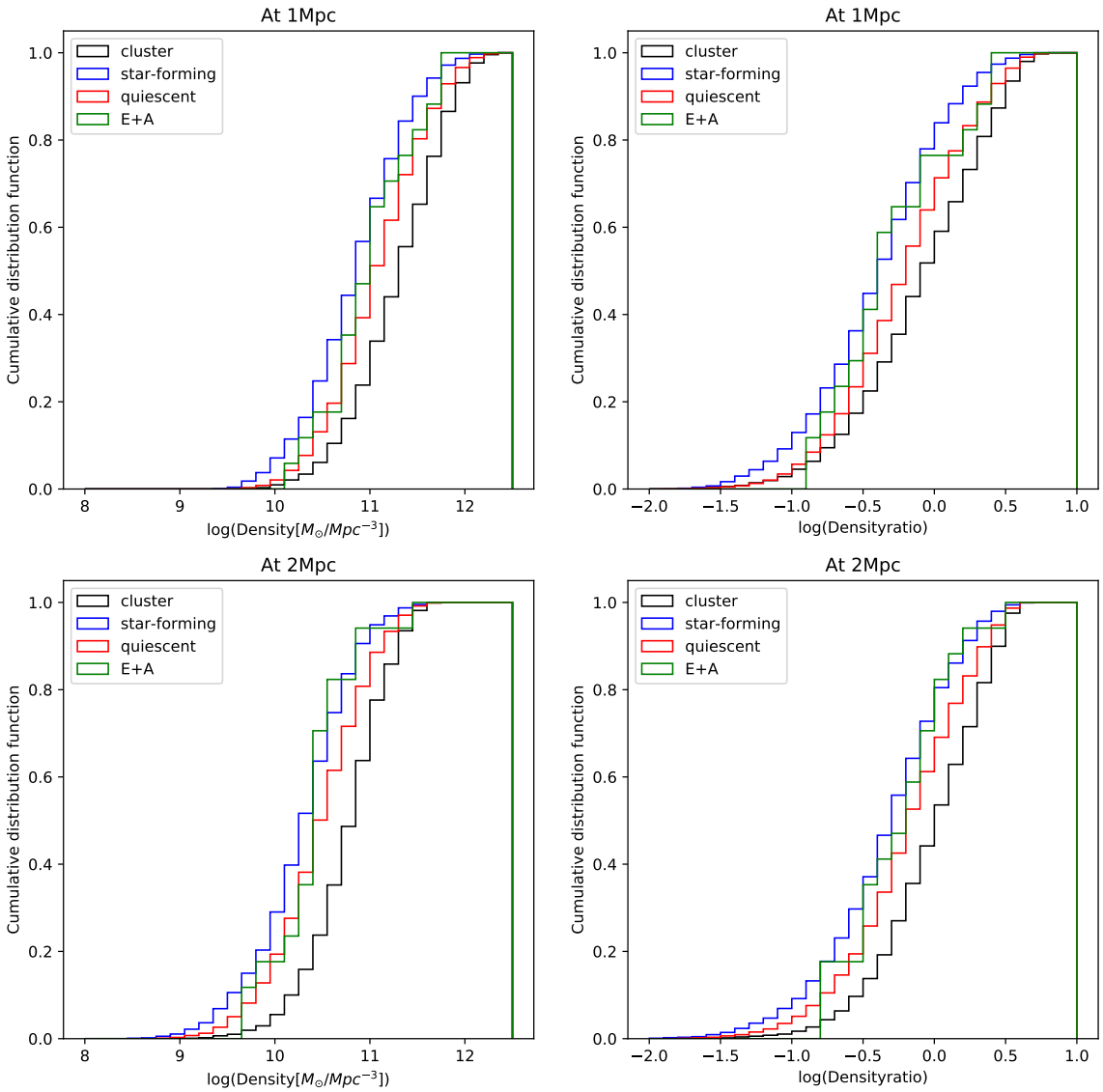

Figure 5.5: Left: GSMD distribution of star-forming (blue), quiescent (red), post-starburst (green) and cluster galaxies (black) from mass-limited SHELS F2 sample for smoothing scales of 1 and 2 Mpc. Right: GSMD ratio distribution of all galaxies from left panel for smoothing scales of 1 and 2 Mpc with the same color scheme as left panels.

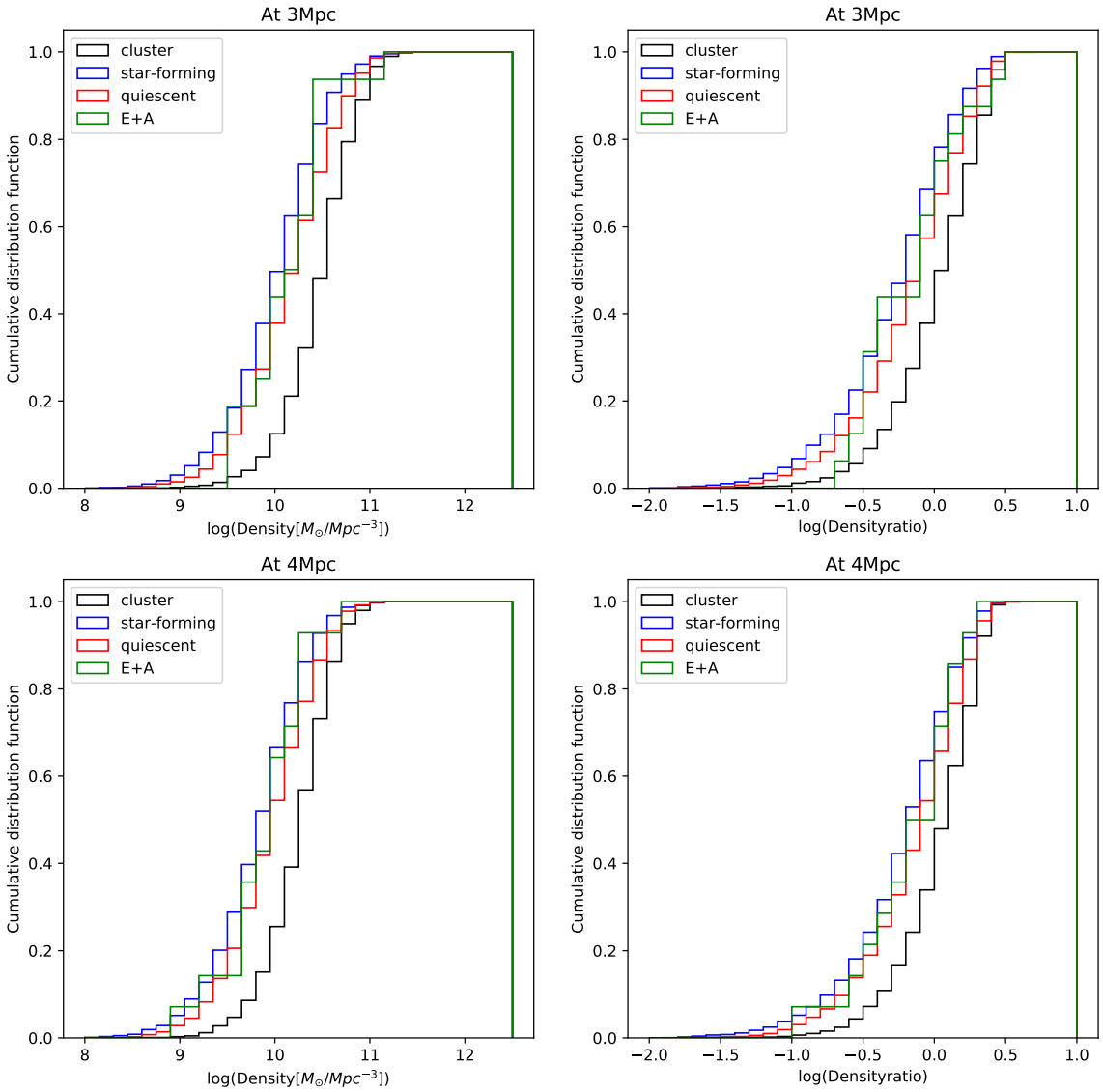

Figure 5.6: Continuation of Figure 5.5.

same underlying distribution and choose a significance level of 0.05. Our K-S test results show that $p-$values range from 10^{-44} to 10^{-15} from 1Mpc to 4Mpc. These $p-$values are significantly smaller than 0.05 for all scales and hence we can reject null hypothesis at all scale lengths. K-S test verifies our GSMD measurements that star-forming and quiescent galaxies follow different GSMD distributions. We also perform K-S tests to compare GSMD distribution of E+A galaxies with GSMD distributions of star-forming and quiescent galaxies. From K-S test results, we cannot reject the null hypothesis that E+A galaxies reside in similar density environments as star-forming and quiescent galaxies at any scale length.

Left panels of Figures 5.7 and 5.8 show the distribution of GSMD measurements around galaxies in our mass-limited sample within $0.2 < z < 0.55$ for all scale lengths in different redshift bins. Right panels show the distribution of mass-limited FoF cluster members (Section 5.3) with the same stellar mass limit as our mass-limited SHELS F2 sample. We find that the locations of highest GSMD regions from left panels trace the locations of FoF cluster members from right panels. Some disagreement shows up in higher redshift bins because we cannot trace GSMD field with as many galaxies as in the lower redshift bins. GSMD field is sparse at high redshift because we can only trace highest mass objects.

Large symbols in left and right panels of Figures 5.7 and 5.8 represent 26 galaxies in our E+A sample within $0.2 < z < 0.55$, including E+A galaxies which lie below stellar mass limit. We find that GSMD values around cluster E+A galaxies are indeed high and GSMD values around non-cluster E+A galaxies are low in both panels which again shows the agreement between our GSMD measurements and matching results from FOF algorithm. This agreement also holds for the comparison of GSMD ratios with the results from FOF algorithm (Figures 5.9 and 5.10).

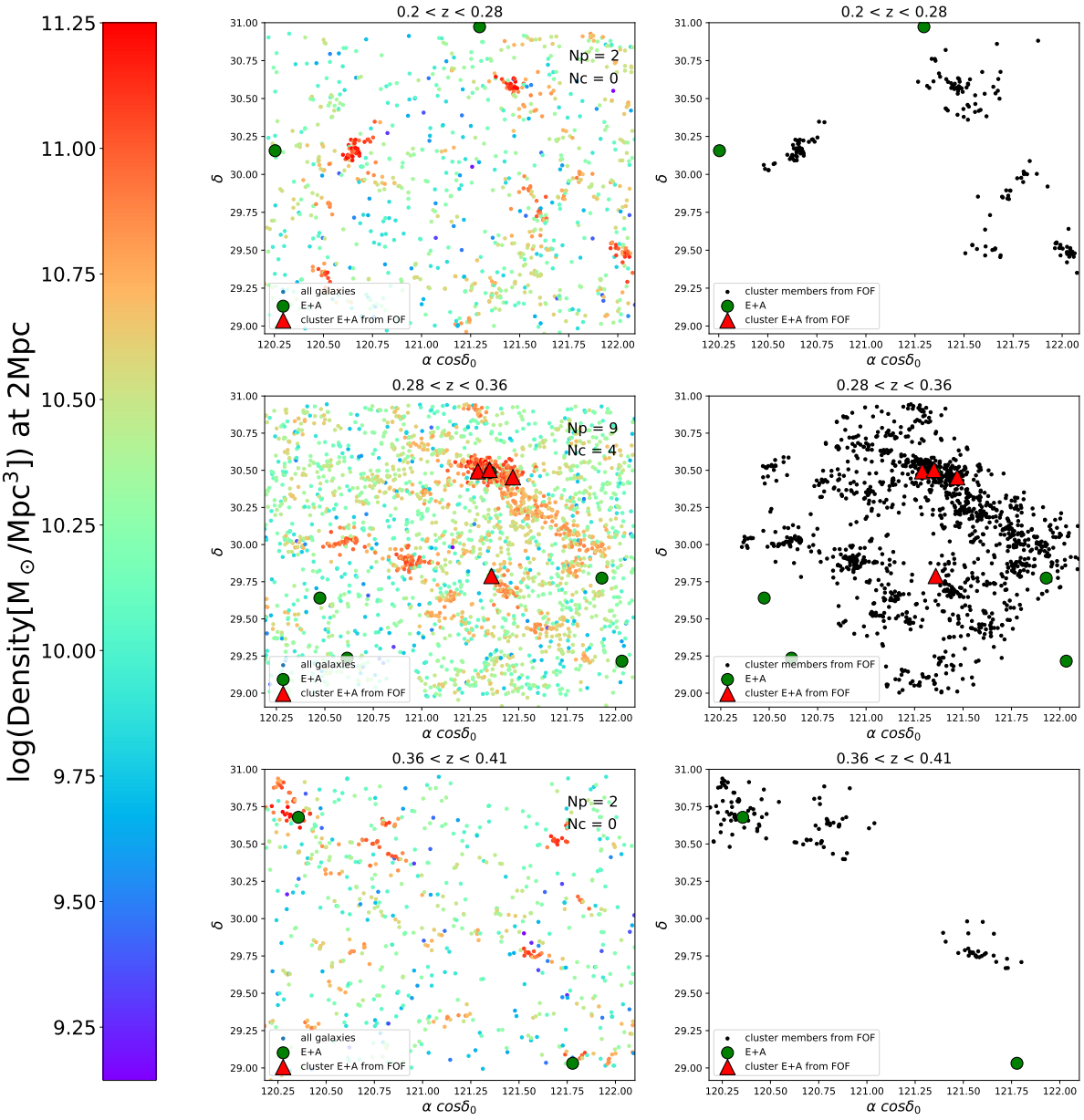

Figure 5.7: Left: Distribution of local GSMD values around galaxies in mass limited SHELS F2 sample on $\alpha\cos\delta_0$ and δ plane in different redshift bins, where δ_0 = 30 degrees. GSMD values are colour coded on a logarithmic scale with the redder colours representing the highest densities. Green points represent E+A galaxies and red triangles represent E+A galaxies in clusters from our sample. The symbols N_p and N_c denote the number of E+A galaxies and number of FoF cluster E+A galaxies in each redshift bin. Right: Distribution of FoF clusters on $\alpha\cos\delta_0$ and δ plane. Black points represent the FoF cluster members in SHELS F2 field. Large symbols follow the same colour scheme as in left panels.

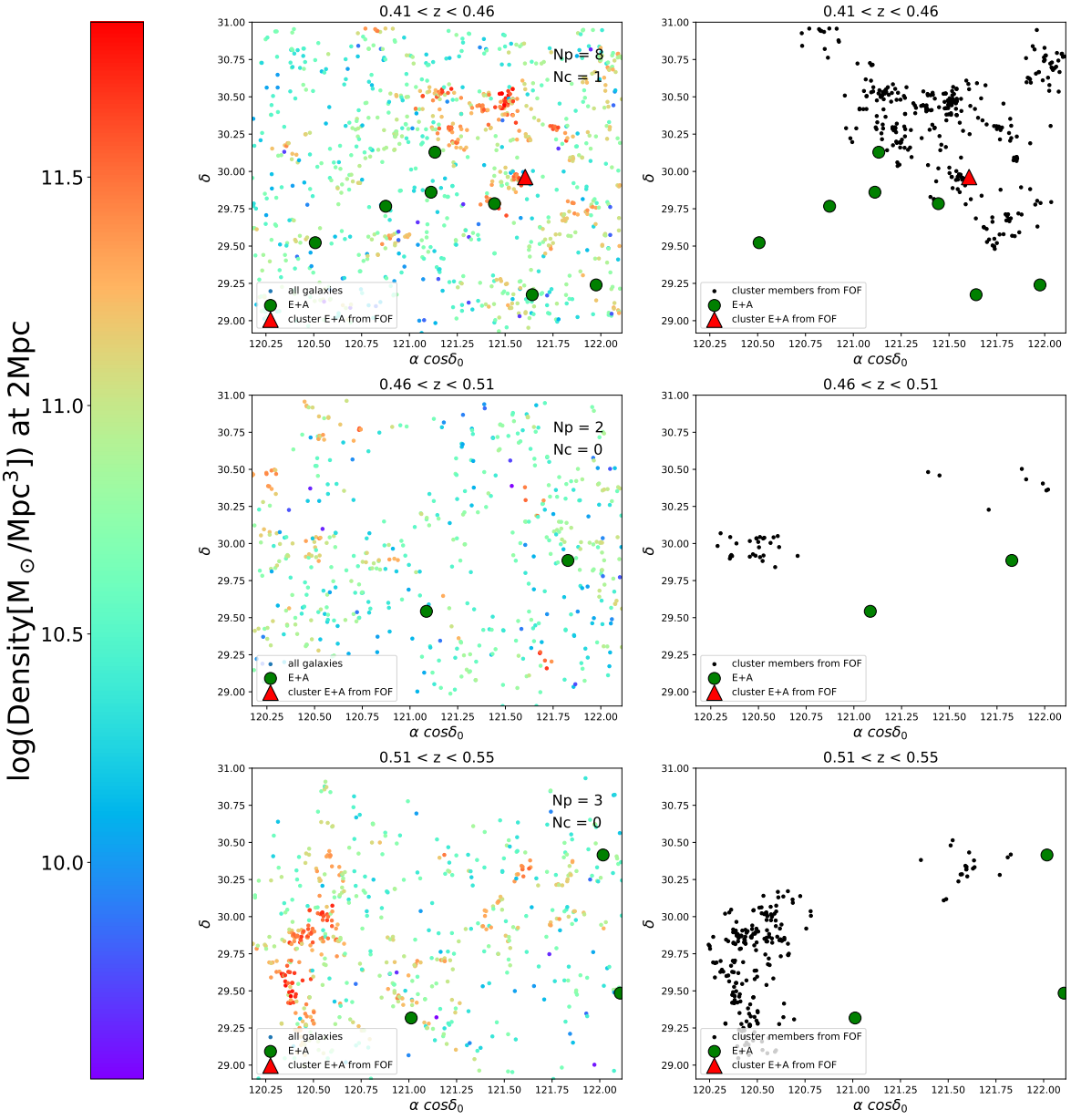

Figure 5.8: Continuation of Figure 5.7.

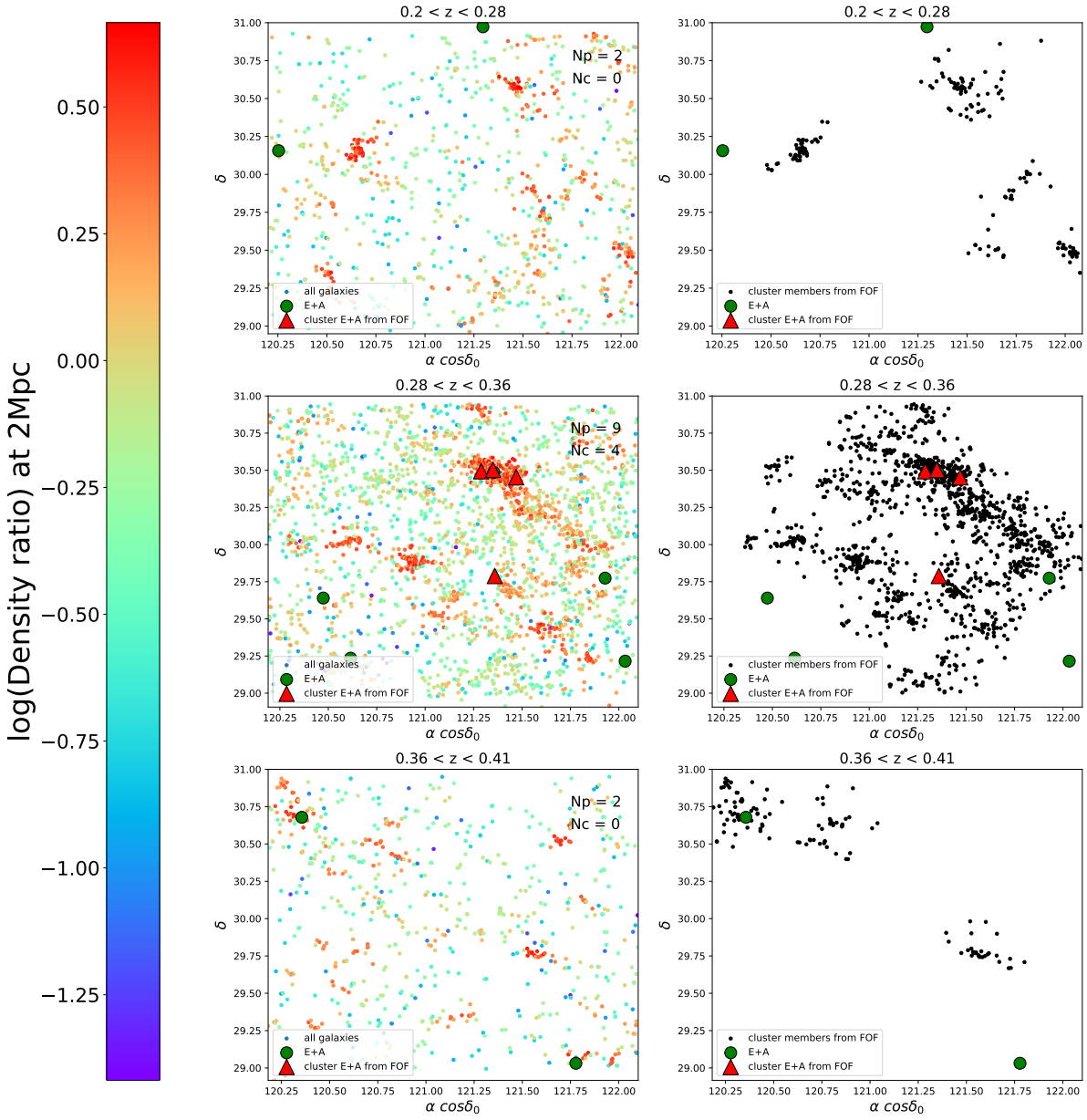

Figure 5.9: Left:Distribution of local density ratios around galaxies in mass limited SHELS F2 sample on $\alpha\cos\delta_0$ and δ plane in different redshift bins, where δ_0 = 30 degrees. The density ratio values are colour coded on a logarithmic scale with the redder colours representing the highest densities. Green points represent E+A galaxies and red triangles represent E+A galaxies in clusters from our sample. The symbols N_p and N_c denote the number of E+A galaxies and number of cluster E+A galaxies in each redshift bin. Right: Distribution of FOF clusters on $\alpha\cos\delta_0$ and δ plane. Black points represent the cluster members in SHELS F2 field. Large symbols follow the same colour scheme as in left panels.

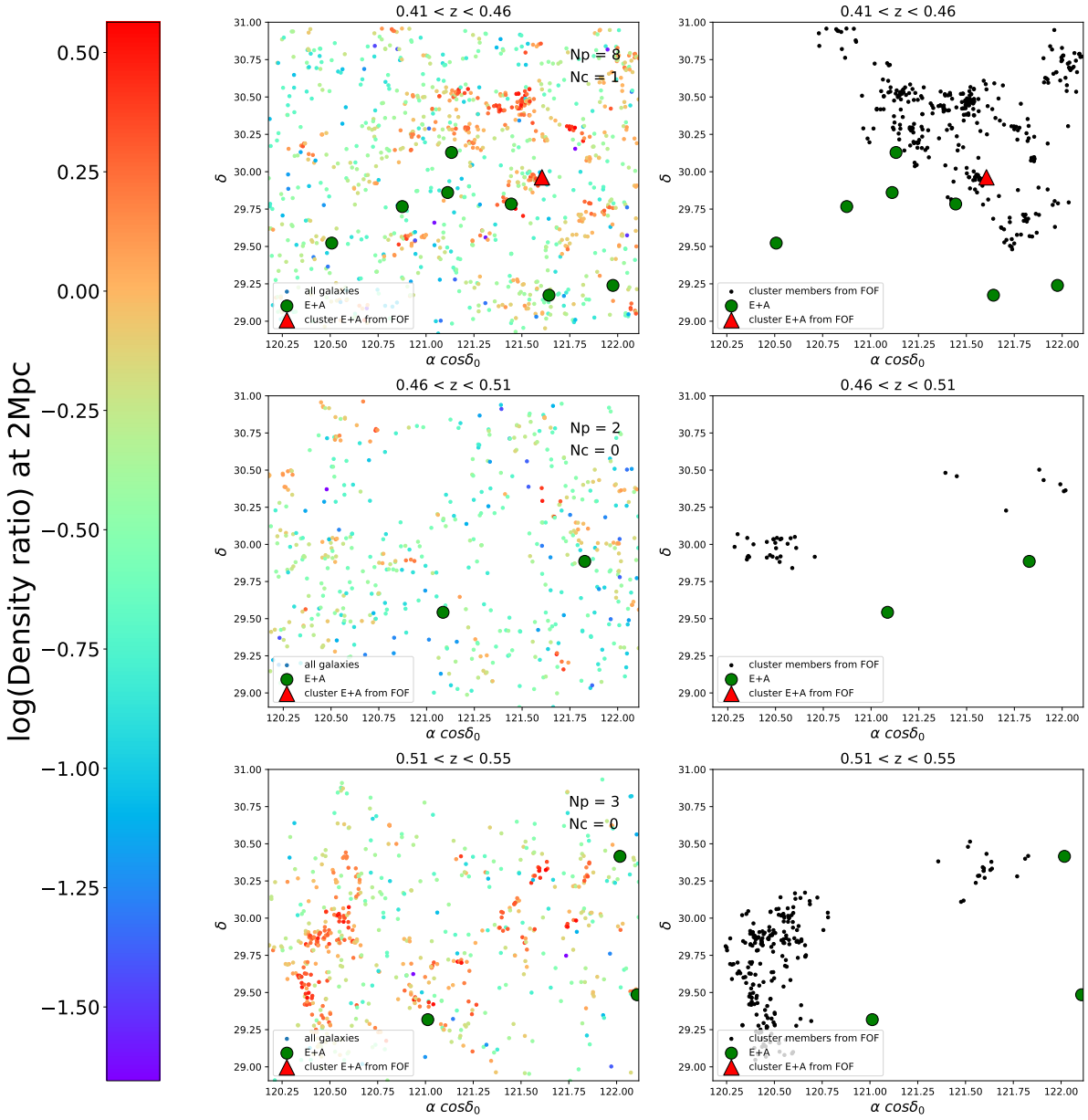

Figure 5.10: Continuation of Figure 5.9.

Table 5.1: Fraction of mass-limited E+A galaxies in different GSMD ratio bins: 0 to 33, 34 to 67 and 68 to 100 percentiles of GSMD ratio distribution of all galaxies with upper and lower errors. GSMD ratio values in the first, second and third bin correspond to underdense, average and overdense regions respectively.

Scale (Mpc)	$0-33$	$34-67$	$68-100$
1	$35.3\%^{+24\%}_{-16\%}$	$41.2\%^{+26\%}_{-18\%}$	$23.5\%^{+20\%}_{-13\%}$
2	$35.29\%^{+24\%}_{-16\%}$	$35.29\%^{+24\%}_{-16\%}$	$29.41\%^{+22\%}_{-15\%}$
3	$43.75\%^{+28\%}_{-20\%}$	$31.25\%^{+24\%}_{-16\%}$	$25.0\%^{+22\%}_{-15\%}$
4	$35.71\%^{+28\%}_{-19\%}$	$14.28\%^{+20\%}_{-10\%}$	$50\%^{+33\%}_{-23\%}$

Table 5.1 shows the GSMD ratio distribution of mass-limited E+A galaxies in different GSMD ratio bins: underdense, average and overdense regions for all scale lengths with upper and lower errors on each value. E+A galaxies have similar percentage in underdense, average dense and overdense regions within large error bars, hence E+A galaxies prefer no special environments. Also, the percentage of all SHELS F2 galaxies in overdense regions is $33\% \pm 10^{-4}$, similar to the percentage of E+A galaxies in overdense regions within error bars. The fact that the fraction of E+A galaxies in overdense regions agrees with the fraction of all galaxies residing in these regions suggests that E+A galaxies follow general galaxy population.

5.4.2 GSMD measurements for the volume-limited sample

To test the results based on GSMD measurements for the mass-limited sample using galaxies for which corrections due to missing mass are not required, we estimate GSMD field around galaxies in volume-limited sample (Section 4.2) using the same procedure from Section 5.1. We construct volume-limited sample in such a way that all galaxies in the sample are high mass galaxies ($\log(M_\star) > 10.8$)

which are observable through the redshift range $0.01 < z < 0.6$. There is no need to correct for Malmquist bias in GSMD estimation for these high mass galaxies.

Volume-limited sample consists of 8 E+A galaxies within $0.2 < z < 0.55$ and one out of these 8 E+A galaxies is a cluster member. There are 579 star-forming galaxies and 2924 quiescent galaxies in volume-limited sample including 1023 cluster members. The fraction of cluster E+A galaxies in volume-limited E+A sample is 1/8 i.e. $12.5\%^{+29.4\%}_{-11.2}$, similar to fraction of cluster galaxies in mass-limited E+A sample (2/17 i.e. $11.8\%^{+16\%}_{-8}$).

Left panels of Figures 5.11 and 5.12 show the distribution of GSMD measurements around galaxies from volume-limited sample within $0.2 < z < 0.55$ for all scale lengths in different redshift bins. Right panels show the distribution of FoF cluster members (Section 5.3) which have $\log(M_\star) > 10.8$ (similar to galaxies in volume-limited sample) in different redshift bins. Large symbols in each panel show E+A galaxies in volume-limited sample. The locations of highest GSMD regions from left panels trace the locations of FoF cluster members from right panels which verifies that our GSMD measurements are in agreement with the results from FOF algorithm. Cluster E+A galaxies show up in high GSMD regions in both panels and non-cluster E+A galaxies are indeed in lower GSMD regions.

Based on comparison of Figures 5.7 and 5.8 with Figures 5.11 and 5.12, we confirm that GSMD measurements from mass-limited sample are consistent with GSMD measurements from volume-limited sample. This consistency also holds for GSMD ratios based on comparison of Figures 5.9 and 5.10 with Figures 5.13 and 5.14. The consistency between the results from two samples shows that our results from mass-limited sample are robust to the correction for missing stellar mass.

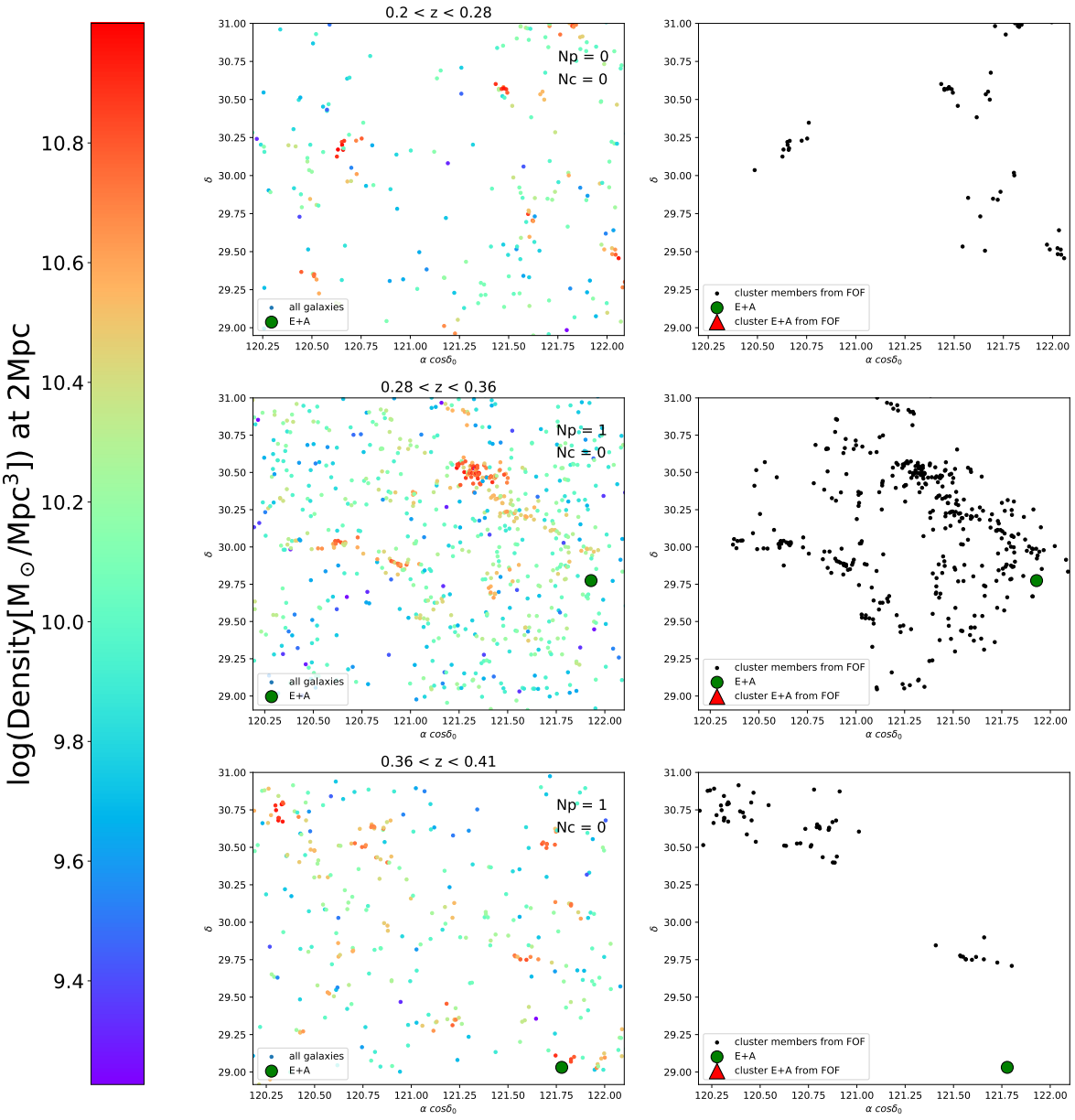

Figure 5.11: Left: Distribution of GSMD values around galaxies in volume-limited SHELS F2 sample on α cosδ_0 and δ plane in different redshift bins, where δ_0 = 30 degrees. The density values are colour coded on a logarithmic scale with the redder colours representing the highest densities. Green points represent E+A galaxies and red triangles represent E+A galaxies in clusters from our sample. The symbols N_p and N_c denote the number of E+A galaxies and number of cluster E+A galaxies in each redshift bin. Right: Distribution of FoF clusters on α cosδ_0 and δ plane. Black points represent the cluster members in SHELS F2 field. Large symbols follow the same colour scheme as in left panels.

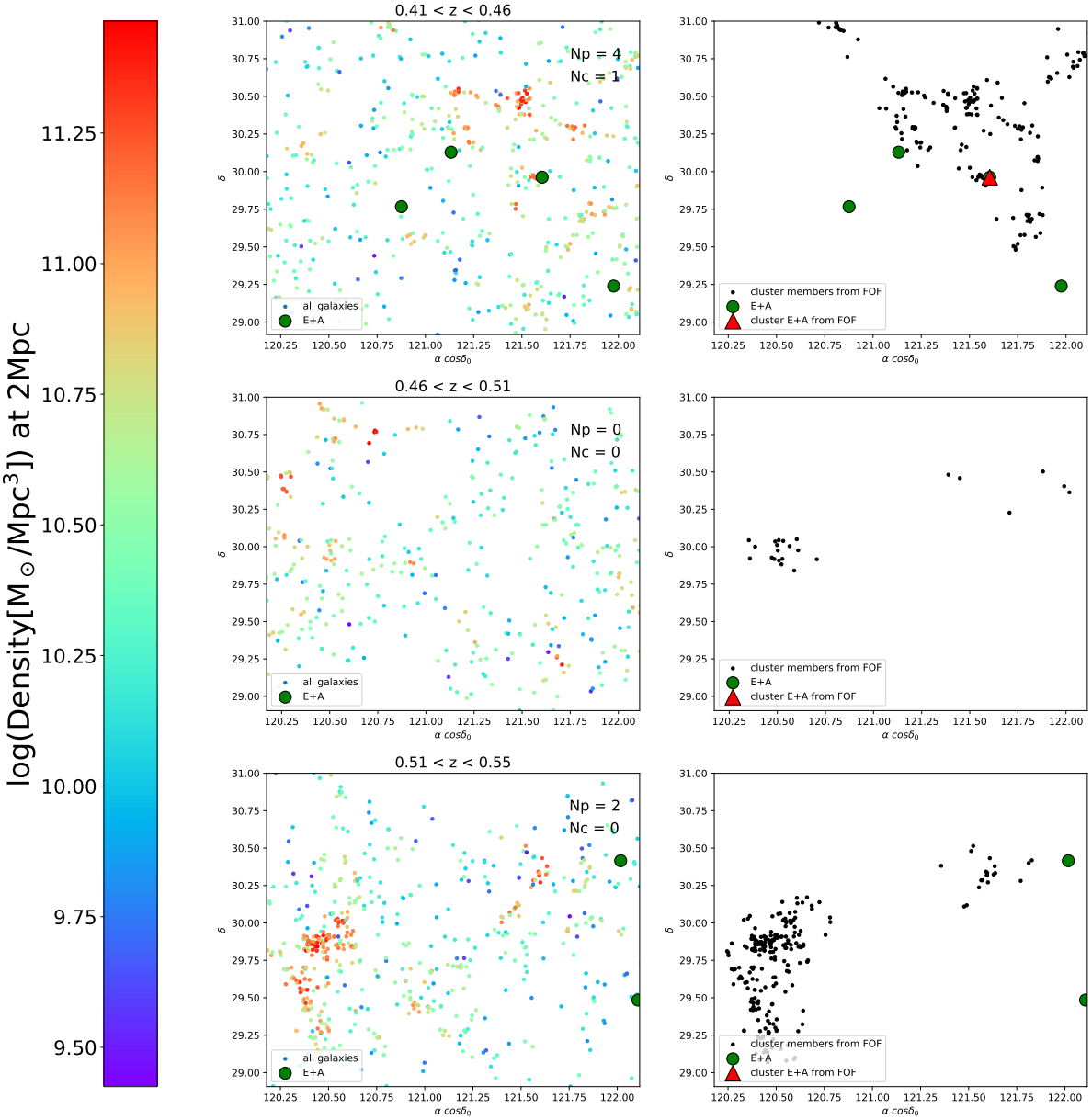

Figure 5.12: Continuation of Figure 5.11

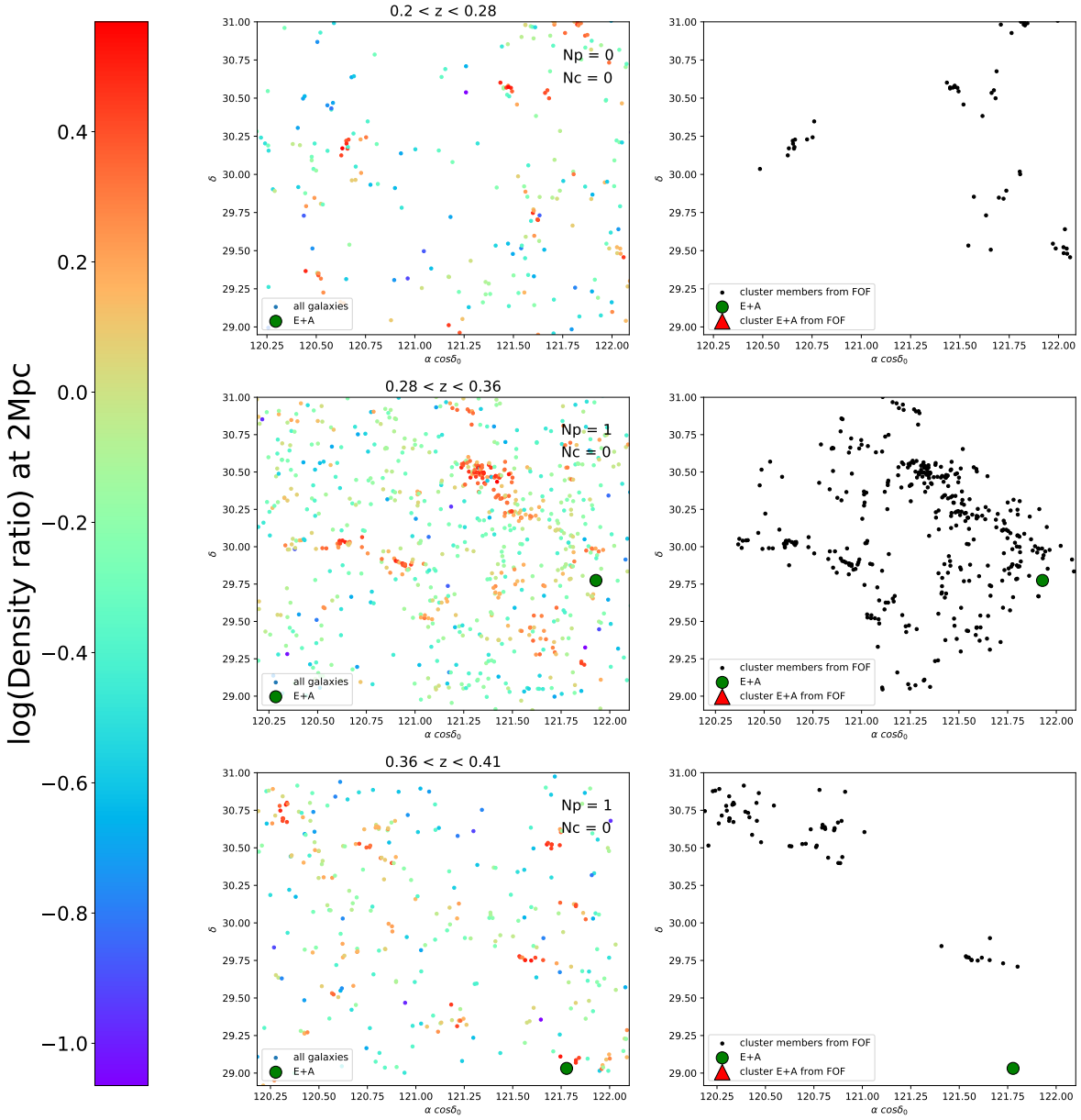

Figure 5.13: Left: Distribution of GSMD ratios around galaxies in volume-limited SHELS F2 sample on α cosδ_0 and dec δ plane in different redshift bins, where δ_0 = 30 degrees. The density ratio values are colour coded on a logarithmic scale with the redder colours representing the highest densities. All symbols follow same color scheme as in Figure 5.11

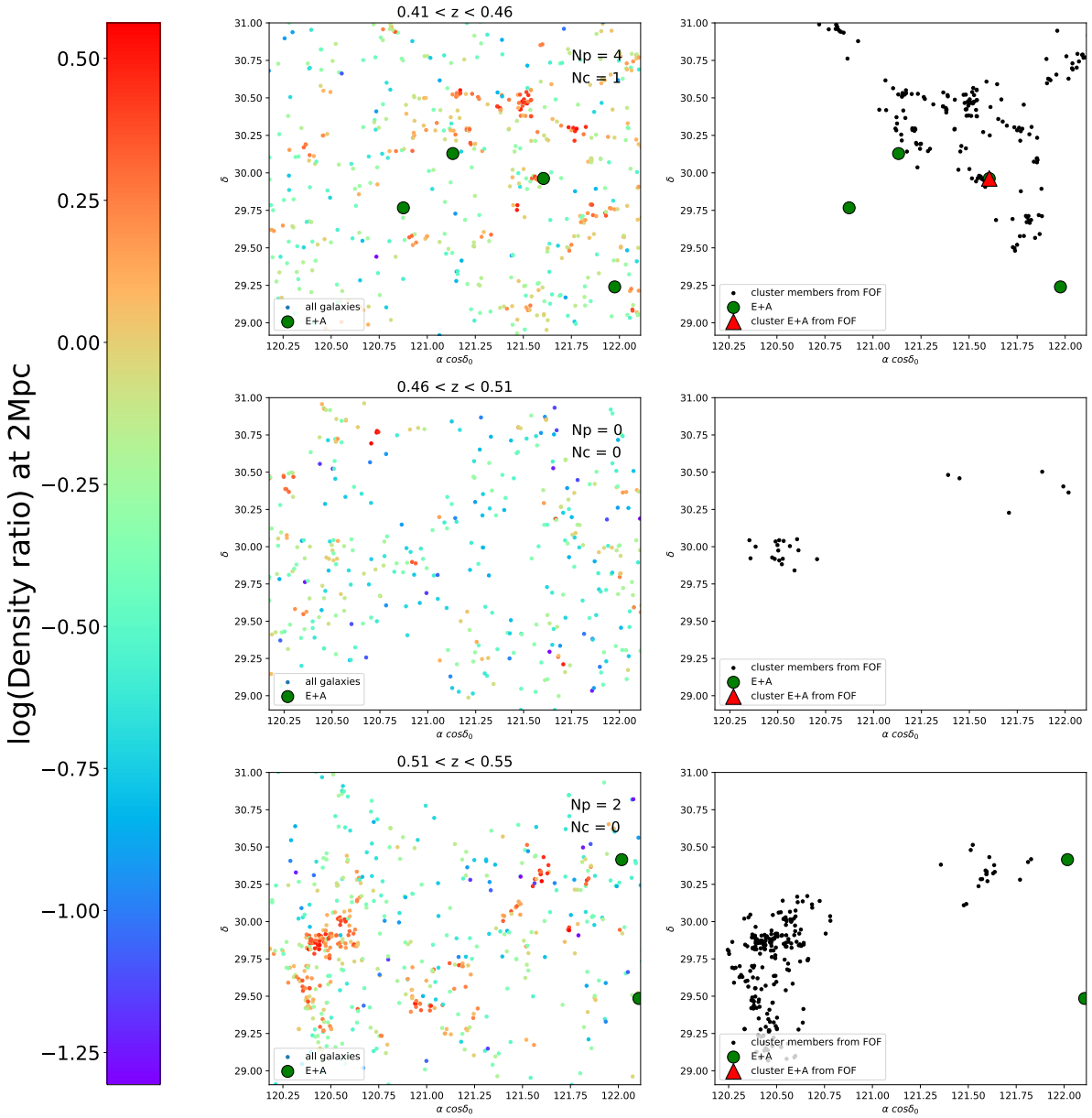

Figure 5.14: Continuation of Figure 5.13

Table 5.2: Number of star-forming and quiescent galaxies within similar stellar mass range as star-forming E+A ($D_n4000 < 1.5$) and quiescent E+A ($D_n4000 > 1.5$) galaxies, respectively, from mass-limited SHELS F2 sample as a function of scale length.

Scale (Mpc)	No. of star-forming galaxies	No. of quiescent galaxies
1	1881	4753
2	1797	4569
3	1708	4355
4	1617	3597

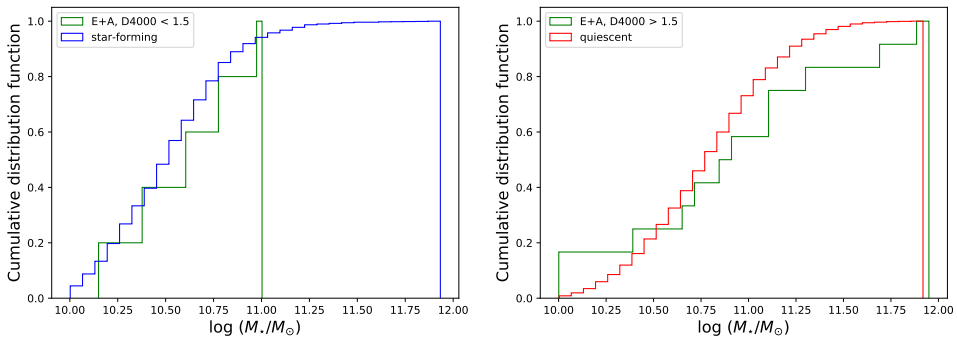

Figure 5.15: Left: Stellar mass range of star-forming galaxies (blue histogram) from SHELS F2 field that are mass-matched to the star-forming ($D_n4000 < 1.5$) E+A galaxies (green histogram). Right: Stellar mass range of quiescent galaxies (red histogram) that are mass-matched to the quiescent ($D_n4000 > 1.5$) E+A galaxies (green histogram). See text for details on mass matching.

5.4.3 Comparison of GSMD measurements for mass-matched samples

We want to compare GSMD values around E+A galaxies with GSMD values around star-forming and quiescent galaxies. To account for the trend in local GSMD with stellar mass, i.e., for the fact that more massive galaxies tend to reside in denser environments, we choose samples of star-forming and quiescent galaxies mass-matched to E+A galaxies in SHELS F2 mass-limited sample.

To construct mass-matched samples, we choose star-forming galaxies having stellar masses within lower and upper mass limits of star-forming E+A ($D_n4000 < 1.5$) and quiescent ($D_n4000 > 1.5$)

E+A galaxies respectively (Figure 5.15). We do not consider edge galaxies in our mass-matched samples. As number of edge galaxies increase with smoothing scale, number of galaxies in our mass-matched samples decrease with increase in length of smoothing scale (Table 5.2).

We construct kernel density estimation (kde) distribution functions using `Kernel density estimator`[5] both for star-forming ($D_n4000 < 1.5$) and quiescent ($D_n4000 > 1.5$) E+A galaxies separately. Both kde functions are based on Gaussian kernels with the optimal bandwidths estimated from `Grid search`[6]. We sample 1000 times from both kde functions with each sample size equal to number of star-forming and quiescent E+A galaxies. For every galaxy in each sample we then select the closest match in mass from the parent mass-limited star-forming or quiescent galaxy sample (Table 5.2). At the end, the procedure provides 1000 samples of both star-forming and quiescent galaxies that closely match the distribution of our star-forming and quiescent E+A galaxies respectively.

We perform K-S test for GSMD/GSMD ratio distribution of each mass-matched star-forming and quiescent sample with GSMD/GSMD ratio distribution of all mass-limited E+A galaxies. Based on K-S test results from GSMD/GSMD ratio distributions, we cannot reject the null hypothesis that E+A galaxies reside in similar density environments as similarly massive star-forming galaxies for > 90% of 1000 samples at all scales. From K-S tests of GSMD/GSMD ratio distribution of mass-matched quiescent galaxies with GSMD/GSMD ratio distribution of E+A galaxies, we find that we cannot reject the null hypothesis that E+A galaxies reside in similar density environments as

[5]`Kernel density estimator` is a package in `Scikit-learn` software written in `Python` programming language and is used for data analysis. More information about `Kernel density estimator` is available at https://scikit-learn.org/stable/modules/generated/sklearn.neighbors.KernelDensity.html.

[6]`Grid search` is also a package in `Scikit-learn` software used for data analysis. Information about `Grid Search` package is available at https://scikit-learn.org/stable/modules/generated/sklearn.model_selection.GridSearchCV.html.

similarly massive quiescent galaxies for $\sim 92\%$ of 1000 samples for 1 and 4 Mpc and for $\sim 67\%$ of 1000 samples at 2 and 3 Mpc. Overall, distributions from K-S test results do not show any distinction between the type of environments in which E+A galaxies reside with respect to similarly massive star-forming and quiescent galaxies. However, results may suggest that at intermediate scales of 2 and 3 kpc, E+A galaxies reside in different density environments than similarly massive quiescent galaxies. We further explore this below by comparing the distribution of GSMD and GSMD ratios for mass-matched E+A, star-forming, and quiescent galaxies separated into three mass bins.

The stellar mass values of mass-limited E+A galaxies lie within $10 < \log(M_\star/M_\odot) < 12$. We choose three mass bins as $10 < \log(M_\star/M_\odot) < 10.5$, $10.5 < \log(M_\star/M_\odot) < 11$ and $11 < \log(M_\star/M_\odot) < 12$. There are 5, 6 and 6 E+A galaxies in the first, second and third mass bin for smaller scale lengths which reduce to (5,6,5) and (3,6,5) for 3 and 4 Mpc respectively because of the edge effects (Section 5.2). We divide galaxies from 1000 mass-matched star-forming and quiescent samples into the same three mass bins. For each mass-matched sample in each mass bin, we compute median GSMD/GSMD ratios. For the distribution of 1000 median GSMD/GSMD ratio values in each mass bin, we calculate median, 16^{th} percentile and 84^{th} percentile values for star-forming and quiescent galaxies in each mass bin.

Figures 5.16 and 5.17 show $[16, 50, 84]\%$ range for the distribution of 1000 median GSMD values computed for mass-matched star-forming and quiescent galaxies in three mass bins and for four smoothing scales (1 to 4 Mpc). Figures 5.16 and 5.17 also show $[16, 50, 84]\%$ range of GSMD distributions for mass-limited E+A galaxies. In addition, GSMD values for individual E+A galaxies binned by stellar mass are also shown (orange points).

Median GSMD values for E+A galaxies are lower than median GSMD values for mass-matched

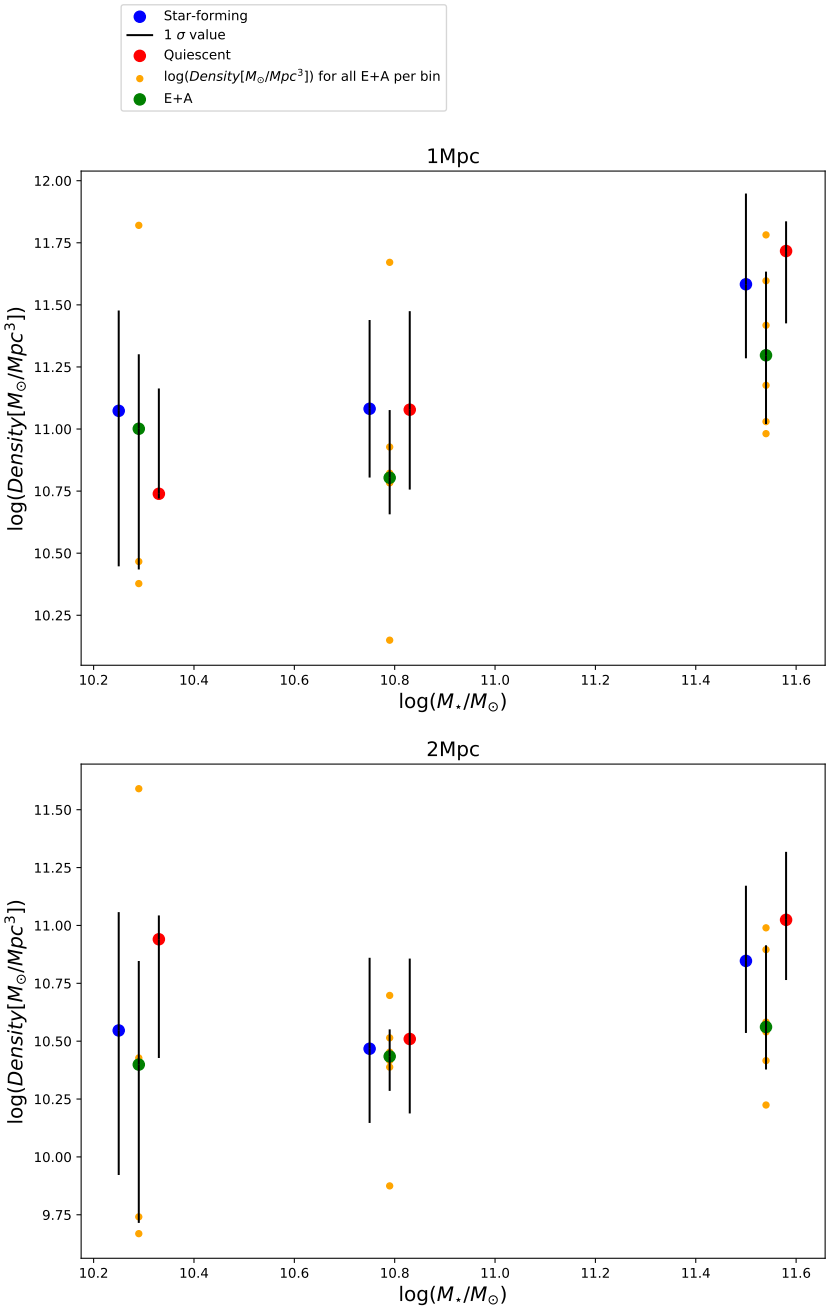

Figure 5.16: Top: Distribution of median GSMD values around E+A (green), mass-matched star-forming (blue) and mass-matched quiescent galaxies (red) in three mass bins: $10 < \log(M_\star/M_\odot) < 10.5$, $10.5 < \log(M_\star/M_\odot) < 11$ and $11 < \log(M_\star/M_\odot) < 12$ on log scale for smoothing scale length of 1 Mpc. Upper and lower black lines at each median GSMD value show $\pm$ 1 σ range. GSMD values of E+A galaxies are shown as orange points in each mass bin. Bottom: Continuation of top panel for scale length of 2 Mpc. See text for details on the estimation of median values for each mass bin.

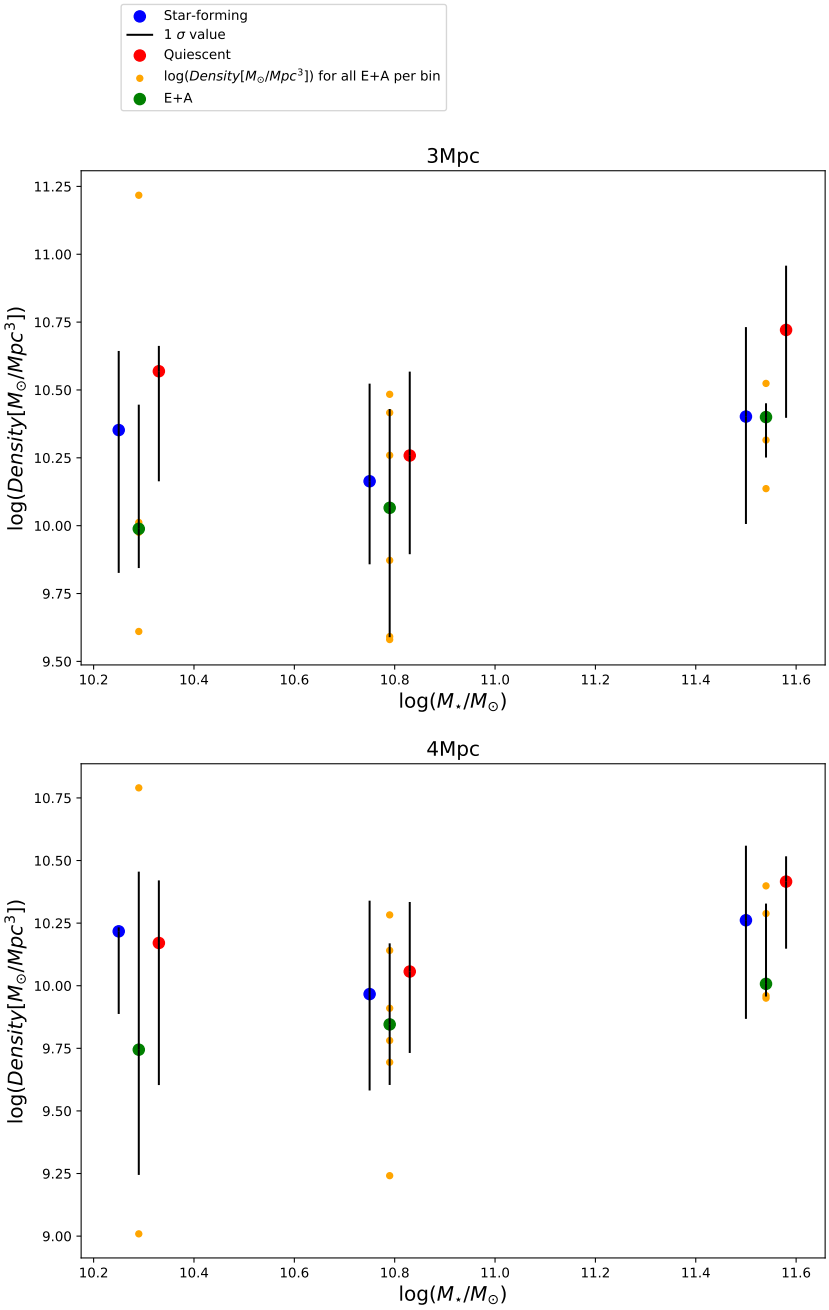

Figure 5.17: Continuation of Figure 5.16 for smoothing scales of 3 and 4 Mpc.

quiescent galaxies in each mass bin at all scales except the first mass bin at 1Mpc. At 1Mpc, median GSMD values for E+A galaxies is slightly higher than the median value for mass-matched quiescent galaxies in the first mass bin. Also, median GSMD values for E+A galaxies are lower than median GSMD values of mass-matched star-forming galaxies at all scales except the second mass bin at 2 Mpc, where median GSMD for E+A galaxies is more similar to median GSMD of mass-matched star-forming galaxies.

We also compare the median GSMD ratios (Section 5.1) of E+A galaxies with median GSMD ratios of two mass-matched galaxy populations in three mass bins (Figures 5.18, 5.19). Median GSMD ratios for E+A galaxies are lower than median GSMD ratios of mass-matched quiescent galaxies at all scales in all mass bins, consistent with the results from Figures 5.16 and 5.17. The comparison of median GSMD ratios between E+A galaxies and mass-matched star-forming galaxies reveals similarities with the results for absolute GSMD values for 1 and 4 Mpc. However, in contrast to absolute GSMD comparison, median GSMD ratio values for E+A galaxies are more similar to the values for mass-matched star-forming galaxies in second and third mass bins at 2 and 4 Mpc.

All mass-matching comparison results have large uncertainties associated with the small number of E+A galaxies in the sample (and, by design, small number of galaxies in each of 1000 mass-matched samples of star-forming and quiescent galaxies) and thus are not statistically significant. From the comparison results of median GSMD/GSMD ratios of E+A galaxies with the median GSMD/GSMD ratios for mass-matched star-forming and quiescent galaxies, we conclude that there are some indications that E+A galaxies reside in lower density environments than similarly massive quiescent galaxies and in similar or lower density environments with respect to star-forming galaxies of the same mass. Larger samples of E+A galaxies are needed to confirm the result that our analysis

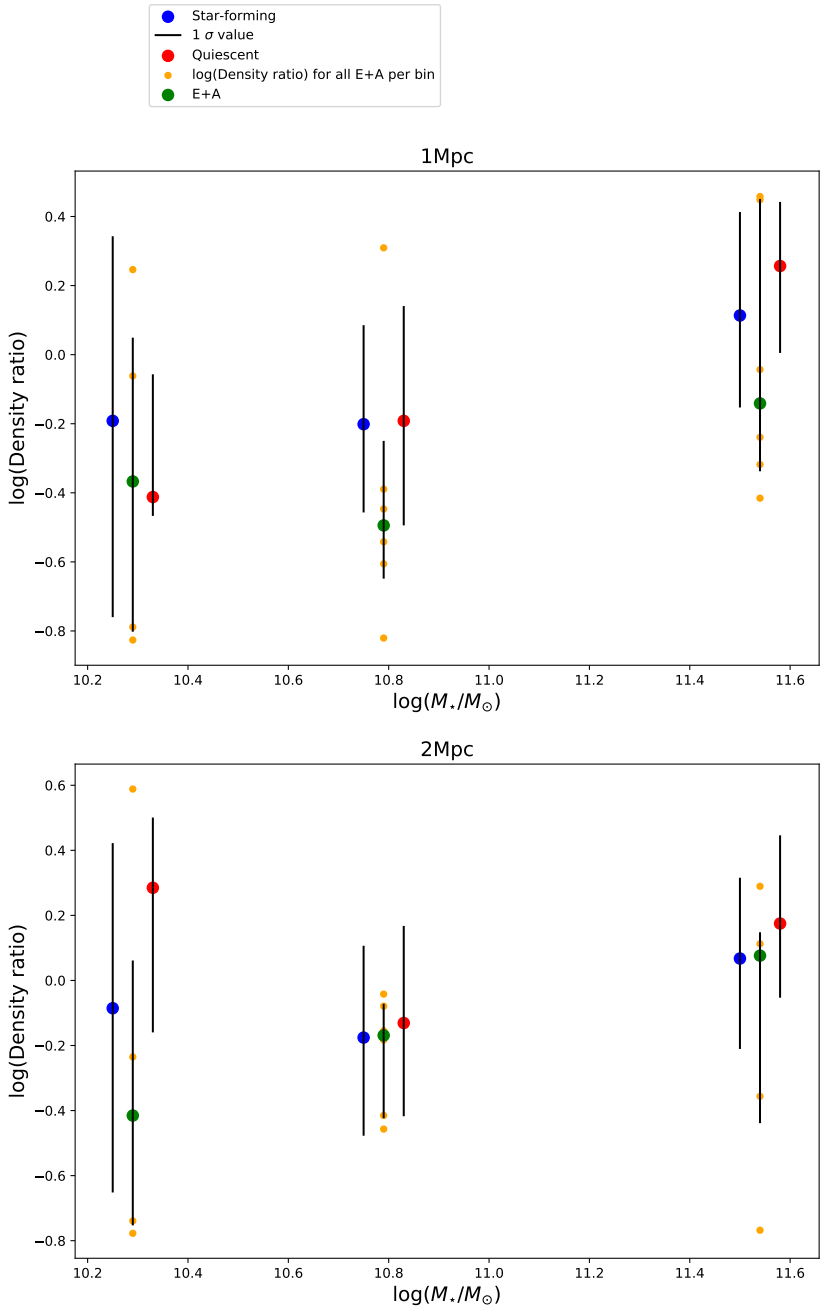

Figure 5.18: Top: Distribution of median GSMD ratio values around E+A (green), mass-matched star-forming (blue) and mass-matched quiescent galaxies (red) in three mass bins: $10 < \log(M_\star/M_\odot) < 10.5$, $10.5 < \log(M_\star/M_\odot) < 11$ and $11 < \log(M_\star/M_\odot) < 12$ on log scale for smoothing scale length of 1 Mpc. Upper and lower black lines at each median GSMD ratio value show $\pm$ 1 σ range. GSMD ratio values of E+A galaxies are shown as orange points in each mass bin. Bottom: Continuation of top panel for scale length of 2 Mpc. See text for details on the estimation of median values for each mass bin.

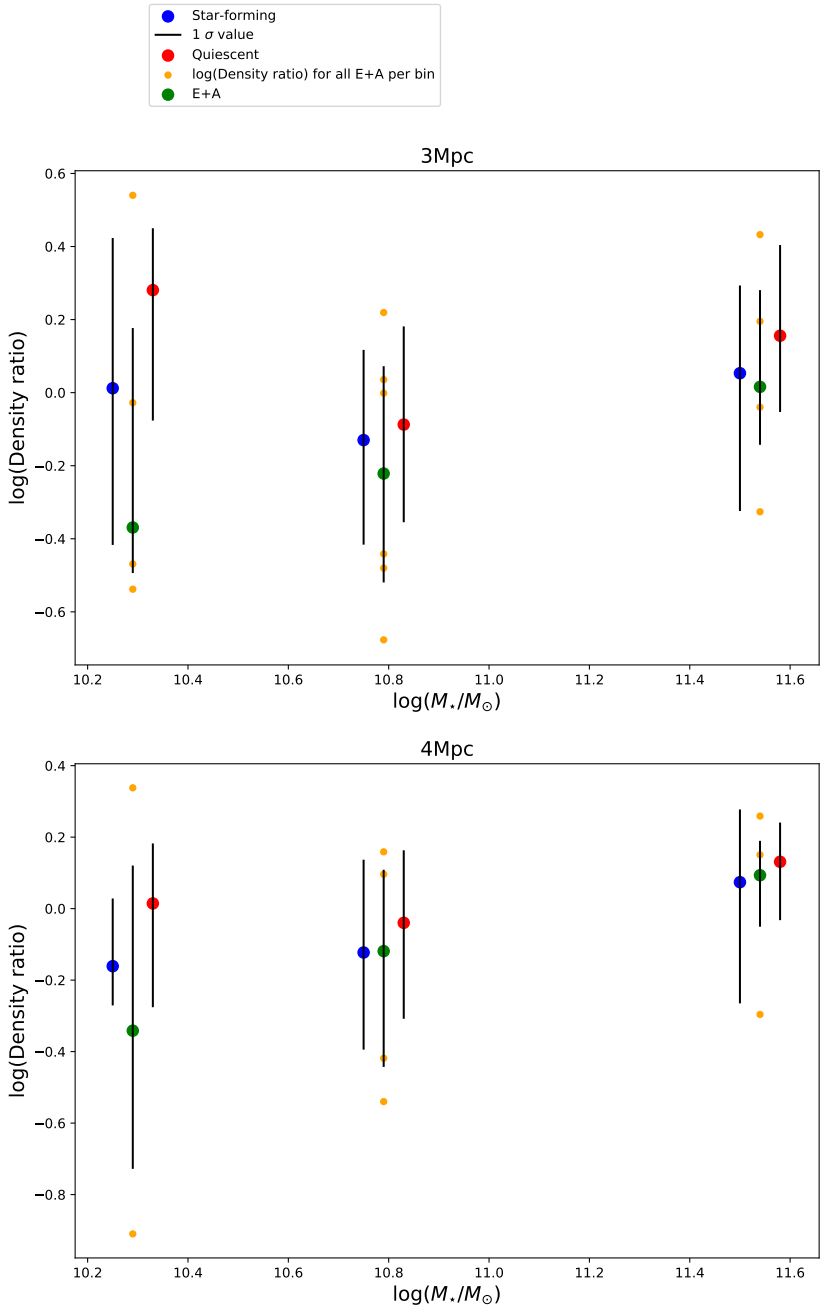

Figure 5.19: Continuation of Figure 5.18 for smoothing scales of 3 and 4 Mpc.

suggests.

Chapter 6

Discussion

6.1 Environments of E+A galaxies

In this chapter, we compare the fraction of E+A galaxies in different environments from GSMD measurements (Chapter 5) with literature in Section 6.1.1. We also investigate origin mechanisms of E+A galaxies in underdense, average and overdense regions (Table 5.1) based on internal properties and Hyper Suprime-Cam (HSC) $i-$band images (Aihara et al. 2018) in Section 6.1.2.

6.1.1 Fraction of E+A galaxies in different environments

We study the environments of E+A galaxies at $0.2 < z < 0.55$. Values in Table 6.1 confirm similar contributions of E+A galaxies to both FoF cluster and field galaxy population in the SHELS F2 sample. This conclusion holds for both mass-limited and volume-limited samples.

We divide GSMD ratios in SHELS F2 field in three bins, based on [0-33, 34-67, 68-100] percentiles of their distribution. We name these bins as underdense, average dense and overdense

Table 6.1: Percentage contribution of E+A galaxies to total galaxy population in FoF cluster and field environments for mass-limited and volume-limited samples.

Sample	cluster	field
Mass-limited	$0.08\%^{+0.11\%}_{-0.05\%}$	$0.30\%^{+0.21\%}_{-0.17\%}$
Volume-limited	$0.11\%^{+0.25\%}_{-0.08\%}$	$0.39\%^{+0.19\%}_{-0.14\%}$

respectively. Then we calculate the contribution of E+A galaxies to the general galaxy population in each bin as shown in Table 6.2.

Based on GSMD ratios, the contribution of E+A galaxies to galaxy population in overdense regions is consistent with the contribution of FoF cluster E+A galaxies to overall FoF cluster population in mass-limited/volume-limited samples within error bars at all scales (compare column 3 of Table 6.2 with column 1 of Table 6.1). In the following discussion we will use the contribution of E+A galaxies to the FoF clusters and their fraction in overdense regions interchangeably. This consistency that we find holds also if we compare E+A fraction in underdense and average regions with E+A contribution to non-cluster galaxy population from FoF results in mass-limited/volume-limited samples within error bars at all scales (compare columns 1 and 2 of Table 6.2 with column 2 of Table 6.1). Overall low fraction of E+A galaxies to the general galaxy population in all environments illustrates that post-starburst galaxies represent a short lived phase in galaxy evolution (Couch & Sharples 1987; Barger et al. 1996; Lotz et al. 2020; Baron et al. 2021).

Studies of the environments of E+A galaxies indicate that these galaxies are found both in clusters and field at all redshifts but their abundance changes with redshift and environment (Poggianti & Barbaro 1997; Yang et al. 2008; Poggianti et al. 2009; Paccagnella et al. 2017). E+A galaxies are

Table 6.2: Percentage contribution of E+A galaxies to total galaxy population in different GSMD ratio bins: 0 to 33, 34 to 67 and 68 to 100 percentiles of GSMD ratio distribution of all galaxies with lower and upper errors. GSMD ratio values in first, second and third bin correspond to underdense, average and overdense regions respectively.

Scale (Mpc)	$0-33$	$34-67$	$68-100$
1	$0.26\%^{+0.15\%}_{-0.1\%}$	$0.30\%^{+0.15\%}_{-0.1\%}$	$0.17\%^{+0.14\%}_{-0.08\%}$
2	$0.27\%^{+0.16\%}_{-0.1\%}$	$0.26\%^{+0.15\%}_{-0.1\%}$	$0.23\%^{+0.15\%}_{-0.09\%}$
3	$0.33\%^{+0.17\%}_{-0.12\%}$	$0.23\%^{+0.15\%}_{-0.1\%}$	$0.19\%^{+0.15\%}_{-0.09\%}$
4	$0.25\%^{+0.17\%}_{-0.1\%}$	$0.1\%^{+0.12\%}_{-0.06\%}$	$0.35\%^{+0.18\%}_{-0.13\%}$

more likely to be found in clusters at $z > 0.2$ and in the field at $z \sim 0.1$. Although there are studies which indicate the presence of E+A galaxies in clusters at $z \sim 0.1$ (Mahajan 2013; Poggianti et al. 2016; Paccagnella et al. 2017), there are very few studies that find significant fraction of E+A galaxies in the field and groups at $z \geq 0.2$ (Balogh et al. 1999; Poggianti et al. 2009).

The results from different studies corresponding to the environments of E+A galaxies at $0.2 < z < 0.8$ are contradictory. Most of the previous studies at $0.2 < z < 0.8$ found large abundance of E+A galaxies in clusters and either low or no presence of E+A galaxies in low density environments like galaxy groups and field (Dressler et al. 1999; Tran et al. 2003; Dressler et al. 2013). However there are other studies which found similar fraction of E+A galaxies in both clusters ($1.5\% \pm 0.8\%$) and field ($1.2\% \pm 0.8\%$) at $z \sim 0.2-0.5$ (Balogh et al. 1999) and significant fraction of E+A galaxies in groups with low [OII] emission ($12\% \pm 5\%$) in addition to clusters ($11\% \pm 2\%$) at $z \sim 0.4-0.8$ (Poggianti et al. 2009).

The fraction of our mass-limited sample E+A galaxies in overdense regions and FoF clusters (third column of Table 6.2 and first column of Table 6.1) is lower as compared to fractions of E+A

galaxies in clusters from previous studies at $0.2 < z < 0.8$ at all scales. One of the reasons for larger fraction of cluster E+A galaxies in previous studies as compared to our study is that all these studies are based on surveys which primarily focus on clusters unlike the survey (SHELS) which we use for our study. The absolute fractions between our study and previous studies may also differ because of the mass range that is probed and the selection criteria employed. Here we investigate qualitatively if the selection itself may account for the discrepancy between our and some previously reported results.

None of the studies at $0.2 < z < 0.8$ use the combination of conditions on minimum equivalent widths of Hδ and [OII] spectral lines and visual inspection similar to our analysis and hence are prone to contamination in their sample from galaxies with AGN. The selection criteria based on conditions on minimum equivalent width values strongly depends on the methodology used to find equivalent width. Dressler et al. (1999) uses Gaussian fitting method to find equivalent widths of Hδ and [OII] spectral lines and use EW([OII]) > 0 Å as the selection criteria for E+A sample. Gaussian fitting method gives highly uncertain results in the estimation of weak spectral lines because it fits a Gaussian preferentially to the noise rather than the spectral line (Goto et al. 2003a). Using Gaussian fit-based measurements of EW([OII]) values to select a sample of E+A galaxies can result in contamination from galaxies with AGN and affect the results.

Unlike previously described studies, Poggianti et al. (2009) found significant fraction ($12\% \pm 5\%$) of E+A galaxies in groups (galaxies in these groups have low [OII] emission) in addition to clusters at $z = 0.4 - 0.8$. Poggianti et al. (2009) uses EW conditions such as EW([OII]) > -5 Å and EW(Hδ) > 3 Å to select E+A galaxies and 10 nearest neighbours to compute local projected densities around galaxies (Section 1.3.1.1). In spite of the differences, we can still compare our results with Poggianti

et al. (2009) because the authors use spectroscopic samples to map densities[1], similar to our analysis. Fractions of our mass-limited sample E+A galaxies in overdense, underdense and average density regions (Table 6.2) are lower than cluster E+A and group with low [OII] emission E+A fractions reported by Poggianti et al. (2009) within error bars. Slightly different selection criteria and redshift range might be the reasons for discrepancy between our results and results from Poggianti et al. (2009).

The fraction of our mass-limited sample E+A galaxies in underdense regions (first column of Table 6.2) is consistent with E+A fraction in the field from Balogh et al. (1999) within error bars at all scales. However, fraction of our mass-limited sample E+A galaxies in overdense regions (third column of Table 6.2) is lower than cluster E+A fraction from Balogh et al. (1999). Balogh et al. (1999) uses flux summing method to find EW and E+A selection criteria based on minimum conditions on EW values (EW([OII]) > -5 Å and EW(Hδ) > 5 Å), similar to our analysis. Additionally, Balogh et al. (1999) traces redshift range $0.2 < z < 0.5$ which overlaps with redshift range of our interest. Hence, similar selection criteria, redshift range and methodology to compute EW might be the reasons for consistency between our results and results from Balogh et al. (1999).

At $z \sim 0.1$, many studies investigate the projected local densities around E+A galaxies using SDSS data (Quintero et al. 2004; Balogh et al. 2005; Goto 2005a; Hogg et al. 2006; Nolan et al. 2007; Yan et al. 2009). Unlike surveys at $0.2 < z < 0.8$, SDSS is not primarily focused on clusters similar to survey used in our study (SHELS). All SDSS-based studies at $z \sim 0.1$ find that E+A galaxies reside in low density environments i.e. the field. Our results are consistent with the studies at $z \sim 0.1$. Balogh et al. (2005), Goto (2005a) and Nolan et al. (2007) use similar minimum EW conditions in

[1]Poggianti et al. (2009) defines cluster as structures consisting of galaxies with velocity dispersion $\sigma_{cluster} > 400$ km/s and groups with $160 < \sigma_{group} < 400$ km/s with at least 10 spectroscopic members.

selection criteria as our study to select E+A galaxies. Quintero et al. (2004), Hogg et al. (2006) and Yan et al. (2009) select E+A galaxies on the basis of measurements of excess flux coming from A type stars than K type stars (derived from SED fitting) combined with the conditions on EW(Hα) and EW(Hβ) emission lines. Similar selection criteria and, more importantly, the similarity between SDSS and SHELS surveys, may be the reason for the consistency between our results at $z \sim 0.3$ and the ones at $z \sim 0.1$.

All SDSS-based studies at $z \sim 0.1$ compute local densities around E+A galaxies using neighbouring galaxies within $\pm$ 1000 km s^{-1} along the line of sight to exclude foreground and background objects (Section1.3.1.1). Balogh et al. (2005), Nolan et al. (2007) and Yan et al. (2009) compute local densities around E+A galaxies within projected distances to 5^{th}, 10^{th} and 3^{th} nearest neighbour (Section1.3.1.1) respectively. Goto (2005a), Quintero et al. (2004) and Hogg et al. (2006) use aperture method (Section 1.3.1.2) to compute densities with a combination of scale lengths varying from kpc to Mpc. Our study is similar to Goto (2005a) in terms of both selection criteria and methodology to estimate densities.

The similarity of our results with the studies at $z \sim 0.1$ and discrepancies between our results and studies at $z > 0.4$ paint a picture that the redshift range we are probing might be the transition period for the origin mechanisms of E+A galaxies. In this transition period ($0.2 < z < 0.4$), major mechanism for the formation of E+A galaxies becomes more related to direct galaxy-galaxy interactions/mergers in lower density environments than to cluster-related environmental processes.

6.1.2 Origin of E+A galaxies

The origin mechanism of E+A galaxies is strongly related to the density of the environments in which these galaxies reside (Section 1.4). Since most of the studies at $0.2 < z < 0.8$ find E+A galaxies in clusters, proposed physical process for the formation of E+A galaxies at this redshift interval is related to dense galaxy environments in clusters. The process that is most commonly mentioned in the literature is ram-pressure stripping (Couch & Sharples 1987; Dressler & Gunn 1992; Tran et al. 2003; Poggianti et al. 2009; Paccagnella et al. 2017; Lotz et al. 2020). As galaxies fall into cluster, their gas is stripped by hot intracluster medium quenching their star formation(Gunn & Gott 1972; Larson et al. 1980; Moore et al. 1996; Sohn et al. 2019).

Five out of 26 i.e. $19.2\%^{+13.8\%}_{-9.1\%}$ of galaxies in our E+A sample are cluster FoF members within $0.2 < z < 0.55$ (Section 5.3). Two out of these five E+A FoF cluster members lie in our E+A mass-limited sample and one lies in volume-limited sample. Hence, the fraction of cluster members in our E+A mass-limited sample within $0.2 < z < 0.55$ is 2/17 i.e. $11.8\%^{+16\%}_{-8\%}$ and in volume-limited sample within $0.2 < z < 0.55$ is 1/8 i.e. $12.5\%^{+29\%}_{-11\%}$. Environmental processes should be affecting the formation and evolution of these cluster E+A galaxies.

Ram-pressure stripping disturbs the morphology of star-forming galaxies as they quench but the resultant E+A galaxies formed still retain disc like morphology (Poggianti et al. 2009). Five E+A galaxies in our FoF clusters within $0.2 < z < 0.55$ have high Sérsic index values ($n > 3$) within errors, consistent with the luminosity profile of elliptical galaxies. We investigate i-band Hyper Suprime-Cam (Aihara et al. 2018) images of these galaxies. All cluster E+A galaxies appear to be bulge-dominated objects with no signs of disks that ram-pressure stripping should not destroy.

We expect to see signatures of ram-pressure stripping such as disturbed morphologies with tidal features in $i-$band images if stripping of molecular hydrogen gas from the galaxy induces star formation in the galaxy (Poggianti et al. 2009). If ram-pressure stripping does not induce star-formation then signatures of stripping can be seen in CO(2–1) emission ($\sim$ 200 GHz, Smercina et al. 2021). The observations of CO(2–1) emission are not currently available for SHELS F2 galaxies. Thus we conclude, based only on HSC $i-$band imaging that ram-pressure stripping may not play role in the formation of cluster E+A galaxies in our sample.

For massive enough galaxies ($\log(M_{star}/M_{\odot}) > 11$), environment does not necessarily play important role in quenching (Peng et al. 2010). Stellar mass values of cluster E+A galaxies in our sample are less than $\log(M_{star}/M_{\odot}) = 11$, hence mass quenching may not be important for their formation.

In low density environments, the major mechanism that drives the formation of E+A galaxies is gas rich major merger/galaxy interactions (Bekki et al. 2001; Blake et al. 2004; Quintero et al. 2004; Goto 2005b; Hogg et al. 2006; Mahajan 2013; Yesuf et al. 2014; Lotz et al. 2020). A major gas rich merger results in the formation of compact objects (Zolotov et al. 2015) with bulge dominated morphologies and high Sérsic index values (Canalizo et al. 2000; Yang et al. 2004; Goto et al. 2003b; Cales et al. 2011). The percentage values of compact galaxies in underdense and average density regions (columns 1 and 2 of Table 5.1) vary between 50%-60% and 40%-70% respectively at all scales. These compact galaxies have high Sérsic index values ($n > 3$) and hence may have been formed by gas rich mergers.

Studies of the morphologies of post-starburst galaxies in low density environments indicate that these galaxies have disturbed morphologies and tidal features providing evidence for their merging

origin (Zabludoff et al. 1996; Blake et al. 2004; Goto 2005b; Yamauchi & Goto 2005; Goto et al. 2008; Pracy et al. 2009). We investigate $i-$band HSC images of compact galaxies in underdense and average dense regions to find that majority of them show bulge-dominated morphologies without obvious tidal features. We also investigate $i-$band HSC images of non-compact E+A galaxies in underdense and average dense regions. Majority of these non-compact galaxies in both underdense and average dense regions show tidal features and also have high Sersic index values ($n > 3$).

Majority (60%) of E+A galaxies in underdense and average dense regions show tidal features or high Sérsic index values. Thus, we conclude that major mechanism responsible for the formation of E+A galaxies in underdense and average dense regions is merger/galaxy interactions. Ram-pressure stripping may drive the formation of E+A galaxies in overdense regions. However, the signatures of ram-pressure stripping such as disturbed morphologies with tidal features are not visible in HSC $i-$band images. As all cluster E+A galaxies have $\log(M_\star/M_\odot) < 11$, hence mass quenching may not be important for their formation.

Chapter 7

Conclusions and Future goals

To explore galaxy evolutionary track that includes a post-starburst phase, we study the internal properties and environments of E+A galaxies within $0.2 < z < 0.55$. Our sample consists of 17 E+A galaxies within $0.2 < z < 0.55$ from the parent spectroscopic sample in SHELS F2 field that is 85% complete down to 20.975 in SDSS $r-$band. Our selection criteria of E+A galaxies is based on the minimum EW condition (EW(Hδ) - EW(H$\delta)_{err}$ > 5 Å) for wide Hδ absorption line combined with visual inspection to confirm the absence of [OII] and Hα emission lines.

We investigate the internal properties of E+A galaxies in our sample and compare these with internal properties of star-forming and quiescent galaxies. Galaxy internal properties include structural properties such as Sérsic index and galaxy sizes as well as the trends in spectroscopic measurements (D_n4000 index, EW(Hδ)) with stellar mass. Using our volume-limited sample, we measure the number density evolution of E+A and quiescent galaxies within $0.01 < z < 0.6$ and also calculate the number density growth of quiescent galaxies from post-starburst galaxies from $z = 0.55$ to $z = 0.25$.

Using stellar mass function from Muzzin et al. (2013b), we calculate local GSMD field around

mass-limited SHELS F2 galaxies within $0.2 < z < 0.55$ for four scale lengths (1 to 4 Mpc) following the procedure from Damjanov et al. (2015). We select samples of star-forming and quiescent galaxies mass-matched with E+A galaxies and compare local GSMD and GSMD ratio values in three different mass bins:$10 < \log(M_\star/M_\odot) < 10.5$, $10.5 < \log(M_\star/M_\odot) < 11$ and $11 < \log(M_\star/M_\odot) < 12$. To select E+A cluster galaxies from our sample, we use the results from FoF algorithm (Sohn et al. 2018) which provides additional information about their environments.

Based on the local GSMD field of E+A galaxies in our sample and their internal properties, we investigate physical processes that drive their formation and evolution. Following are the main conclusions:

- Approximately $\sim 90\%$ E+A galaxies in our sample have high Sérsic index ($n > 3$) values, $\sim 67\%$ have $1.2 < D_n4000 < 1.6$ and $\sim 85\%$ have $0.5 < R_c\,[\mathrm{kpc}] < 15$, consistent with other samples of E+A galaxies from literature(Goto 2005a; Vergani et al. 2010; Almaini et al. 2017; Matharu et al. 2020). All these properties and intermediate size-mass relation of E+A galaxies with respect to two galaxy populations in our sample confirm that E+A galaxies are transitional phase between star-forming and quiescent galaxies.

- The number density of quiescent galaxies increases significantly (within the range of 48% - 81% using different redshift bins) from $z = 0.6$ to $z = 0.01$ in our volume-limited sample. The number density of E+A galaxies in our sample is consistent with measurements from Rowlands et al. (2018) at $z = 0.25$ but is lower at $z = 0.55$. The discrepancy at higher redshift may be due the selection effects and difference in mass range probed. Additionally, this discrepancy can arise due to the fact that higher redshift bin is at the edge of our volume-limited sample

and thus may be prone to the effects of incompleteness. Also, with the visibility time of 250 Myr, E+A galaxies in our volume-limited sample contribute only $9\%^{+9\%}_{-7\%}$ to the growth of quiescent galaxies from $z = 0.55$ to $z = 0.25$. The contribution of E+A galaxies to number density growth of quiescent galaxies in our analysis is lower than the studies at $0.5 < z < 2$ such as Wild et al. (2016) and Belli et al. (2019). This evolutionary trend is consistent with the idea that the contribution of E+A galaxies decrease towards the growth of quiescent galaxies from $z \sim 1$ to $z \sim 0$ (Wild et al. 2009; Dressler et al. 2013; Rowlands et al. 2018).

- E+A galaxies contribute only $0.08\%^{+0.11\%}_{-0.05\%}$ to FoF cluster galaxy population and $0.3\%^{+0.21\%}_{-0.17\%}$ to non-cluster galaxy population in our mass-limited SHELS F2 sample. These fractions are consistent with the contribution of E+A galaxies to FoF cluster ($0.11\%^{+0.25\%}_{-0.08\%}$) and non-cluster galaxy population ($0.39\%^{+0.19\%}_{-0.14\%}$) in our volume-limited sample within error bars at $0.2 < z < 0.55$. Low fraction of E+A galaxies as compared to overall galaxy population confirms the fact that post-starburst galaxies represent a short lived phase in galaxy evolution (Couch & Sharples 1987; Barger et al. 1996; Lotz et al. 2020; Baron et al. 2021).

- Based on GSMD measurements, the contribution of E+A galaxies to galaxy population in underdense regions in our mass-limited sample is consistent with the contribution of E+A galaxies to field population from Balogh et al. (1999) within error bars. However the contribution of E+A galaxies to galaxy population in overdense regions is lower than previous studies at $0.2 < z < 0.8$ (Dressler et al. 1999; Balogh et al. 1999; Poggianti et al. 2009; Dressler et al. 2013).

- The fraction of cluster E+A galaxies in our mass-limited sample within $0.2 < z < 0.55$ is 2/17

i.e. $11.8\%^{+16\%}_{-8\%}$. In our volume-limited sample, the fraction of cluster E+A galaxies is 1/8 i.e. $12.5\%^{+29\%}_{-11\%}$ within $0.2 < z < 0.55$. Thus, the fractions of cluster E+A galaxies are consistent within mass-limited and volume-limited samples. Furthermore, lower fraction of cluster E+A galaxies in both samples indicates that E+A galaxies do not preferentially reside in clusters.

- Based on GSMD measurements, E+A galaxies have similar fraction in underdense, average dense and overdense regions within large error bars. Hence, E+A galaxies prefer no special environments. Also, the fraction of E+A galaxies in overdense regions is comparable to the fraction of total number of galaxies in overdense regions, hence E+A galaxies follow general galaxy population.

- Based on mass-matching results, E+A galaxies reside in lower density environments than similarly massive quiescent galaxies and in similar or lower density environments with respect star-forming galaxies of the same mass. However, these results have large uncertainties associated with the small number of E+A galaxies in our sample. Larger samples of E+A galaxies are needed to confirm these results.

- Majority (60%) of E+A galaxies in underdense and average dense regions show tidal features and/or high Sérsic index values. Thus, we conclude that major mechanism responsible for the formation of E+A galaxies in underdense and average dense regions is merger/galaxy interactions. Ram-pressure stripping may drive the formation of E+A galaxies in overdense regions. However, the signatures of ram-pressure stripping such as disturbed morphologies with tidal features are not visible in HSC $i-$band images. As all cluster E+A galaxies have $\log(M_\star/M_\odot) < 11$, hence mass quenching may not be important for their formation.

This study is the first step in our contribution to the understanding of the nature and origin of E+A galaxies at intermediate redshift ($0.2 < z < 0.55$). It can be followed by a number of investigations, including:

- Future Integral field unit (IFU) observations and deep imaging of E+A galaxies with tidal features in our sample can give insight into their merger origin.

- All previous studies at $0.2 < z < 0.8$ select E+A galaxies from surveys which are primarily focused on clusters and find large fraction of E+A galaxies in clusters. We use SHELS for our study which is not focused on clusters and find smaller fraction of E+A galaxies in clusters than in the field environment in our sample. Poggianti et al. (2009) shows that E+A galaxies vary in fraction from cluster to cluster and hence we might be missing some clusters which are exceptionally rich in E+A galaxies. Our next step is to select E+A galaxies from a survey which has large number of clusters such as HeCS-omnibus spectroscopic sample of 227 clusters at $z < 0.3$ (Sohn et al. 2020) to explore why some clusters may have larger number of E+A galaxies.

- Using more relaxed selection criteria which allows the presence of AGN emission lines in their spectra, we intend to include AGN host post-starburst galaxies in our sample and study their internal properties and environments. Using BPT diagram, we can investigate the fraction of post-starburst galaxies which are Seyferts[1] or LINERs[2] and what fraction of LINER and Seyfert post-starburst galaxies live in high or low density environments. We can further investigate if

[1]Seyfert galaxies are highly luminous galaxies having AGN at their centers. They have strong emission lines in their spectra and act as highly energetic ionizing sources.

[2]LINERs are another class of AGN and their spectra have emission lines from weakly ionized atoms.

stellar feedback or AGN feedback is the primary mechanism for quenching of star-formation in E+A galaxies with merger origin by estimating the time delay between starburst and onset of AGN activity (Yesuf et al. 2014).

Bibliography

Abraham R. G., et al., 1996, ApJ , 471, 694

Ahumada R., et al., 2020, ApJS , 249, 3

Aihara H., et al., 2018, PASJ , 70, S4

Almaini O., et al., 2017, MNRAS , 472, 1401

Arnouts S., Cristiani S., Moscardini L., Matarrese S., Lucchin F., Fontana A., Giallongo E., 1999, MNRAS , 310, 540

Arnouts S., et al., 2007, A&A , 476, 137

Asano R. S., Takeuchi T. T., Hirashita H., Inoue A. K., 2013, Earth, Planets, and Space, 65, 213

Balogh M. L., Morris S. L., Yee H. K. C., Carlberg R. G., Ellingson E., 1999, ApJ , 527, 54

Balogh M. L., Christlein D., Zabludoff A. I., Zaritsky D., 2001, ApJ , 557, 117

Balogh M. L., Miller C., Nichol R., Zabludoff A., Goto T., 2005, MNRAS , 360, 587

Barger A. J., Aragon-Salamanca A., Ellis R. S., Couch W. J., Smail I., Sharples R. M., 1996, MNRAS , 279, 1

Baron D., Netzer H., Lutz D., Prochaska J. X., Davies R. I., 2021, arXiv e-prints, p. arXiv:2105.08071

Barro G., et al., 2013, ApJ , 765, 104

Bekki K., Shioya Y., Couch W. J., 2001, ApJ , 547, L17

Bell E. F., et al., 2004, ApJ , 608, 752

Belli S., Newman A. B., Ellis R. S., 2019, ApJ , 874, 17

Berlind A. A., et al., 2006, ApJS , 167, 1

Bertin E., Arnouts S., 1996, A&AS , 117, 393

Bezanson R., van Dokkum P. G., Tal T., Marchesini D., Kriek M., Franx M., Coppi P., 2009, ApJ , 697, 1290

Blake C., et al., 2004, MNRAS , 355, 713

Blanton M. R., et al., 2003, ApJ , 592, 819

Blanton M. R., Eisenstein D., Hogg D. W., Schlegel D. J., Brinkmann J., 2005, ApJ , 629, 143

Boselli A., Gavazzi G., 2006, PASP , 118, 517

Bower R. G., Benson A. J., Malbon R., Helly J. C., Frenk C. S., Baugh C. M., Cole S., Lacey C. G., 2006, MNRAS , 370, 645

Brown M. J. I., Dey A., Jannuzi B. T., Brand K., Benson A. J., Brodwin M., Croton D. J., Eisenhardt P. R., 2007, ApJ , 654, 858

Bruzual G., Charlot S., 2003, MNRAS , 344, 1000

Butkevich A. G., Berdyugin A. V., Teerikorpi P., 2005, MNRAS , 362, 321

Caldwell N., Rose J. A., Franx M., Leonardi A. J., 1996, AJ , 111, 78

Cales S. L., et al., 2011, ApJ , 741, 106

Calzetti D., Armus L., Bohlin R. C., Kinney A. L., Koornneef J., Storchi-Bergmann T., 2000, ApJ , 533, 682

Canalizo G., Stockton A., Brotherton M. S., van Breugel W., 2000, AJ , 119, 59

Carollo C. M., et al., 2013, ApJ , 773, 112

Cassata P., et al., 2007, ApJS , 172, 270

Cen R., 2012, ApJ , 755, 28

Chabrier G., 2003, PASP , 115, 763

Chang T.-C., van Gorkom J. H., Zabludoff A. I., Zaritsky D., Mihos J. C., 2001, AJ , 121, 1965

Cid Fernandes R., et al., 2004, ApJ , 605, 105

Codis S., Pichon C., Pogosyan D., 2015, MNRAS , 452, 3369

Cooper M. C., Newman J. A., Madgwick D. S., Gerke B. F., Yan R., Davis M., 2005, ApJ , 634, 833

Couch W. J., Sharples R. M., 1987, MNRAS , 229, 423

Croton D. J., et al., 2005, MNRAS , 356, 1155

Croton D. J., et al., 2006, MNRAS , 365, 11

Daddi E., et al., 2005, ApJ , 626, 680

Damjanov I., et al., 2011, ApJ , 739, L44

Damjanov I., Hwang H. S., Geller M. J., Chilingarian I., 2014, ApJ , 793, 39

Damjanov I., Zahid H. J., Geller M. J., Hwang H. S., 2015, ApJ , 815, 104

Damjanov I., Zahid H. J., Geller M. J., Utsumi Y., Sohn J., Souchereau H., 2019, ApJ , 872, 91

Di Matteo T., Springel V., Hernquist L., 2005, Nature , 433, 604

Dressler A., Gunn J. E., 1983, ApJ , 270, 7

Dressler A., Gunn J. E., 1992, ApJS , 78, 1

Dressler A., Smail I., Poggianti B. M., Butcher H., Couch W. J., Ellis R. S., Oemler Augustus J., 1999, ApJS , 122, 51

Dressler A., Oemler Augustus J., Poggianti B. M., Gladders M. D., Abramson L., Vulcani B., 2013, ApJ , 770, 62

Fabricant D., et al., 2005, PASP , 117, 1411

Fabricant D. G., Kurtz M. J., Geller M. J., Caldwell N., Woods D., Dell'Antonio I., 2008, PASP , 120, 1222

Fasano G., Franceschini A., 1987, MNRAS , 225, 155

Field G. B., Henry R. C., 1964, ApJ , 140, 1002

Gallazzi A., Charlot S., Brinchmann J., White S. D. M., Tremonti C. A., 2005, MNRAS , 362, 41

Gallazzi A., et al., 2009, ApJ , 690, 1883

Gallazzi A., Bell E. F., Zibetti S., Brinchmann J., Kelson D. D., 2014, ApJ , 788, 72

Gehrels N., 1986, ApJ , 303, 336

Geller M. J., Hwang H. S., Fabricant D. G., Kurtz M. J., Dell'Antonio I. P., Zahid H. J., 2014, ApJS , 213, 35

Geller M. J., Hwang H. S., Dell'Antonio I. P., Zahid H. J., Kurtz M. J., Fabricant D. G., 2016, ApJS , 224, 11

Genzel R., et al., 2014, ApJ , 785, 75

Goto T., 2005a, MNRAS , 357, 937

Goto T., 2005b, MNRAS , 357, 937

Goto T., 2007, MNRAS , 381, 187

Goto T., et al., 2003a, PASJ , 55, 771

Goto T., et al., 2003b, PASJ , 55, 771

Goto T., Kawai A., Shimono A., Sugai H., Yagi M., Hattori T., 2008, MNRAS , 386, 1355

Grogin N. A., Geller M. J., 1998, ApJ , 505, 506

Gunn J. E., Gott J. Richard I., 1972, ApJ , 176, 1

Hashimoto Y., Oemler Augustus J., Lin H., Tucker D. L., 1998, ApJ , 499, 589

Hayward C. C., Torrey P., Springel V., Hernquist L., Vogelsberger M., 2014, MNRAS , 442, 1992

Hilz M., Naab T., Ostriker J. P., Thomas J., Burkert A., Jesseit R., 2012, MNRAS , 425, 3119

Hogg D. W., 1999, Distance measures in cosmology (arXiv:astro-ph/9905116)

Hogg D. W., et al., 2003, ApJ , 585, L5

Hogg D. W., Masjedi M., Berlind A. A., Blanton M. R., Quintero A. D., Brinkmann J., 2006, ApJ , 650, 763

Hopkins P. F., Hernquist L., Cox T. J., Di Matteo T., Robertson B., Springel V., 2006, ApJS , 163, 1

Hopkins P. F., Bundy K., Murray N., Quataert E., Lauer T. R., Ma C.-P., 2009, MNRAS , 398, 898

Hubble E., 1929, Proceedings of the National Academy of Science, 15, 168

Huchra J. P., Geller M. J., 1982, ApJ , 257, 423

Hwang H. S., et al., 2016, ApJ , 818, 173

Ilbert O., et al., 2006, A&A , 457, 841

Ilbert O., et al., 2013, A&A , 556, A55

Jaffé Y. L., Smith R., Candlish G. N., Poggianti B. M., Sheen Y.-K., Verheijen M. A. W., 2015, MNRAS , 448, 1715

Johansson P. H., Naab T., Ostriker J. P., 2009, ApJ , 697, L38

Kauffmann G., et al., 2003a, MNRAS , 341, 33

Kauffmann G., et al., 2003b, MNRAS , 341, 33

Kauffmann G., et al., 2003c, MNRAS , 341, 54

Kauffmann G., White S. D. M., Heckman T. M., Ménard B., Brinchmann J., Charlot S., Tremonti C., Brinkmann J., 2004, MNRAS , 353, 713

Kennicutt R. C. J., 1983, AJ , 88, 483

Kovač K., et al., 2010, ApJ , 708, 505

Kurtz M. J., Mink D. J., 1998, PASP , 110, 934

Larson R. B., Tinsley B. M., Caldwell C. N., 1980, ApJ , 237, 692

Li C., Kauffmann G., Jing Y. P., White S. D. M., Börner G., Cheng F. Z., 2006, MNRAS , 368, 21

Lotz M., Dolag K., Remus R.-S., Burkert A., 2020, Rise and fall of post-starburst galaxies in Magneticum Pathfinder (arXiv:2011.06602)

Mahajan S., 2013, MNRAS , 431, L117

Martig M., Bournaud F., Teyssier R., Dekel A., 2009, ApJ , 707, 250

Matharu J., et al., 2020, MNRAS , 493, 6011

Miller N. A., Owen F. N., 2001, in Lowenthal J. D., Hughes D. H., eds, Deep Millimeter Surveys: Implications for Galaxy Formation and Evolution. pp 127–130, doi:10.1142/9789812811738_0020

Monet D. G., et al., 2003, AJ , 125, 984

Moore B., Katz N., Lake G., Dressler A., Oemler A., 1996, Nature , 379, 613

Moutard T., et al., 2016, A&A , 590, A103

Moutard T., Malavasi N., Sawicki M., Arnouts S., Tripathi S., 2020, MNRAS , 495, 4237

Muldrew S. I., et al., 2012, MNRAS , 419, 2670

Muzzin A., et al., 2013a, ApJS , 206, 8

Muzzin A., et al., 2013b, ApJ , 777, 18

Naab T., Johansson P. H., Ostriker J. P., 2009, ApJ , 699, L178

Nolan L. A., Raychaudhury S., Kabán A., 2007, MNRAS , 375, 381

Norton S. A., Gebhardt K., Zabludoff A. I., Zaritsky D., 2001, ApJ , 557, 150

Oke J. B., Sandage A., 1968, ApJ , 154, 21

Oser L., Ostriker J. P., Naab T., Johansson P. H., Burkert A., 2010, ApJ , 725, 2312

Oser L., Naab T., Ostriker J. P., Johansson P. H., 2012, ApJ , 744, 63

Ostriker J. P., 1980, Comments on Astrophysics, 8, 177

Paccagnella A., et al., 2017, ApJ , 838, 148

Paccagnella A., Vulcani B., Poggianti B. M., Moretti A., Fritz J., Gullieuszik M., Fasano G., 2019, MNRAS , 482, 881

Pattarakijwanich P., Strauss M. A., Ho S., Ross N. P., 2016, ApJ , 833, 19

Peng Y.-j., et al., 2010, ApJ , 721, 193

Petrosian V., 1976, ApJ , 210, L53

Pichon C., Pogosyan D., Kimm T., Slyz A., Devriendt J., Dubois Y., 2011, MNRAS , 418, 2493

Planck Collaboration et al., 2014, A&A , 571, A16

Poggianti B. M., Barbaro G., 1997, A&A , 325, 1025

Poggianti B. M., Wu H., 2000, ApJ , 529, 157

Poggianti B. M., Smail I., Dressler A., Couch W. J., Barger A. J., Butcher H., Ellis R. S., Oemler Augustus J., 1999, ApJ , 518, 576

Poggianti B. M., et al., 2009, ApJ , 693, 112

Poggianti B. M., et al., 2016, AJ , 151, 78

Pracy M. B., Kuntschner H., Couch W. J., Blake C., Bekki K., Briggs F., 2009, MNRAS , 396, 1349

Quintero A. D., et al., 2004, ApJ , 602, 190

Quintero A. D., Berlind A. A., Blanton M. R., Hogg D. W., 2005, What galaxies know about their nearest cluster (arXiv:astro-ph/0512004)

Rodriguez-Gomez V., et al., 2015, MNRAS , 449, 49

Rowlands K., et al., 2018, MNRAS , 473, 1168

Schawinski K., Thomas D., Sarzi M., Maraston C., Kaviraj S., Joo S.-J., Yi S. K., Silk J., 2007, MNRAS , 382, 1415

Schechter P., 1976, ApJ , 203, 297

Sell P. H., et al., 2014, MNRAS , 441, 3417

Sersic J. L., 1968, Atlas de Galaxias Australes. Observatorio Astronomico de Cordoba, Cordoba, Argentina

Shen S., Mo H. J., White S. D. M., Blanton M. R., Kauffmann G., Voges W., Brinkmann J., Csabai I., 2003, MNRAS , 343, 978

Smail I., Morrison G., Gray M. E., Owen F. N., Ivison R. J., Kneib J. P., Ellis R. S., 1999, ApJ , 525, 609

Smercina A., et al., 2021, arXiv e-prints, p. arXiv:2108.03231

Smethurst R. J., Lintott C. J., Bamford S. P., Hart R. E., Kruk S. J., Masters K. L., Nichol R. C., Simmons B. D., 2017, MNRAS , 469, 3670

Snyder G. F., Cox T. J., Hayward C. C., Hernquist L., Jonsson P., 2011, ApJ , 741, 77

Sohn J., Geller M. J., Hwang H. S., Zahid H. J., Lee M. G., 2016, ApJS , 225, 23

Sohn J., Geller M. J., Rines K. J., Hwang H. S., Utsumi Y., Diaferio A., 2018, ApJ , 856, 172

Sohn J., Geller M. J., Zahid H. J., Fabricant D. G., 2019, ApJ , 872, 192

Sohn J., Geller M. J., Diaferio A., Rines K. J., 2020, ApJ , 891, 129

Sohn J., Geller M. J., Hwang H. S., Diaferio A., Rines K. J., Utsumi Y., 2021, The HectoMAP Cluster Survey: Spectroscopically Identified Clusters and their Brightest Cluster Galaxies (BCGs) (arXiv:2106.11429)

Stoughton C., et al., 2002, AJ , 123, 485

Suess K. A., Kriek M., Price S. H., Barro G., 2021, ApJ , 915, 87

Taylor E. N., Franx M., Glazebrook K., Brinchmann J., van der Wel A., van Dokkum P. G., 2010, ApJ , 720, 723

Teerikorpi P., 1997, ARA&A , 35, 101

Tempel E., Tago E., Liivamägi L. J., 2012, A&A , 540, A106

Toomre A., 1964, ApJ , 139, 1217

Tran K. V. H., 2007, in Metcalfe N., Shanks T., eds, Astronomical Society of the Pacific Conference Series Vol. 379, Cosmic Frontiers. p. 348

Tran K.-V. H., Franx M., Illingworth G., Kelson D. D., van Dokkum P., 2003, ApJ , 599, 865

Tran K.-V. H., Franx M., Illingworth G. D., Kelson D. D., van Dokkum P., 2004, in Diaferio A., ed., IAU Colloq. 195: Outskirts of Galaxy Clusters: Intense Life in the Suburbs. pp 483–487, doi:10.1017/S1743921304001048

Trujillo I., et al., 2006, ApJ , 650, 18

Trujillo I., Cenarro A. J., de Lorenzo-Cáceres A., Vazdekis A., de la Rosa I. G., Cava A., 2009, ApJ , 692, L118

Vergani D., et al., 2010, A&A , 509, A42

White S. D. M., Rees M. J., 1978, MNRAS , 183, 341

Wild V., Kauffmann G., Heckman T., Charlot S., Lemson G., Brinchmann J., Reichard T., Pasquali A., 2007, MNRAS , 381, 543

Wild V., Walcher C. J., Johansson P. H., Tresse L., Charlot S., Pollo A., Le Fèvre O., de Ravel L., 2009, MNRAS , 395, 144

Wild V., Almaini O., Dunlop J., Simpson C., Rowlands K., Bowler R., Maltby D., McLure R., 2016, MNRAS , 463, 832

Wild V., et al., 2020, MNRAS , 494, 529

Williams R. J., Quadri R. F., Franx M., van Dokkum P., Toft S., Kriek M., Labbé I., 2010, ApJ , 713, 738

Wilman D. J., Zibetti S., Budavári T., 2010, MNRAS , 406, 1701

Wittman D., Dell'Antonio I. P., Hughes J. P., Margoniner V. E., Tyson J. A., Cohen J. G., Norman D., 2006, ApJ , 643, 128

Wolf C., et al., 2004, A&A , 421, 913

Wolf C., et al., 2009, MNRAS , 393, 1302

Wu P.-F., Gal R. R., Lemaux B. C., Kocevski D. D., Lubin L. M., Rumbaugh N., Squires G. K., 2014, ApJ , 792, 16

Yamauchi C., Goto T., 2005, MNRAS , 359, 1557

Yan R., Newman J. A., Faber S. M., Konidaris N., Koo D., Davis M., 2006, ApJ , 648, 281

Yan R., et al., 2009, MNRAS , 398, 735

Yang Y., Zabludoff A. I., Zaritsky D., Lauer T. R., Mihos J. C., 2004, ApJ , 607, 258

Yang Y., Zabludoff A. I., Zaritsky D., Mihos J. C., 2008, ApJ , 688, 945

Yesuf H. M., Faber S. M., Trump J. R., Koo D. C., Fang J. J., Liu F. S., Wild V., Hayward C. C., 2014, ApJ , 792, 84

Zabludoff A. I., Zaritsky D., Lin H., Tucker D., Hashimoto Y., Shectman S. A., Oemler A., Kirshner R. P., 1996, ApJ , 466, 104

Zahid H. J., Geller M. J., Kewley L. J., Hwang H. S., Fabricant D. G., Kurtz M. J., 2013, ApJ , 771, L19

Zahid H. J., Baeza Hochmuth N., Geller M. J., Damjanov I., Chilingarian I. V., Sohn J., Salmi F., Hwang H. S., 2016b, ApJ , 831, 146

Zahid H. J., Baeza Hochmuth N., Geller M. J., Damjanov I., Chilingarian I. V., Sohn J., Salmi F., Hwang H. S., 2016a, ApJ , 831, 146

Zahid H. J., Geller M. J., Damjanov I., Sohn J., 2019, ApJ , 878, 158

Zehavi I., et al., 2005, ApJ , 630, 1

Zolotov A., et al., 2015, MNRAS , 450, 2327

Zwaan M. A., Kuntschner H., Pracy M. B., Couch W. J., 2013, MNRAS , 432, 492

de Vaucouleurs G., 1948, Annales d'Astrophysique, 11, 247

van der Wel A., Holden B. P., Zirm A. W., Franx M., Rettura A., Illingworth G. D., Ford H. C., 2008, ApJ , 688, 48

van der Wel A., Bell E. F., van den Bosch F. C., Gallazzi A., Rix H.-W., 2009, ApJ , 698, 1232

van der Wel A., et al., 2014, ApJ , 788, 28